Radio Continuum of Galaxies with H_2O-Megamaser-Disks

Dissertation
zur
Erlangung des Doktorgrades (Dr. rer. nat.)
der
Mathematisch-Naturwissenschaftlichen Fakultät
der
Rheinischen Friedrich-Wilhelms-Universität Bonn

vorgelegt von
Fateme Kamali
aus
Firoozabad (Iran)

Bonn 2019

Angefertigt mit Genehmigung der Mathematisch-Naturwissenschaftlichen Fakultät der Rheinischen Friedrich-Wilhelms-Universität Bonn

1. Gutachter:	Prof. Dr. Karl M. Menten
2. Gutachter:	Prof. Dr. Pavel Kroupa
Tag der Promotion:	12.07.2019
Erscheinungsjahr:	2019

To my parents, for their love and support.

Contents

Abstract

Galaxies with H_2O -megamaser-disks are low luminosity active galaxies where 22 GHz H_2O -maser emission is detected in their accretion disk surrounding the central suppermassive black hole (SMBH). Furthermore, given that the geometry of the maser disk is known, they provide a unique view of the central region of active galaxies, allowing us to investigate the spatial relationship of the accretion disk with jets on the same physical scales. In this work, we attempt to study the alignment between the radio jet and the associated rotation axis of the sub-pc accretion disks which are traced by the 22 GHz H_2O -megamaser emission. This is an essential part of the paradigm describing active galactic nuclei. Our observations were carried out using radio interferometer arrays with three different resolutions, corresponding to physical scales of $\sim$ 145 pc, $\sim$ 34 pc, and $\sim$ 2 pc at a fiducial distance of 85 Mpc (mean of distances in our sample). Our observations provide a larger sample where morphology or geometry of both accretion disk and jets are observed on similar physical scales.

On kiloparsec scales, our observations were carried out using the Karl G. Jansky Very Large Array (VLA) at 33 GHz. We detect radio emission in 87% of the sources in our sample. We find evidence for biconical extended jets on scales >300 pc for four sources. Seventeen other sources show only one component, often accompanied by extended emission. Among the sources with biconical structure where the maser disk orientation is known, we find that the jet-like 33 GHz continuum feature in one source (NGC 4388) appears to be perpendicular to the maser disk's orientation.

On scales of $\sim$ 100 pc, we used the enhanced Multi-Element Radio Linked Interferometer Network (eMERLIN) at 5 GHz to investigate the radio emission. We detected radio emission in 56% of the sources in our sample. Four sources show biconical morphologies, three sources remain unresolved, and three other sources show extended emission. For four of the detected sources, the orientation of the maser disk is known. In all four, the radio continuum is misaligned with the rotation axis of the disk, but by not more than 37° relative to the disk's rotation axis.

On parsec-scales, using the Very Long Baseline Array (VLBA) at 5 GHz, we detect 28% of the sources, where two sources show only one component, and three other sources show multiple components in the radio maps. Among the five detections, four of them exhibit a maser disk with known orientation. For all four of these sources, the radio continuum is misaligned relative to the rotation axis of the maser disk, but with a 99.1% confidence level, the orientations are not random and are confined to a cone within 32° of the maser disk's normal. Among the four sources the misalignment of the radio continuum with respect to the normal vector to the maser disk is smaller when the inner radius of the maser disk is larger.

Furthermore, based on the spectral indices, brightness temperatures and multi-scale morphologies, we conclude that the radio emission in the majority of our sources is dominated by both outflow and star formation. Further observations, such as full polarization studies and kinematic studies of outflows, will help construct a more complete picture of the central region of active galaxies.

Prologue: Our insignificant presence in the Universe

According to the standard model of cosmology, the Universe is about 13.8 billion years old, and we Homo sapiens on the other hand, are only about 300,000 years old. If we scale the 13.8 billion years old Universe to one year, a unit more understandable for us humans, assuming the big bang happened on January 1st, the planet Earth was formed in mid-September (Sagan 1977). The first forms of multicellular life appeared on Earth only in mid-December. The first evidence for the appearance of humans indicates that they came around 10:30 pm in the evening of the New Year's Eve in this one year old Universe. All human history, from domestication of fire, use of stone tools, cave paintings, invention of agriculture to the invention of computers, landing on the moon, searching for extraterrestrial intelligent life, and even the beginning for a possible existential crisis of humans (climate change) occurred only in the last one and a half hours of New Year's Eve (Sagan 1977). And only in the last minute of this one year old Universe (i.e., 40 seconds in the 1.5 hours existence of humans), we have known that the Universe extends beyond our Galaxy[1].

In the history of human beings, the sky, and especially the night sky, has always aroused curiosity. Until about a 100 years ago, the nature of the fuzzy, cloudy like objects in the sky called nebulae (mostly observable with telescopes), was still uncertain. In 1920, a famous debate on the size of the Universe and the location of the nebulae took place between two astronomers; Harlow Shapley and Heber Curtis. Shapley believed that these nebulae are in the host galaxy of our planet, i.e., the Milky Way, while Curtis argued that they are outside the Milky Way. A few years later, Hubble found the distance to one of these unknown nebulae (M31) using a type of variable star called Cepheids, and proved that extragalactic sources exist (Carroll & Ostlie 2006).

Nowadays we know that there are many billions of other galaxies in the Universe. Figure 0.1 shows only a fraction of one degree in the sky[2], and every fuzzy light source seen in this image is a galaxy (the image contains about 5,500 galaxies). This demonstrates how vast and enormous our Universe is, and we are able to comprehend it, thanks to the developments of our brains' neocortex, and countless other evolutionary steps. We humans are self-conscious and each of us has the ability to create new thoughts. Nevertheless, our greatest advances have been accomplished through the cooperation with each other, and thanks to our cumulative knowledge, we have learned a great deal about our surroundings, yet still not enough. Among all the species on Earth, humans have the most amount of information stored in their genes and brain (Sagan 1977). As we managed to store information via writing and recording, we are able to progress faster towards understanding ourselves, our surroundings, and the Universe. On this path, we also have encountered countless new questions and mysteries. This thesis wishes to make a very small contribution to our understanding of the Universe and hopefully has lit another spark to shed more light, adding to those already shining.

[1] Here I attempted to roughly demonstrate how different important events in the history of the Universe are placed in time with respect to each other. The estimated time of the events are not accurate, hence these events could happen a little sooner or later in this re-scaled calendar.

[2] One degree is roughly the width of your little finger when you stretch your arm in front of you, which is about two times size of the full moon in the sky.

When You and I behind the Veil are past,
Oh but the long long while the world shall last,
Which of our Coming and Departure heeds,
As much as Ocean of a pebble-cast.
(Omar Khayyam, 11^{th}-12^{th} century)

Figure 0.1: Hubble eXtreme Deep Field (XDF) image. This image has been made by combining images made with the NASA Hubble Space Telescope over more than 10 years. The combined exposure time is 2 million seconds. Every fuzzy dot seen in this image is a galaxy. © NASA; ESA; G. Illingworth, UCO/Lick Observatory and the University of California, Santa Cruz; R. Bouwens, UCO/Lick Observatory and Leiden University; and the HUDF09 Team.

Structure of this thesis

In Chapter 1, I present an introduction to what motivates this thesis. In Chapter 2, I present our pilot project aimed to measure the radio continuum emission of H_2O -megamaser galaxies at the kpc-scale. Chapter 3 focuses on the contribution of this work to investigating the standard paradigm of active galactic nuclei. I discuss the possible dominant sources of the observed radio emission in our sample in Chapter 4. Finally, I present the summary and give an outlook in Chapter 5.

CHAPTER 1

Introduction

1.1 What are H_2O-megamaser galaxies?

Galaxies have different morphologies; some are elliptical, some are disk-shaped, some lenticular or even irregular. It is generally accepted that in the center of each "normal" galaxy[1] exists a very massive object, called a supermassive black hole (SMBH, Kormendy & Richstone 1995). These SMBHs can have masses between 10^7 to 10^{10} $M_\odot$[2]. In some galaxies the central SMBH is quiescent, e.g., in our Milky Way, but in other galaxies the SMBH is actively accreting matter. This matter accretion can be very violent and aggressive which makes the central region of the galaxy shine very bright, even outshining the rest of the galaxy. The central regions of galaxies with an accreting SMBH are called active galactic nuclei or AGNs. Since the AGN's black holes are surrounded by orbiting gas, if the gas is able to eventually cool, an accretion disk is formed in the equatorial plane (Blandford et al. 2018). Accretion onto the accretion disk is often accompanied by ejection of material to the outside of the disk, via the so called jets. These jets can be empowered and collimated by the central SMBH and the accretion disk, and can expand to intergalactic space at a distance multiple times the size of the galaxy itself. The jets are often invisible in the optical regime, but appear very bright in the radio, and can sometimes be seen in the infrared (IR) and X-rays (see Fig. 1.1). Some active galaxies are hosts to a very interesting physical phenomenon that cannot happen naturally on Earth: *masers*. The microwave amplification by the stimulated emission of radiation (maser) has a similar mechanism as the laser but the radiation is in the microwave regime. Devices yielding maser emission were first built in laboratories (on Earth) in 1953 (Gordon et al. 1954), since this phenomenon cannot occur naturally in environments where thermal equilibrium holds. Under thermal equilibrium, the energy levels of atoms and molecules are populated following a Boltzmann distribution with positive excitation temperature, with $N/g = e^{-h\nu/k_B T_{ex}}$, where N is the column density, g is the statistical weight of the given state, $h\nu$ is the energy above the ground state, k_B is the Boltzmann constant and T_{ex} is the positive excitation temperature. In this case the radiation attenuates while traveling through a medium because it gets absorbed. However, in the interstellar medium the conditions are usually out of thermal equilibrium, and the densities are below the critical density for collisional de-excitation, therefore atoms and molecules can stay in the excited states. An incident photon with energy equal to the energy difference between two levels, can cause decay of one excited atom or molecule and the resulting photon has the same frequency

[1] In this work, the term galaxy does not refer to dwarf galaxies, which have stellar masses at least two orders of magnitudes less than our Milky Way.

[2] $M_\odot$, denotes the solar mass which is $\sim 1.98\times10^{33}$grams.

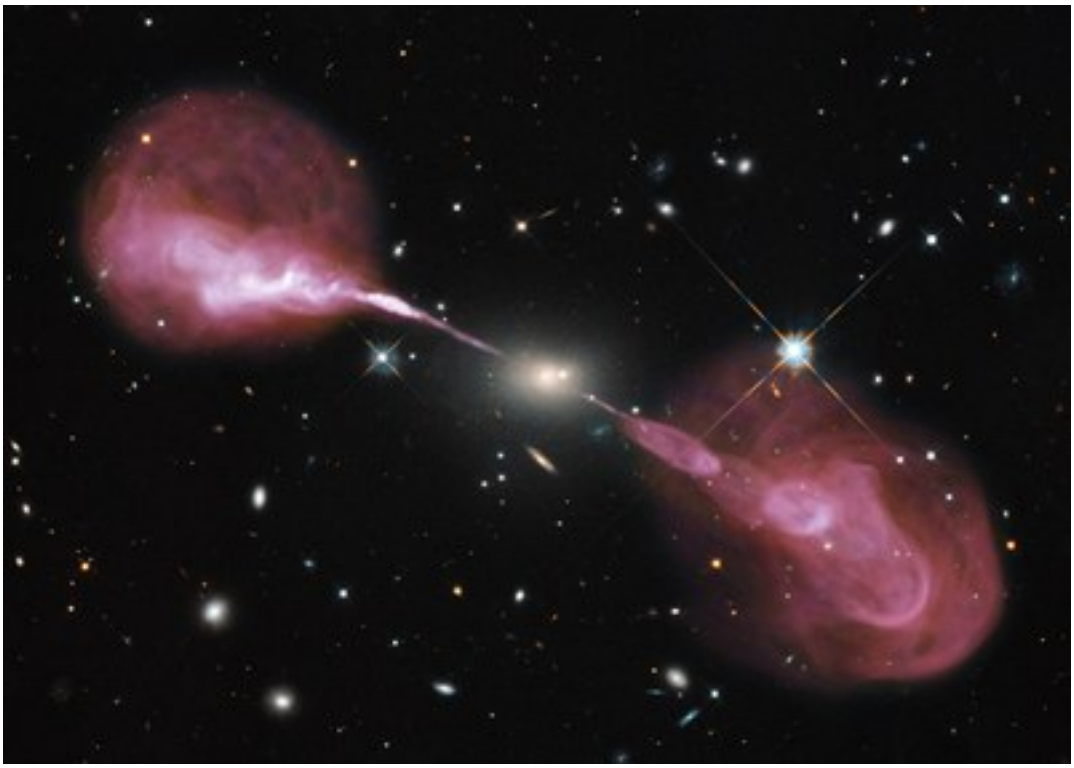

Figure 1.1: Hercules A. This elliptical galaxy at the distance of ~ two billion light years (686 Mpc, NASA Extragalactic Database) is a strong radio galaxy and an AGN. In this image, the galaxy is seen as a fuzzy yellow ellipse, observed by the Hubble Space Telescope's Wide Field Camera 3. The radio jets (invisible at optical wavelengths) are shown in red, observed using the Karl G. Jansky Very Large Array (VLA) radio telescope in New Mexico. The jet size is about 1.5 million light-years wide, extending to several times the size of the galaxy. © NASA, ESA, S. Baum and C. O'Dea (RIT), R. Perley and W. Cotton (NRAO/AUI/NSF), and the Hubble Heritage Team (STScI/AURA).

and direction as the incident photon. This process is called stimulated emission, which results in the amplification of the radiation. Thus, maser phenomena can naturally occur in space, given the proper physical conditions such as low particle densities are met. Astrophysical masers were first discovered in the Milky Way (Weaver et al. 1965) and later on, also in extragalactic sources such as the galaxy M33 (Churchwell et al. 1977). The line emission from extragalactic masers can be about 10^6 times more luminous than typical masers found in the Milky Way. In this case they are called megamasers. Maser emission is observed from rotational or vibrational transitions in molecules such as OH, H_2O, CH_3OH, HCN, and SiO. In 1993, H_2O megamaser emission, emitted from the water vapor $J_{K\_K_+}=6_{16}$-5_{23} rotational transition at the rest frequency of 22.23508 GHz (λ 1.3 cm), was detected with a relatively broadband spectrometer (Nakai et al. 1993). Its spectrum was quite different from others: there were three different groups of lines, one group had a recessional velocity[3] corresponding to that of the galaxy, and the other groups were blueshifted and redshifted by hundreds of km s^{-1} with respect to the first group. This was the first discovery of a so-called H_2O -disk-megamaser galaxy (Nakai et al. 1993). Milliarcsecond resolution Very Long Baseline Interferometry (VLBI) showed that the masers are distributed in a sub-parsec[4] sized Keplerian disk surrounding the central engine

[3] Recessional velocity is the velocity at which an astronomical object is being carried along with its surrounding space due to the expansion of the Universe (see e.g., Carroll & Ostlie 2006).

[4] One parsec is about 3.26 light years or 3.08×10^{16}meters.

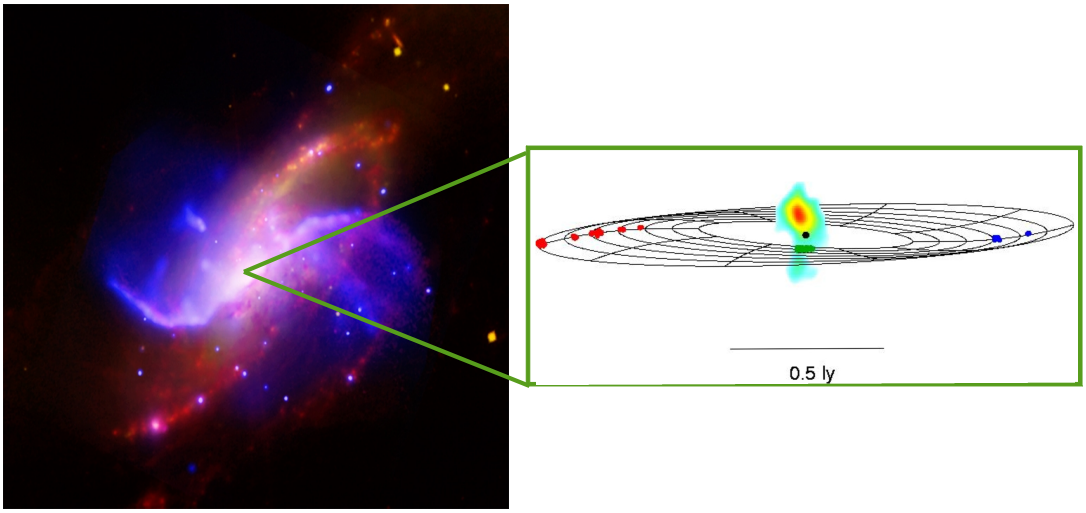

Figure 1.2: NGC 4258, the prototype H_2O -megamaser galaxy. The left image is a combination of X-rays (blue), optical (gold), Infrared (red) and radio (purple) observations. © X-ray: NASA/CXC/Univ. of Maryland/A.S. Wilson et al.; Optical: Palomar Observatory. DSS; IR: NASA/JPL-Caltech; VLA: NRAO/AUI/NSF. The right hand panel shows the H_2O -megamaser-disk (a warped disk) and the sub-pc radio jet perpendicular to it (Herrnstein et al. 1999).

of the galaxy (see Fig. 1.2). Soon after their discovery, H_2O -megamaser galaxies became very important for cosmological studies, since their distances can be measured directly and independently of any cosmological models. In the next section, two important aspects of these fascinating galaxies are described in further detail.

1.2 The importance of H_2O -megamaser galaxies

1.2.1 Measuring a fundamental cosmological parameter: the Hubble constant

Our Universe, which contains billions of galaxies, is expanding. The so called Hubble-Lemaître law which formulates this expansion, implies that the recessional velocity (v) of the galaxies is related to their distance (D), and the proportionality constant is called the Hubble constant (H_0):

$$v = H_0 D \tag{1.1}$$

The inverse of the Hubble constant is a measure of the age of the Universe (Liddle 2015). Therefore, a precise measurement of H_0 is very important for our understanding of the Universe, particularly its age. Over the past 90 years astronomers have determined H_0 using different methods. However, the development of new techniques and instruments have recently led to more precise and accurate measurements which resulted in a potential controversy: H_0 measurements from different methods are currently inconsistent within uncertainties. These current measurements indicate a 3.5 σ discrepancy between the measured values from the local Universe and the more distant early Universe (Riess et al. 2016). If this existing inconsistency turns out to be real and not due to systematic issues, its implications could be of great importance to our understanding of the Universe. It could imply that either our understanding of the physics

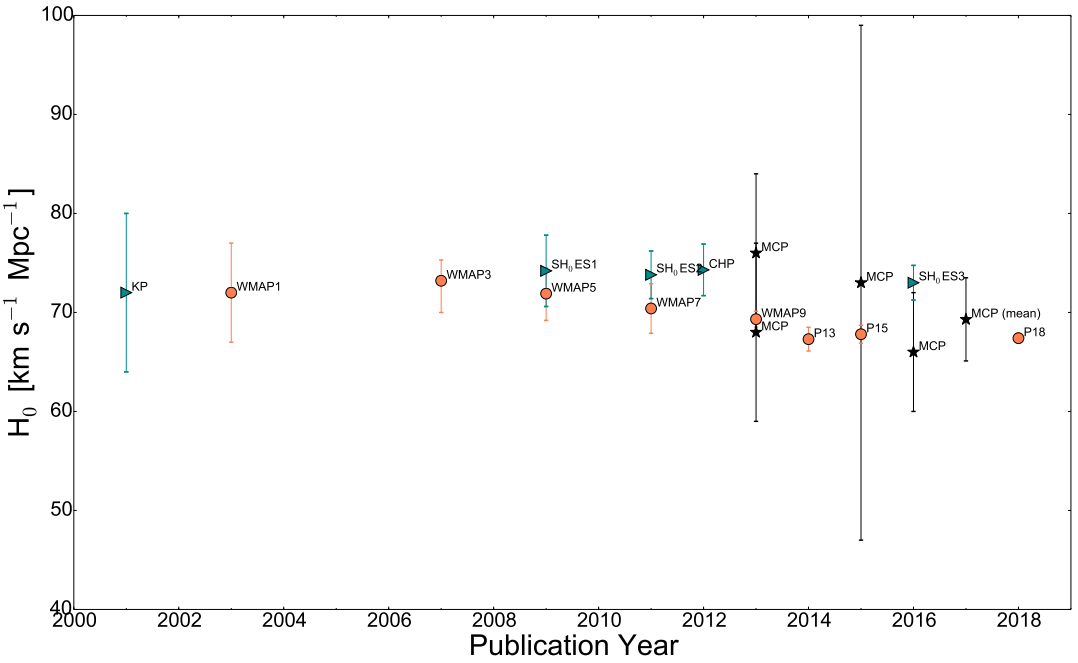

Figure 1.3: H_0 measurements since the year 2000. The measurements from the local Universe are shown with teal triangles, from the early Universe (assuming a flat geometry) with orange circles and from H_2O -megamaser-disks with black stars. References for the data: Freedman et al. (2001); Spergel et al. (2003, 2007); Riess et al. (2009); Dunkley et al. (2009); Komatsu et al. (2011); Riess et al. (2011); Freedman et al. (2012); Bennett et al. (2013); Reid et al. (2013); Kuo et al. (2013); Planck Collaboration et al. (2014); Kuo et al. (2015); Gao et al. (2016); Riess et al. (2016); Planck Collaboration et al. (2016, 2018); Braatz et al. (2018). Plot © FKamali

of the early Universe or our understanding of the local Universe is poor. The latter could be equivalent to having systematic problems in the local distance measurements. Therefore it is important to have as many independent H_0 measurements as possible.

Figure 1.3 shows different measurements of the Hubble constant since the year 2000. In order to measure H_0, one has to measure both the recessional velocity and the distance to the galaxies. Measuring the recessional velocity is usually not a complicated issue, however, measuring the distance could sometimes be a great challenge. This is where galaxies with H_2O -megamaser-disks come into the picture. These galaxies provide an opportunity to measure their distances directly, and more importantly, independent of cosmological models. Finding more galaxies with H_2O -megamaser-disks is crucial to getting a larger number of H_2O -maser based distance measurements in order to have lower statistical uncertainties. The Megamaser Cosmology Project (MCP) was initiated to measure H_0 within 3% accuracy using at least 9 galaxies hosting H_2O -megamaser-disks. The H_2O -megamasers are mostly associated with two types of active galaxies called Seyfert 2 and LINERs (low-ionization nuclear emission-line regions), thus the MCP has surveyed more than 4000 such galaxies to find suitable H_2O -megamaser-disks in order to determine their geometric distances. The survey resulted in a $\lesssim 1\%$ detection rate, only ~ 9 are potentially good candidates that are located well into the Hubble flow where the motion of galaxies due to the expansion of the Universe dominates other motions (see e.g., Kuo et al. 2018). Since the megamaser emission is very bright, using radio interferometry techniques (see Sect. 1.7) the physical size of the Keplerian disks could be measured. The distance to the host galaxies could also be measured directly using the angular diameter distance D, which relates

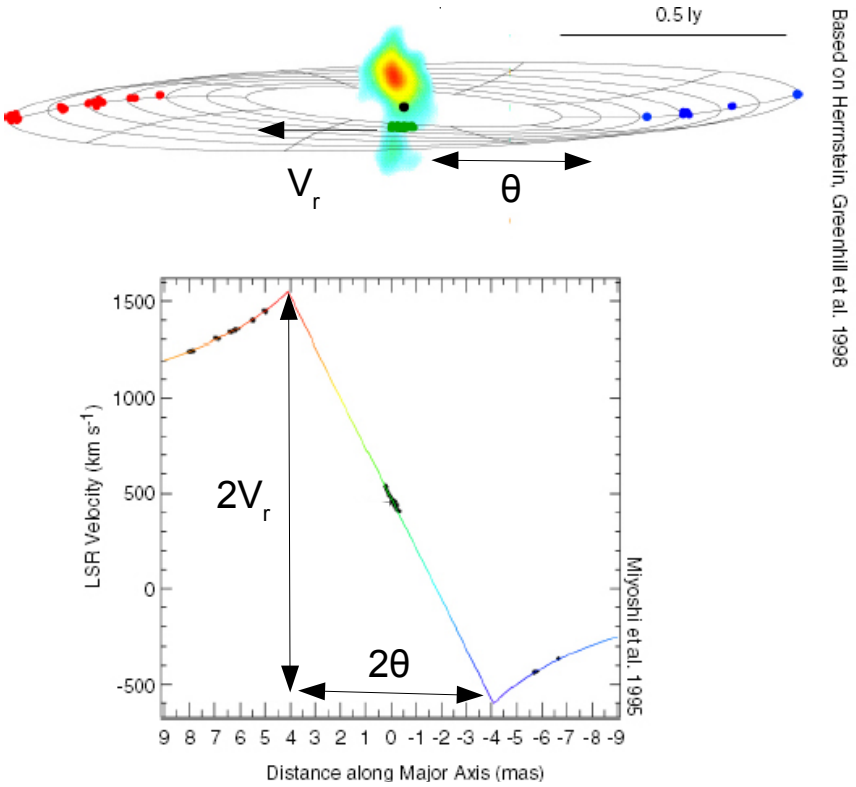

Figure 1.4: The H_2O -megamaser-disk in NGC 4258. The angular diameter distance (D) is measured using the velocity corresponding to radius r (V_r), the acceleration ($a = \frac{V_r^2}{r}$), and the disk's angular size (θ, measured using the rotation curve as shown here). ©JBraatz, reconstructed by FKamali based on Miyoshi et al. (1995); Greenhill et al. (1995); Herrnstein et al. (1998).

the actual size of an object (here the physical size of the maser disk, r) to its apparent angular size, θ:

$$D = \frac{r}{\theta} \tag{1.2}$$

In practice, for the simplest model, the distance is determined by three parameters:

- θ, the disk's angular size which is measured from the rotation curve as shown in Fig. 1.4,
- V_r, the velocity corresponding to the radius r,
- a, the acceleration of the systemic features measured by the velocity drift of the systemic masers ($a = \frac{V_r^2}{r}$). This can be determined by monitoring the spectrum.

The MCP has so far published distance measurements to four galaxies (Reid et al. 2013; Kuo et al. 2013, 2015; Gao et al. 2016), which resulted in a weighted average value of H_0=69.3±4.2 $kms^{-1}Mpc^{-1}$ (Braatz et al. 2018).

In addition to their cosmological importance, studying H_2O -megamaser-disks plays a crucial role in testing the AGN's standard paradigm, explained in the following section.

1.2.2 Investigating jet-disk connection

A unique feature of galaxies hosting H_2O -megamaser-disks is that their sub-parsec accretion disk can be studied using the H_2O -maser emission. As mentioned before, the accretion of

material onto the SMBH is often accompanied by the ejection of material (jets) along the rotation axis of the disk. Studies in the late 90s, have shown that the jets are not necessarily perpendicular to the large scale galactic disk in active galaxies (Pringle et al. 1999; Nagar & Wilson 1999; Kinney et al. 2000; Schmitt et al. 2001). A warp in the accretion disk could cause this, or the gas fueling the SMBH has a different angular momentum direction than that of the gas on a galaxy wide scale. Other studies investigated the position angles (PAs) on different scales and reported that the different PAs do not necessarily align (Schmitt et al. 2002; Greene et al. 2013; Pjanka et al. 2017). In other words, the direction of angular momenta for disks on different scales do not align. When determining the jet directions, we are biased by the viewing angle and corrections are needed. The jets might be moving towards or away from our line of sight and may thus also be affected by Doppler boosting if they reach relativistic speeds. However, if the accretion disk is viewed edge-on, the putative jets should be in the plane of the sky and free of viewing angle biases. In H_2O-megamaser-disk galaxies exhibiting the above mentioned groups of systemic, red- and blueshifted features, the maser disk is viewed edge-on, since the coherent amplification of radiation requires large linear scales. Therefore, we only observe the maser emission if the amplification path is directed towards our line of site. Although H_2O-megamasers are observed mostly in Seyfert 2s, where a dusty obscuring torus surrounds the accretion disk around the AGNs and blocks the view in the optical or near IR regime, the radio waves from the masers can penetrate the obscuring torus and are not affected by extinction. Therefore, H_2O-megamaser galaxies are good laboratories to study the AGN's paradigm, where the central engine accretes matter and the accretion is associated with ejection of material into the space, the so called jets which should be perpendicular to the plane of the disk.

As mentioned above, the host galaxies of H_2O-megamaser-disks are Seyfert 2s and LINERs. In the following sections, I briefly review what an AGN is.

1.3 Active galactic nuclei, a brief history

AGNs were observed for the first time in 1908, by Edward A. Fath. He was observing the spectra of the brightest "spiral nebulae" when he discovered some objects showing broad emission lines that at that time were known to be characteristics of gaseous nebulae. It should be noted that in 1908, it was not yet known that extragalactic objects exist. Herbert Curtis at the Lick Observatory, describes one other nebula (called M 87) in 1918 and mentions not only a lack of spiral arms, but also a straight line of emission connected with the core of the galaxy (Curtis 1918). This was the first reported jet, also at a time when the extragalactic origin of many nebulae were not yet known. Years later, when astronomers knew that the Universe extends beyond our Galaxy and that there are billions of other galaxies, Carl K. Seyfert published a paper (Seyfert 1943) which showed that a fraction of galaxies exhibit broad atomic emission lines which cover quite different degrees of ionization and originate from a small nucleus which look like a star (i.e., it looked point-like on a photographic plate). However these galaxies did not attract attention until the late 1950s, when a source catalog at radio wavelengths led to the discovery of sources which looked like stars on photographic plates but had broad emission lines at unknown wavelengths in their spectra which could not be from a star (the spectra from stars in thermal emission follow Planck's law). Hence these sources were called quasi stellar radio sources (quasars). Later on, the lines were identified as highly redshifted hydrogen emission lines. These high redshift sources also had high luminosity, and the important question was what is the nature of these sources? The most acceptable explanation was reported by Salpeter (1964) and Zel'dovich (1964): the accretion of matter onto a central SMBH is responsible for

the high luminosity of quasars. During the last 70 years, countless number of studies were carried out, with the purpose of understanding the nature of AGNs. Here, we review a few important aspects of these various studies, such as AGN classifications and the unified model of AGNs which try to describe the different observed properties (and consequently the different classes) using only a few fundamental parameters.

1.4 What defines an active galaxy?

AGN hosts are defined as galaxies which contain a massive ($>10^5 M_\odot$) accreting black hole (BH) with Eddington ratios greater than 10^{-5} (Netzer 2015). The Eddington ratio is the ratio of the bolometric luminosity of the galaxy and the Eddington luminosity, where Eddington luminosity is defined as the luminosity at which the gravitational and radiation forces are in balance. Some observational properties are common within the whole family of AGNs. For example, their spectral energy distribution (SED) extends from radio up to γ-rays (i.e. $\sim 10^{12}$ Å to $\sim 10^{-4}$ Å, Elvis et al. 1994, see Fig. 1.5). In comparison, the spectrum of normal galaxies devoid of an AGN is confined to a range from $\sim 2\times10^4$ Å to $\sim 4\times10^3$ Å, since their light is the superposition of stellar and interstellar dust lights. AGN spectra are dominated by emission lines, usually high excitation lines with broad line widths. These emission lines, as well as the continuum emission from AGNs, are highly variable on scales of a few hours to many years, depending on the wavelength of study. This variability is associated to a small nuclear region. AGNs are sometimes strong radio sources ($\sim$ 10% of them, see Sect. 1.5.3) but the best frequency range to search for AGNs is in the X-rays. They are luminous in the X-rays, with a total luminosity of about $10^{12}\,L_\odot$[5](Osterbrock & Ferland 2006). While this is a general definition of an AGN, there are various classes and sub-classes which possess different properties but they all have in common the above mentioned features. In the following section, I will explain some relevant classification and unification schemes of AGNs, referring to relevant references for further detail.

1.5 Active galactic nuclei classification

It is a difficult task to demonstrate a well-established classification of AGNs. There exists a variety of different classifications based on radio or optical luminosities, or the strength of emission lines. Unification schemes try to combine all these different classes into a single one using only a few parameters such as viewing angle, luminosity and Eddington ratio. In the following, I review three main AGN classifications schemes: one based on the spectral properties, another one based on the ratio of radio to optical luminosity, and a third one based on the accretion mode of the central engine.

1.5.1 Type 1 and Type 2 AGNs

One feature plays an important role in the classification of AGNs: the width of the observed emission lines. If the permitted emission lines[6] have widths $\gtrsim 1000\,\mathrm{km\,s^{-1}}$, and the forbidden emission lines[7] with widths $< 1000\,\mathrm{km\,s^{-1}}$ are observed in the spectrum, the galaxies are called

[5] $L_\odot$ denotes solar luminosity, equivalent to 3.828×10^{26} W or 3.828×10^{33} erg s^{-1}.

[6] Permitted lines are transitions of electrons between different levels that are allowed by quantum-mechanical selection rules.

[7] Forbidden lines are those transitions that are not allowed by the electric-dipole quantum-mechanical selection rules, but could occur for example by magnetic-dipole transitions (see e.g., Osterbrock & Ferland 2006). These

Table 1.1: Spectral properties of different classes of AGNs. Table taken from Kamali (2014), based on the lecture notes from the Active Galactic Nuclei course held in the University of Göttingen in winter-semester 2012.

Class	Sub-class	Host Galaxy	Description
Seyfert	Type 1	spirals	strong broad permitted lines, narrow forbidden lines, Fe II lines with width comparable to Hβ, hard X-ray power law with a soft excess
	Type 1.5	spirals	strong broad and narrow lines with comparable strength, weak Fe II lines
	Type 1.8	spirals	weak broad lines
	Type 1.9	spirals	weak Hα, no higher order Balmer lines
	Type 2	spirals	only narrow lines, no Fe II lines, no soft X-ray but hard X-rays
	NLS1[8]	spirals	almost like Sy1 but with narrower Balmer lines (permitted lines are slightly broader than the forbidden ones), stronger Fe II and weaker [OIII] lines, lines are narrow due to the lower black hole mass compared to that of broad line Sy1s
Quasars	Radio-loud	all	strong radio emission, some polarization, broad and narrow emission lines
	Radio-quiet	all	weak radio emission, weak polarization, broad and narrow emission lines
Radio Galaxies	lobe dominated		**FR I**[9]: lower luminosity relative to FR II, brighter in the lobe than the cores, decreasing surface brightness toward the edge **FR II**: more luminous, powerful lobes, jet less obvious, $L_{lobs} \sim L_{core}$ **SSRLQs**[10]
	Core dominated: Blazars	90% in ellipticals	**BL Lacs**[11]: almost absence of emission lines, featureless optical spectrum, rapid variability at all energies even on short scales **OVV quasars**[12]: broad optical emission lines, rapid variability **FSRLQs**[13]: broad emission lines, radio spectral slope $\alpha_r = 0$, higher redshift than BL Lacs
LINERs[14]		all	similar to Sy2 but with low luminosity and low ionization emission lines like [OI], [OII], [NII], [SII]

type 1 AGNs. On the other hand, there are AGNs which lack the broad permitted emission lines in their spectra, and are called type 2 AGNs. Seyfert galaxies which are one of the first classes of AGNs discovered, are also divided into two main sub-classes, i.e., of type 1 and type 2, based on the same criteria (absence or presence of broad emission lines in their spectra). For Seyfert

lines are produced with much reduced intensities compared to permitted lines, and in environments with low densities, these transitions may become observable.

[8] Narrow Line Seyfert 1 (NLS1), see Osterbrock & Pogge (1985)

[9] Fanaroff and Riley (FR), see Fanaroff & Riley (1974)

[10] Steep-Spectrum Radio Loud Quasars (SSRLQs)

[11] BL Lacertae

[12] Optically Violently Variable (OVV) quasars

[13] Flat-Spectrum Radio Loud Quasars (FSRLQs)

[14] Low Ionization Emission-line Regions (LINERs), see Heckman (1980)

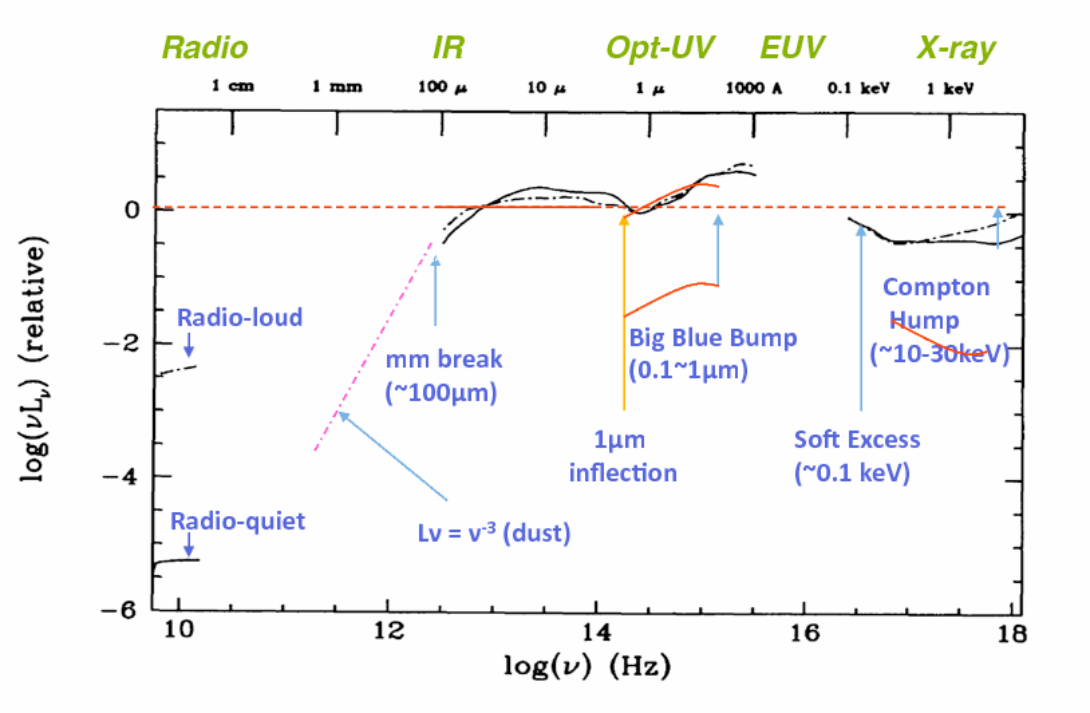

Figure 1.5: Spectral energy distribution of AGNs (Elvis et al. 1994). As seen in this spectrum, the AGN's SED spans from the low energy radio regime to the very high energy X-ray regime.

galaxies, there are also intermediate sub-classes, whose details are presented in Table 1.1. In these intermediate sub-classes, the strength of some broad lines such as Fe II or some hydrogen emission lines, e.g., the Balmer series, are different.

1.5.2 Low excitation and high excitation AGNs

Optical spectroscopic properties are also used to classify AGNs into two classes of high excitation and low excitation AGNs. This classification is based on the existence of strong emission lines in the spectra such as [O II] λ3727, [O III] λ5007 and [Ne II] λ3867, or the existence of weak emission lines such as [O II] λ3727 (Hine & Longair 1979). In general, galaxies with high excitation emission lines are called HEG, and galaxies with low excitation emission lines in their optical spectra are called LEG. Quasars and Seyfert galaxies are HEGs while LINERs belong to the LEG subclass.

1.5.3 Radio quiet and radio loud AGNs

With respect to their properties at long wavelengths, AGNs are also grouped into two classes, those that are radio loud and those that are radio quiet. As the name suggests, the criteria that define to which group an AGN belongs, is the luminosity of the galaxy in the radio regime. The radio loud galaxies produce large scale radio jets and lobes, and the jet contributes a significant fraction to the total bolometric luminosity of the galaxy. The radio loud galaxies make up about 10% of the AGNs and are usually found in ellipticals, while the radio-quiet AGNs prefer spirals (Wilson & Colbert 1995).

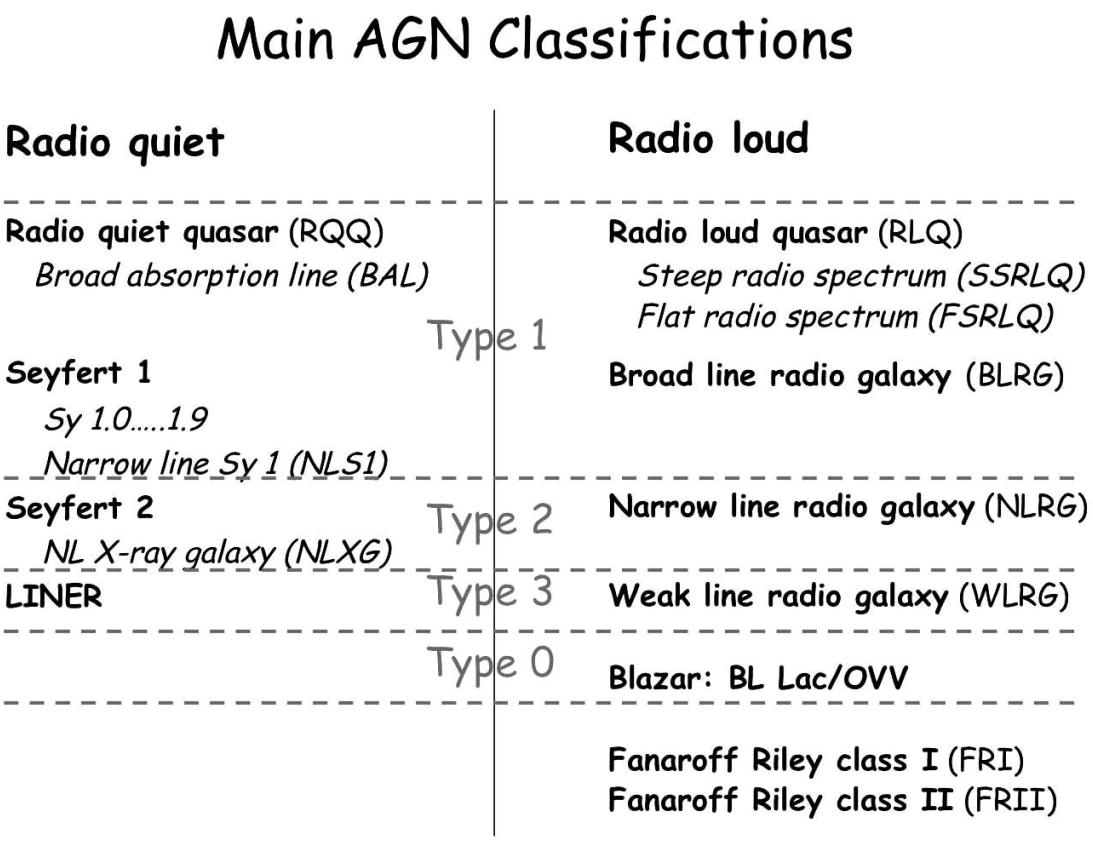

Figure 1.6: Classification of AGNs, taken from Tadhunter (2008).

Traditionally, the radio loudness is defined as the ratio of the monochromatic radio luminosity to the monochromatic optical luminosity (R). For instance, R can be defined as:

$$R = \frac{f\,(5\,\mathrm{GHz})}{f\,(4400\,\text{Å})} \tag{1.3}$$

For radio loud galaxies this ratio is greater than 10 (Kellermann et al. 1989). Fig. 1.6 shows the sub-classes of radio loud and radio quiet AGNs. Seyfert 2s and LINERs which are host to H_2O -megamaer-disks, are among the radio quiet AGNs. Padovani (2016) has argued that the two classes of radio quiet and radio loud AGNs are intrinsically different objects, the major physical difference being lack or presence of relativistic radio jets. Therefore, Padovani (2016) suggested that using the names "radio loud and radio quiet" is misleading, and the subclasses must be called "jetted" and "non-jetted" AGNs. In this work, we stay with the traditional classification of radio quiet/loud AGNs.

1.5.4 Jet mode and radiative mode AGNs

Heckman & Best (2014) suggested that the AGNs could be classified in two groups, based on the dominant energy output resulting from extracting energy from the potential well of a SMBH: AGNs in a radiative-mode or in a jet-mode. In the radiative-mode AGNs, dominant energetic output is in the form of electromagnetic radiation produced by the gas accreted by the SMBH (i.e., from the accretion disk). Jet-mode AGNs produce relatively little radiation from accretion, and energetic output takes the form of the bulk kinetic energy transported in

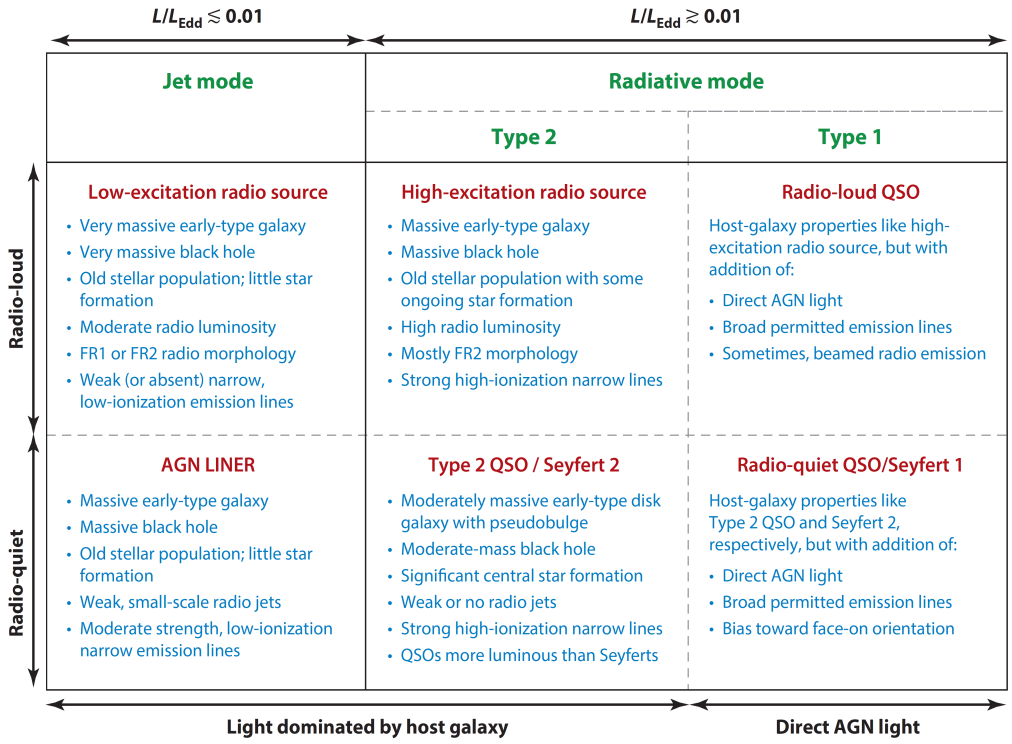

Figure 1.7: AGN classification. Figure taken from Heckman & Best (2014).

collimated outflows. Fig. 1.7 shows the different classifications in an organized and easily readable way.

1.6 A Unification scheme for AGNs

It was suggested in the 1980s, that the two classes of type 1 and type 2 AGNs are the same, but viewed from different angles (Antonucci & Miller 1985; Barthel 1989; Urry & Padovani 1995). In the unified model of AGNs, the central engine is surrounded by obscuring gas and dust, the so called torus. This material is optically thick and when looking through the torus, the broad emission lines are absorbed. However, they can still be seen in the reflected polarized light (Antonucci & Miller 1985). In the unified model of AGNs, blazars are those AGNs where one part of the two-sided jet is directed towards us.

1.6.1 An AGN's dissection in the Unification scheme

The unified model of AGNs suggests that an AGN consists of the following parts (see Fig. 1.8):

- The **SMBH** is the central engine of AGNs characterized by its high mass and small Schwarzschild radius. Figure 1.9 shows the first picture of a dark shadow caused by gravitational light bending and photon capture at the event horizon of the SMBH at the center of galaxy M 87 (Event Horizon Telescope Collaboration et al. 2019).

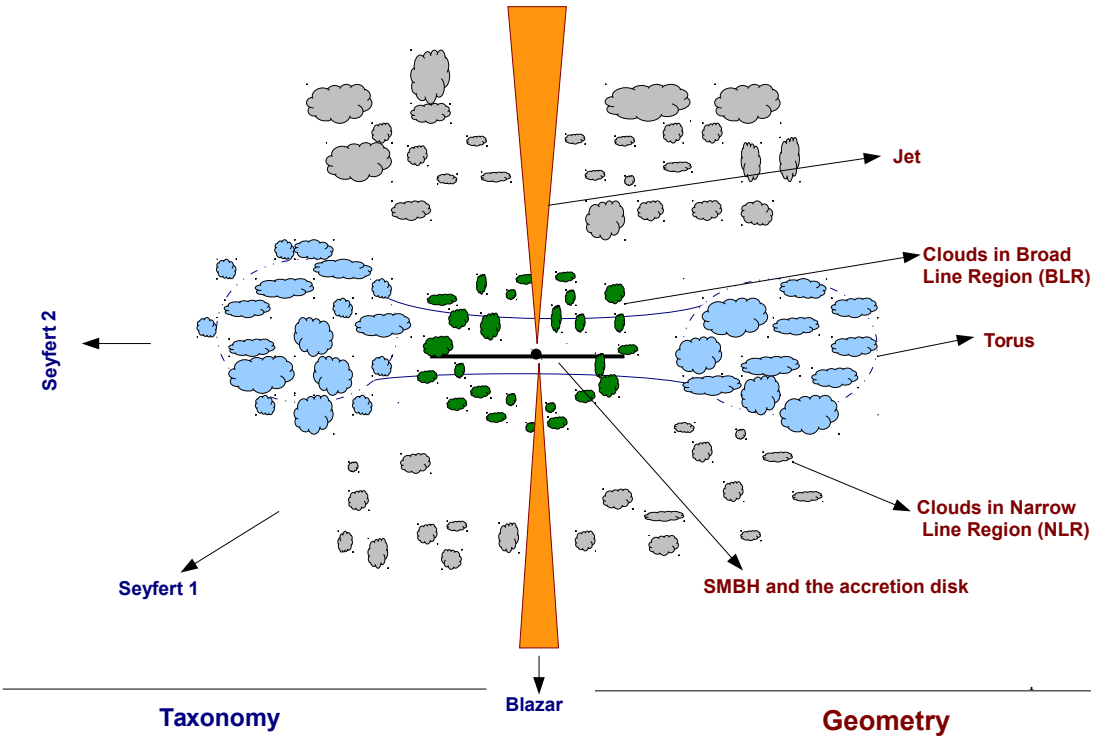

Figure 1.8: Structure of an AGN, where the accretion disk is viewed edge-on and the jets are in the plain of the sky. The viewing angle to the accretion disk is different in Seyfert 2s, Seyfert 1s and blazars as presented in this figure. Different parts of the AGN are not to scale. © FKamali

- The **Accretion disk** is a structure surrounding the SMBH, where the rest mass energy of infalling material is converted into radiation or fast particles (Osterbrock & Ferland 2006). The accretion disk is visible in the optical/ultraviolet (UV) regime, and sometimes also when applying 22 GHz H_2O radio spectroscopy. It is believed that a putative **corona** (which is an atmosphere above the inner accretion disk with unknown geometry) accompanies the accretion disk. The corona is responsible for inverse Compton scattering of the accretion disk photons to X-ray energies (Padovani et al. 2017).

- **Torus** is an obscuring structure surrounding the SMBH. The radiation from the torus peaks in the mid-infrared (MIR). The more modern view of the torus implies that the dust is clumpy and compact, since a smooth dust distribution cannot survive in the region close to the central engine of AGNs (Almeida & Ricci 2017, and references there in). MIR interferometery observations constrain the size and geometry of the torus (see Fig. 1.10).

- The **broad Line Region (BLR)** is in the gravitational potential of the SMBH. The size of this region can vary from a few light hours to a few light days (Kaspi et al. 2005). The electron number densities are $\gtrsim 10^9$ cm^{-3} in this region (Osterbrock & Ferland 2006), therefore no forbidden lines are produced here. Forbidden lines are low probability transitions from atoms which only become relevant in a low density medium.

- The **Narrow Line Region (NLR)** is outside the torus and not in the gravitational potential of the SMBH. Therefore the width of emission lines is smaller, typically ranging from 200 km s^{-1} to 500 km s^{-1}. Both permitted and forbidden lines can form here, due to lower

Figure 1.9: The first image of a black hole, located at the center of the galaxy M 87. This image was constructed using the Event Horizon Telescope. ©Event Horizon Telescope Collaboration.

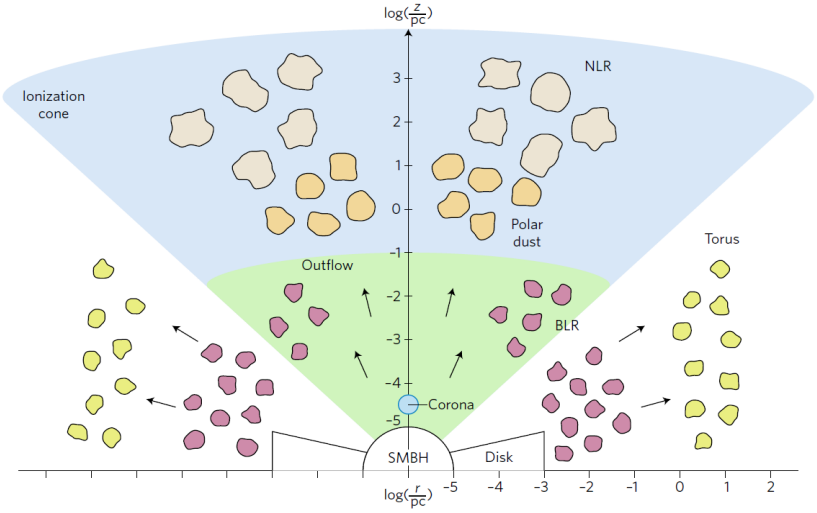

Figure 1.10: AGN's structure seen along the equatorial and polar direction. Different colors indicate different densities or compositions. Figure taken from Almeida & Ricci (2017).

electron densities of order $\sim 10^4 \mathrm{cm}^{-3}$ (Osterbrock & Ferland 2006). The NLR extends to kiloparsec-scales.

- The radio **jets and lobes** are observed in radio loud (or "jetted") AGNs.

1.6.2 Challenges facing the Unification scheme

The unification scheme presented in the late 1980s is currently facing some challenges: true type 2 AGNs are galaxies with broad emission lines not detected in the polarized light. These galaxies represent about 30% of type 2 AGNs in the local Universe, which is considerably a large number (Netzer 2015, and references therein.). The lack of observed broad emission lines in polarized light of these galaxies could indicate that some type 2 AGNs are intrinsically different (i.e., the BLR does not exist). Furthermore, the orientation alone cannot explain the different covering factors measured for type 1 and type 2 AGNs (e.g., Mateos et al. 2016). This implies that the nature of the obscuring tori in type 1 and type 2 AGNs is different.

The radio regime is one of the most salient frequencies to observe the AGNs, because of the high angular resolution provided by interferometric radio observations. More specifically, observing the central region of galaxies at distances > 50 Mpc requires high resolutions which cannot be achieved in the optical, IR or X-rays. However, using radio interferometry we can resolve the pc-scale regions of AGNs without being hindered by obscuration from dust particles, which emit photons at substantially shorter wavelengths than the emission we are studying here at radio wavelengths.

1.7 Radio interferometery: a tool to observe lightyear-scale regions close to the central engine of AGNs

The text in this section is largly based on Parsons (2013), Klein (2014), Condon & Ransom (2016), and Wilson et al. (2009).

The angular resolution of instruments has always been a subject of constant improvement in astronomy. The angular resolution (θ) of a telescope is determined by the wavelength of the observation (λ) and the diameter (D) of the telescope: $\theta \propto \lambda/\mathrm{D}$. When observing in the radio regime, the wavelengths are longer (mm to cm) and to obtain high resolution (i.e., a lower value of θ), one needs to have telescopes with very large diameters. For instance, at 20 cm, with a 100 m single dish telescope, e.g., Effelsberg, the highest resolution that can be achieved is on the order of ~arcminutes. In order to obtain the resolution of 1 arcsecond, we need a diameter of ~ 40 km. However, building fully steerable single dishes with diameters $\gtrsim 100$ m is not achievable with the current technologies. With radio interferometery and aperture synthesis techniques, the distance between two telescopes, called baseline (B), replaces the telescopes diameters and therefore achieving higher resolutions is affordable ($\theta \propto \lambda/\mathrm{B}$). Current interferometers even include baselines as large as the radius of a satellite's orbit moving around the Earth (e.g., the Radio Astron satellite). Here we briefly review the principles of radio interferometry and aperture synthesis. We start with a simple interferometer of two antennas, 1 and 2, separated by a distance of B (see Fig. 1.11). Since the antennas are separated, they will not receive the signals from the sky at the same time. The antenna closer to the source will receive the signal first. The other antenna will receive the signal with a so called geometric delay, τ_g. This delay is equal to $\frac{\mathbf{B}.\mathbf{s}}{c}$, where $\mathbf{B}$ is the base line, $\mathbf{s}$ is the unit vector pointing toward the source and c is the speed of light (we present vectors in boldface). For different sources in the sky, the unit vector $\mathbf{s}$ is different, therefore the geometrical delay will change. Since the astronomical sources are far away, the signals received by the telescopes are plane waves. A signal therefore reaches antenna 1 at time $t - \tau_g = t - \frac{\mathbf{B}.\mathbf{s}}{c}$, and antenna 2 at time t:

$$V_1 = A\,cos\,(\omega\,(t - \tau_g)) \tag{1.4}$$

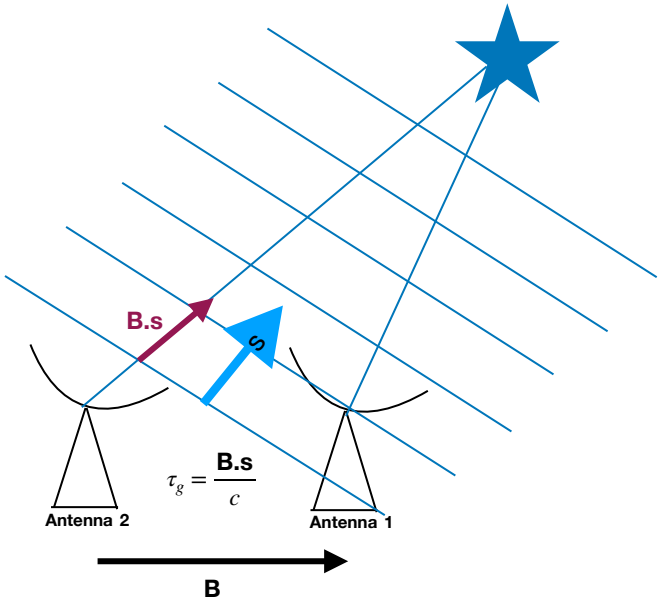

Figure 1.11: A two-element interferometer, consisting of two identical antennas, 1 and 2. The unit vector **s** is pointing towards the source, and the vector **B** is the baseline. Antenna 2 will receive the signal with a delay of $\tau_g = \frac{\mathbf{B.s}}{c}$. © FKamali

$$V_2 = A\,cos\,(\omega\,t) \tag{1.5}$$

where $\omega = 2\pi\nu$ (therefore $\omega\tau_g = 2\pi\nu\tau_g = 2\pi\mathbf{B}.\mathbf{s}/\lambda$), and A is the amplitude. These two signals are correlated, i.e., multiplied and averaged in the so-called correlator, to get the final signal.

$$V_1\,V_2 = A^2\,cos\,(\omega\,t)\,cos\,(\omega\,(t-\tau_g)) = (\frac{A^2}{2})\,(cos\,(2\omega t - \omega\tau_g) + cos\,(\omega\tau_g)) \tag{1.6}$$

The term $cos\,(2\omega t - \omega\,\tau_g)$ is rapidly varying and can be neglected when averaging over a sufficiently large interval ($\Delta t \gg (2\omega)^{-1}$). The correlator's response is:

$$R =< V_1 V_2 >= \left(\frac{A^2}{2}\right) cos\,(\omega\tau_g) = \left(\frac{A^2}{2}\right) cos\left(2\pi\frac{\mathbf{B}.\,\mathbf{s}}{\lambda}\right) = R_{cos} \tag{1.7}$$

This implies that the correlator's output changes sinusoidally across the sky as the source direction changes due to the Earth's rotation. The interferometer is sensitive to different scales depending on the length of the baseline, and only sensitive to the directions perpendicular to the baseline. To receive information on the smaller scale structure of the sources, we need longer baselines, while shorter baselines provide information on the large scale structures. However, since cosine is an even function, it cannot recover the odd part of the source function. We need a sinus response as well, to recover the whole source function. This can be achieved by introducing a 90°phase shift in one of the signals. After correlating as described above, we obtain:

$$R_{sin} =< V_1 V_2 >= \left(\frac{A^2}{2}\right) sin\,(\omega\tau_g) \tag{1.8}$$

We can combine Eq.1.8 and 1.7 into a complex visibility defined as:

$$V \equiv R_{cos} - i\,R_{sin} = Be^{-i\,\Phi} \tag{1.9}$$

where $B = (R_{cos}^2 + R_{sin}^2)^{1/2}$ is the visibility amplitude and $\Phi = tan^{-1}(R_{sin}/R_{cos})$ is the visibility phase. Now we would like to know what the response of our interferometer is to an extended source with brightness distribution of I_ν, which falls into the primary beam of the correlated antennas. In order to understand this, we define new coordinate systems for the baselines on the ground and the source in the sky.

We define $\frac{\mathbf{B}}{\lambda} \equiv (u, v, w)$, i.e., the baseline length in units of wavelength, where u is in east-west direction, v is in north-south direction, and w is the vertical component in the up-down direction. We also define $\mathbf{s} \equiv (l, m, \sqrt{1 - l^2 - m^2})$, i.e., the source unit vector is split into an east-west direction on the sky (l), a north-south direction (m) and a third component that can be written in terms of l and m since $\mathbf{s}$ is a unit vector. For each point on the sky, we have a phase term that is defined by the coordinates on the sky (l, m, $\sqrt{1 - l^2 - m^2}$) and is a function of the baseline (u, v, w). Our visibility is the sum over the two primary beams (of the individual antennas) over the whole sky:

$$V_{(u,v,w)} = \int\int A(l,m)\, I_\nu(l,m)\, e^{-2\pi\, i\,(ul+vm+w\sqrt{1-l^2-m^2})}\, \mathrm{d}l\, \mathrm{d}m \tag{1.10}$$

Separating the w term, we will have

$$V_{(u,v,w)} = \int\int A(l,m)\, I_\nu(l,m)\, e^{-2\pi\, i\,(ul+vm)}.e^{-2\pi\, i\, w\sqrt{1-l^2-m^2}}\, \mathrm{d}l\, \mathrm{d}m \tag{1.11}$$

Here A is the response of the primary beams of the antennas as a function of l and m. The product $A(l, m)\, I_\nu(l, m)$ is called the "perceived sky". Let's assume that our antennas are separated in a two-dimentional plane, thus the w term is zero and can be ignored here. Then we can see that what we observe is the true sky through the response of our antenna. In other words, the visibility is the Fourier transform of the perceived sky; (l, m) and (u, v) are Fourier pairs. The Fourier transform of the image that we made in (l, m) coordinates is called the uv-plane. This uv-plane is sampled by the baselines in our interferometer array. Finally, the inverse Fourier transform of the sampled uv-plane gives us an image. As the Earth rotates, the position of the antennas are changed with respect to the source over time. Therefore, depending on the elevation of the source, circles and ellipses are sampled in the uv-plane, creating more Fourier components of the brightness distribution. This technique is called aperture synthesis. In conclusion, the more data points in the uv-plane, the better the image quality. The uv-coverage depends on the number of antennas and their distribution, the elevation of the sources, and the observation's period.

Next I review what interferometers were used in this work, and give examples of their uv-coverage in Fig. 1.12. The data reduction procedure of our data is explained in each chapter individually.

1.7.1 The interferometers we used in this work

Karl G. Jansky Very Large Array

The Karl G. Jansky Very Large Array (VLA) is an array consisting of 27 antennas, each one 25 meters in diameter, and deployed in a Y-shaped array (see Fig. 1.13). The VLA, which

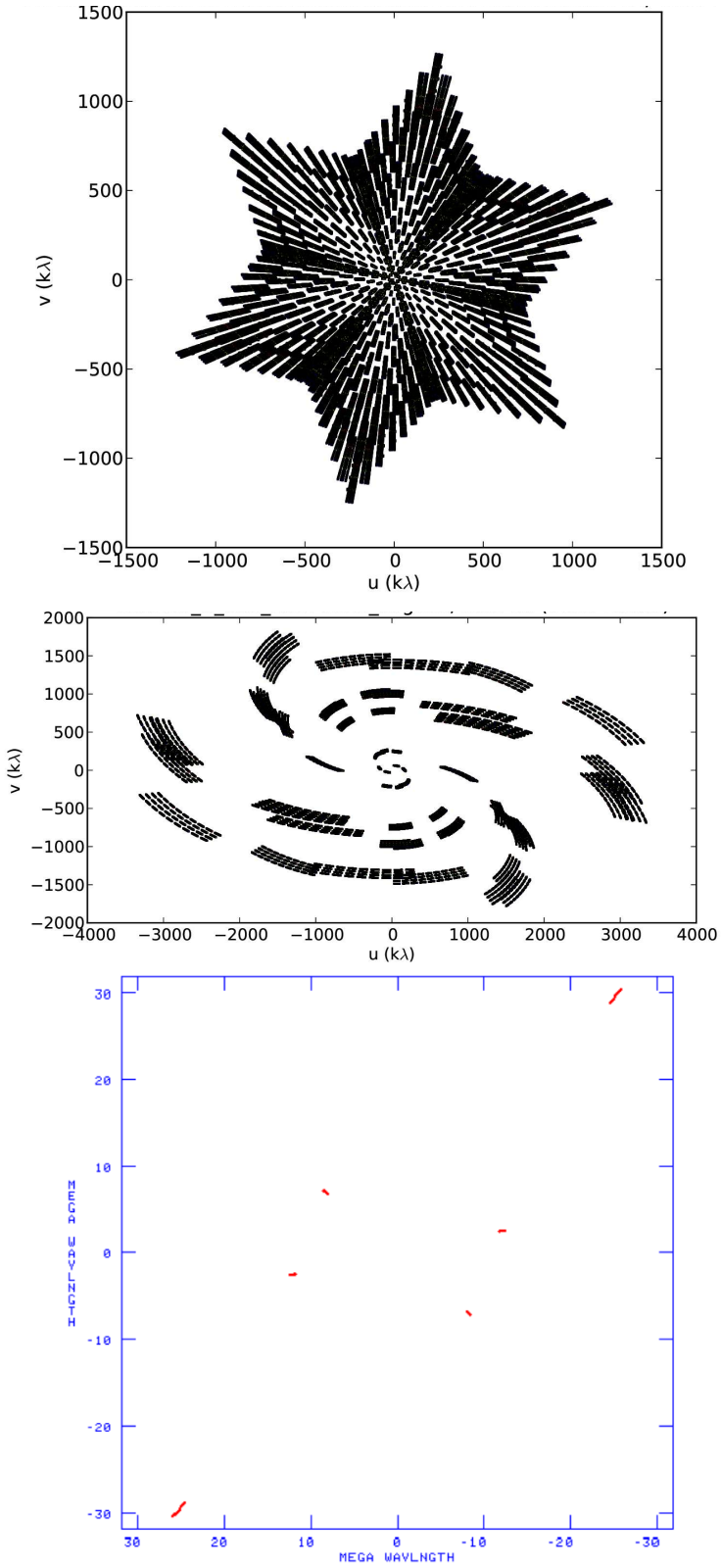

Figure 1.12: UV-coverage for the galaxy Mrk 0001, using three different interferometer arrays we have used in this work: **top**: VLA, **middle**: eMERLIN, **bottom**: VLBA. The number of antennas, their distribution and the integration time of the observations resulted in different uv-coverage.

is located in New Mexico (U.S.), has 4 different configurations, where the maximum baseline varies between 1 km and 36 km.

Figure 1.13: An aerial view of the Karl G. Jansky Very Large Array shows its Y-shape.
© NRAO/AUI/NSF

Very Long Baseline Array

The Very Long Baseline Array is an interferometer consisting of 10 antennas, each 25 meters in diameter, distributed across the U.S. (see Fig. 1.14). The telescopes are controlled remotely from the control center in Socorro, New Mexico. The longest baseline provided by the VLBA is $\sim$ 8000 km, therefore the VLBA observations have very high angular resolution.

Enhanced Multi-Element Radio Linked Interferometer Network

The enhanced Multi-Element Radio Linked Interferometer Network (eMERLIN) is an array consisting of up to 7 antennas with different diameters spread across the UK, providing a longest baseline of $\sim$ 217 km (see Fig. 1.15). The array is operated from the Jodrell Bank Observatory by the University of Manchester. The signals are correlated at Jodrell Bank.

1.8 Contribution of this thesis

In this work, we investigate the standard paradigm of AGNs by studying the radio continuum of H_2O-megamaser galaxies on different scales from sub-parsec to kiloparsec. In addition, we study the alignment of the jets with respect to the rotation axis of the accretion disk, and probe the origin of radio emission in our sample. Furthermore, we search for any correlation between the radio continuum properties of the galaxies and the properties at other frequencies, in order to make future surveys looking for H_2O-megamaser galaxies more efficient. Our sample of 24 H_2O-megamaser galaxies is free of viewing angle biases for the jet, and the maser disk's position angle is measured accurately, providing us with a perfect sample for investigating the

Figure 1.14: The Very Long Baseline Array consists of ten radio telescopes, each with a dish 25 meters in diameter spread over the U.S. © NRAO

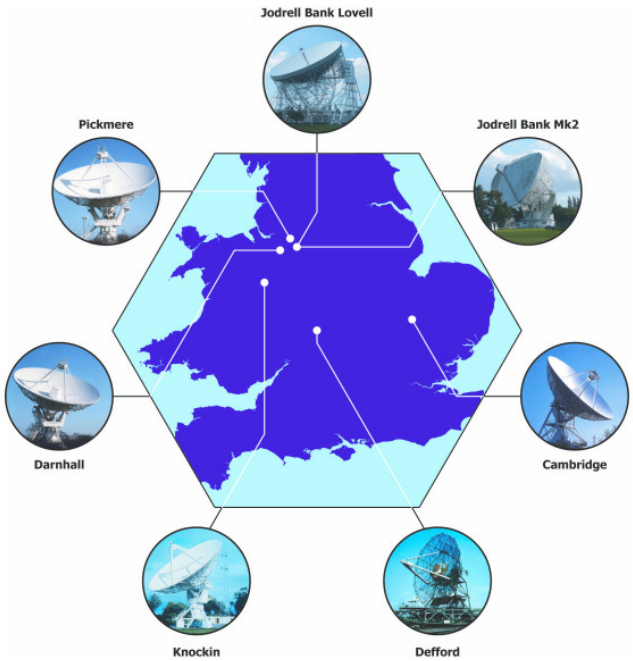

Figure 1.15: The enhanced Multi-Element Radio Linked Interferometer Network, located in the UK, is an interferometer consisting of up to 7 antennas. Image taken from http://www.merlin.ac.uk/.

jet-accretion disk connection.

CHAPTER 2

Radio continuum of galaxies with H_2O megamaser disks: 33 GHz VLA data

The content of this chapter, with the same title, was published as an article in the Astronomy & Astrophysics journal.
Credit: ***F. Kamali et al., A&A, 605, A84, 2017, reproduced with permission ©ESO.***

Abstract

Context. Galaxies with H_2O megamaser disks are active galaxies in whose edge-on accretion disks 22 GHz H_2O maser emission has been detected. Because their geometry is known, they provide a unique view into the properties of active galactic nuclei.
Aims. The goal of this work is to investigate the nuclear environment of galaxies with H_2O maser disks and to relate the maser and host galaxy properties to those of the radio continuum emission of the galaxy.
Methods. The 33 GHz (9 mm) radio continuum properties of 24 galaxies with reported 22 GHz H_2O maser emission from their disks are studied in the context of the multiwavelength view of these sources. The 29–37 GHz Ka-band observations are made with the Jansky Very Large Array in B, CnB, or BnA configurations, achieving a resolution of ~ 0.2 - 0.5 arcseconds. Hard X-ray data from the *Swift*/BAT survey and 22 μm infrared data from WISE, 22 GHz H_2O maser data and 1.4 GHz data from NVSS and FIRST surveys are also included in the analysis.
Results. Eighty-seven percent (21 out of 24) galaxies in our sample show 33 GHz radio continuum emission at levels of 4.5 – 240 σ. Five sources show extended emission (deconvolved source size larger than 2.5 times the major axis of the beam), including one source with two main components and one with three main components. The remaining detected 16 sources (and also some of the above-mentioned targets) exhibit compact cores within the sensitivity limits. Little evidence is found for extended jets (>300 pc) in most sources. Either they do not exist, or our chosen frequency of 33 GHz is too high for a detection of these supposedly steep spectrum features. In NGC 4388, we find an extended jet-like feature that appears to be oriented perpendicular to the H_2O megamaser disk. NGC 2273 is another candidate whose radio continuum source might be elongated perpendicular to the maser disk. Smaller 100–300 pc sized jets might also be present, as is suggested by the beam-deconvolved morphology of our sources. Whenever possible, central positions with accuracies of 20-280 mas are provided. A correlation analysis shows that the 33 GHz luminosity weakly correlates with the infrared luminosity. The 33 GHz luminosity is anticorrelated with the circular velocity of the galaxy. The black hole

masses show stronger correlations with H_2O maser luminosity than with 1.4 GHz, 33 GHz, or hard X-ray luminosities. Furthermore, the inner radii of the disks show stronger correlations with 1.4 GHz, 33 GHz, and hard X-ray luminosities than their outer radii, suggesting that the outer radii may be affected by disk warping, star formation, or peculiar density distributions.

Key words. galaxies: active – galaxies: jets – galaxies: nuclei – radio continuum: galaxies – galaxies: ISM – galaxies: Seyfert

2.1 Introduction

In 1969, the 22 GHz ($\lambda \sim 1.4$ cm) H_2O maser line that is emitted from the water vapor 6_{16}-5_{23} rotational transition was detected for the first time in the Milky Way (Cheung et al. 1969). Since then, this interesting phenomenon has been investigated in a variety of relevant astrophysical environments, also including sources far outside the Milky Way (e.g., Impellizzeri et al. 2008).

One highlight was the discovery of high-velocity H_2O maser emission in the nucleus of NGC 4258, offset by $\pm$ 1000 km s^{-1} from their host galaxy in systemic velocity (e.g., Nakai et al. 1993; Miyoshi et al. 1995; Herrnstein et al. 1999). This led to the discovery of so-called disk masers, which trace subparsec edge-on Keplerian disks that surround supermassive black holes (SMBHs). Later on, the Keplerian motion was used to determine the SMBH masses and direct angular diameter distances. The distance measurement to NGC 4258 is not only independent of the traditional distance ladder, but is also among the most accurate in extragalactic space (Herrnstein et al. 1999; Humphreys et al. 2013). The importance of such direct geometrical extragalactic distance measurements provided the motivation to carry out surveys for finding more H_2O maser disks (e.g., Braatz et al. 2004).

The high accuracy of distances obtained from this method can reduce uncertainties in the Hubble constant. With this idea in mind, the Megamaser Cosmology Project (MCP) was initiated, with the purpose of measuring the Hubble constant with 3% accuracy. In the framework of the MCP, thousands of galaxies have been searched for H_2O megamaser[1] emission. To date, about 160 galaxies with H_2O megamaser emission are known, 39 of which are disk-maser candidates[2] (32 "clean" disk masers, where "clean" means that the maser emission arises from an edge-on Keplerian disk that dominates other emission from nuclear jets or outflows, see Pesce et al. 2015). While the number of disk masers is low, (~1 % of local Seyfert 2s and low ionization nuclear emission region (LINER) galaxies, see, e.g., Van den Bosch et al. 2016, and references therein), their unique geometrical properties, such as an edge-on disk with a putative jet in the plane of the sky, provide motivation to investigate the host galaxies of these H_2O megamaser disks in more detail in order to better understand their nuclear environment. Investigating the radio continuum of these galaxies can reveal emission from inside the maser disks as well as jets or outflows in the vicinity of the central black hole. By definition, these galaxies are particularly suited for studying the accretion disk–jet paradigm under extremely well-defined boundary conditions, including the knowledge of distance, inclination of the accretion disk, and mass of the SMBH.

Here, we present radio continuum data observed at a frequency range centered at 33 GHz (9 mm wavelength) from 24 such disk-maser sources, obtained with the Karl Jansky Very Large Array (VLA)[3]. The purpose of our investigations is to compare the geometry and luminosity of the parsec-scale maser disk with nuclear radio continuum properties, as well as to probe these galaxies for large-scale (kpc scale) radio jets. Resolving structure at kpc scale requires an angular resolution of 0.2-0.5 arcseconds at the distances of our sources. To achieve this resolution, we chose the Ka band of the higher frequency bands, which uses frequencies not too far from the 22 GHz H_2O maser line (to obtain a realistic idea of the radio continuum distribution and intensity near the frequency of the H_2O maser). At the same time, this band minimizes the atmospheric attenuation (which may be stronger at 22 GHz).

[1] Extragalactic masers are about a million times more luminous than many Galactic masers, hence they are called megamasers.

[2] See the MCP webpage: https://safe.nrao.edu/wiki/bin/view/Main/MegamaserCosmologyProject

[3] The Karl Jansky Very Large Array (VLA) is a facility of the National Radio Astronomy Observatory (NRAO), which is operated by the associated universities, Inc., under a cooperative agreement with the National Science Foundation (NSF).

This paper is organized in the following way: in Sect. 3.2 we introduce our sample, and in Sect. 3.3 we describe the data and data reduction. In Sect. 3.4 the 33 GHz continuum maps are presented, followed by analysis and discussion in Sect. 3.5. A summary is given in Sect. 3.6.

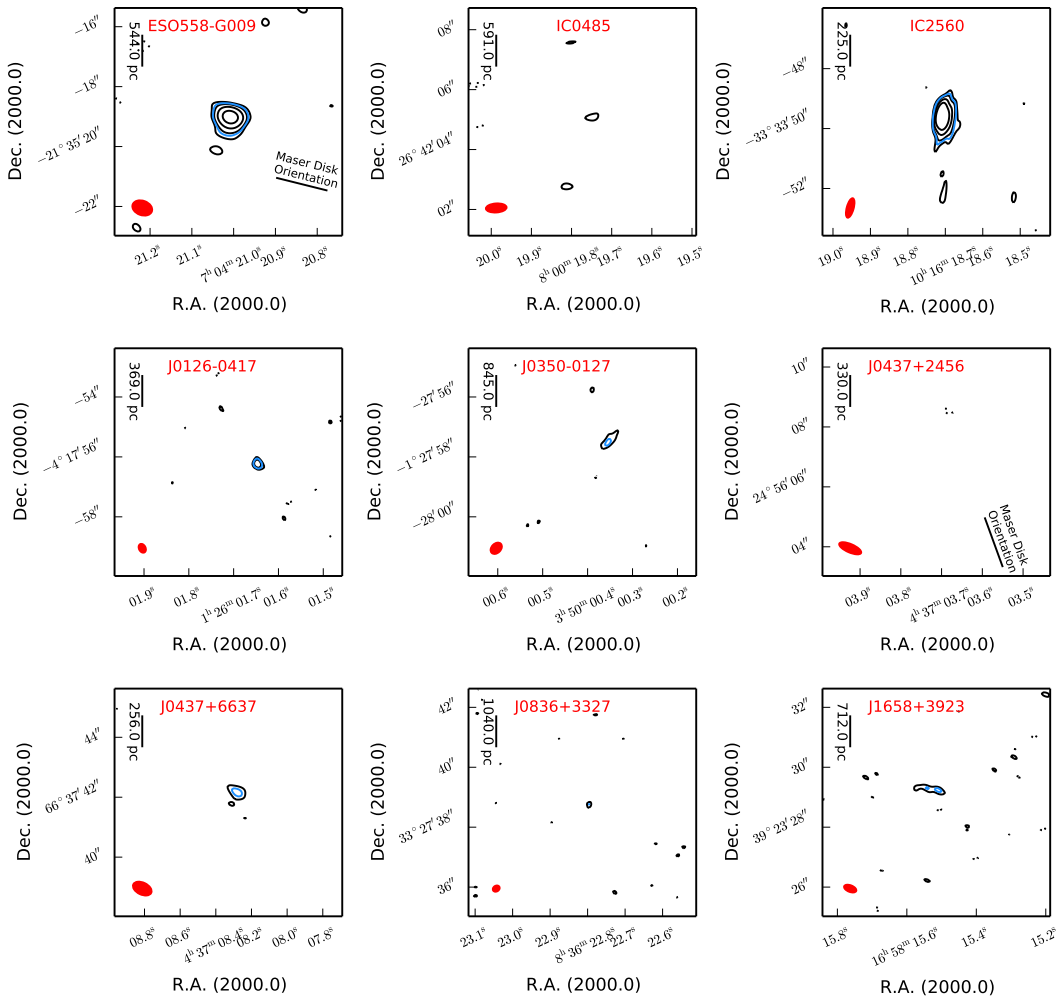

Figure 2.1: 33 GHz contour maps. The contour levels are ±3, ±6, ±12, and ±24 times the rms given in Table 3.3. For convenience, our detection limit of 4.5σ is shown as a blue contour. The synthesized beam is shown in red in the lower left corner of each plot. When available, we also plot the orientation (not the position) of the H_2O maser disk.

2.2 Sample

A total of 39 H_2O disk-maser candidates were identified, mostly by the MCP, until February 2016. We initially selected 30 H_2O disk-maser candidates from those that were known in

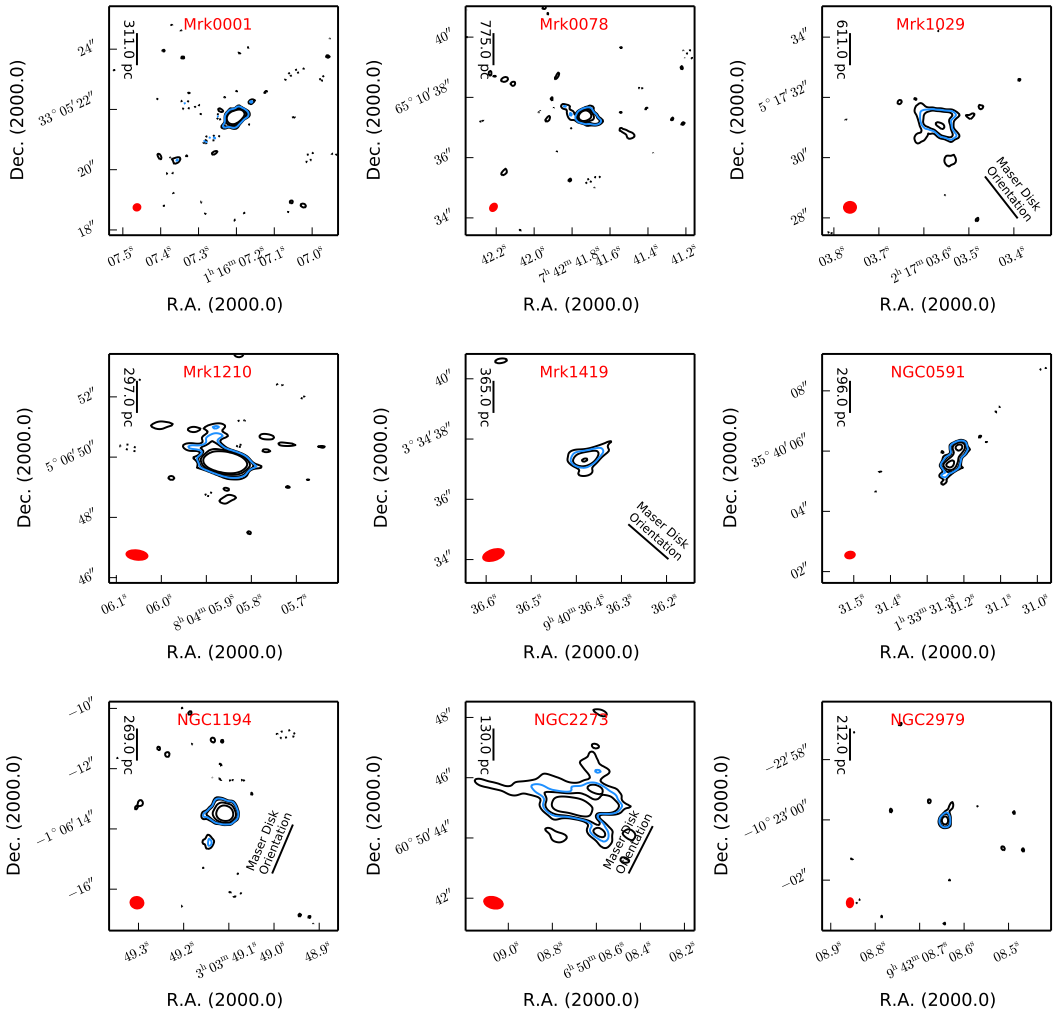

Figure 2.1: *(cont.)*

August 2013. Of this sample, 24 galaxies (see Table 3.1) were observed, with declination (Dec) $> -30^\circ$ and right ascension (R.A.) from 0^h to 17^h. Four H_2O disk-maser candidates with Dec $< -30^\circ$ are not suitable for observation with the VLA. Two more northern galaxies, NGC 4258 and NGC 1068, have been well studied in the past (e.g., Herrnstein et al. 1998; Gallimore et al. 2001) and were therefore also not included in our sample.

Three of the 24 observed galaxies have been monitored with the goal of measuring the Hubble constant (UGC 3789: Braatz et al. 2010, Reid et al. 2013; IC 2560: Wagner et al., in prep.; Mrk 1419: Impellizzeri et al., in prep.), and 13 maser disks were used to measure the SMBH mass ($M_{\rm SMBH}$, see Kuo et al. 2011; Braatz et al. 2015a; Gao et al. 2017). As mentioned before, the distances measured by the MCP are among the most accurate measurements, but they are only available for three sources in our sample. Therefore we adopted the distances from the NASA/IPAC Extragalactic Database (NED)[4] , which are sufficiently accurate for our purposes. The NED distances were obtained using H_0=70.0 km s^{-1} Mpc^{-1}, $\Omega_{\rm matter}$=0.27, and $\Omega_{\rm vacuum}$=0.73 as cosmological parameters. H_2O maser luminosities from the literature were also rescaled to H_0=70.0 km s^{-1} Mpc^{-1} to be consistent with other luminosities in this work.

[4] https://ned.ipac.caltech.edu/

Table 2.1: VLA observations

Galaxy	R.A.	Dec.	Bandpass	Amplitude and	R.A.	δR.A.	Dec.	δDec.
	*J*2000		calibrator	phase calibrator	*J*2000	(arcsec)	*J*2000	(arcsec)
ESO558-G009	07:04:21.02	–21:35:19.2	3C147	J0731-2341	07:04:21.01	0.06	-21:35:19.03	0.05
IC 0485/ UGC 4156	08:00:19.77	+26:42:05.2	3C147	J0748+2400	...	...	...	...
IC 2560	10:16:18.72	–33:33:49.7	3C286	J1018-3144	10:16:18.71	0.16	-33:33:49.60	0.16
J0126-0417	01:26:01.66	–04:17:56.2	3C48	J0115-0127	01:26:01.64	0.04	-04:17:56.23	0.04
J0350-0127	03:50:00.35	–01:27:57.7	3C147	J0339-0146	03:50:00.35	0.15	-01:27:57.40	0.15
J0437+2456	04:37:03.69	+24:56:06.9	3C147	J0426+2327	...	...	...	...
J0437+6637	04:37:08.26	+66:37:42.3	3C147	J0449+6332	04:37:08.28	0.12	+66:37:42.10	0.12
J0836+3327	08:36:22.80	+33:27:38.7	3C286	J0827+3525	...	...	...	...
J1658+3923	16:58:15.50	+39:23:29.3	3C48	J1653+3945	16:58:15.54	0.22	+39:23:29.27	0.20
Mrk 0001/NGC 0449	01:16:07.25	+33:05:22.4	3C48	J0112+3208	01:16:07.20	0.02	+33:05:21.75	0.02
Mrk 0078	07:42:41.73	+65:10:37.5	3C286	J0805+6144	07:42:41.73	0.03	+65:10:37.39	0.03
Mrk 1029	02:17:03.57	+05:17:31.4	3C48	J0224+0659	02:17:03.57	0.18	+05:17:31.15	0.18
Mrk 1210/Phoenix	08:04:05.86	+05:06:49.8	3C147	J0811+0146	08:04:05.86	0.03	+05:06:49.83	0.03
Mrk 1419/NGC 2960	09:40:36.38	+03:34:37.2	3C147	J0948+0022	09:40:36.38	0.14	+03:34:37.36	0.13
NGC 0591/Mrk 1157	01:33:31.27	+35:40:05.7	3C48	J0148+3854	01:33:31.23	0.10	+35:40:05.79	0.11
NGC 1194	03:03:49.11	–01:06:13.5	3C48	J0312+0133	03:03:49.11	0.03	-01:06:13.48	0.03
NGC 2273	06:50:08.66	+60:50:44.9	3C147	J0650+6001	06:50:08.69	0.28	+60:50:45.10	0.27
NGC 2979	09:43:08.65	–10:22:59.7	3C286	J0943-0819	09:43:08.64	0.04	-10:23:00.02	0.04
NGC 3393	10:48:23.46	–25:09:43.4	3C286	J1037-2934	10:48:23.46	0.03	-25:09:43.44	0.03
NGC 4388	12:25:46.75	+12:39:43.5	3C286	J1218+1105	12:25:46.78	0.02	+12:39:43.77	0.02
NGC 5495	14:12:23.35	–27:06:28.9	3C286	J1409-2657	14:12:23.35	0.05	-27:06:29.14	0.06
NGC 5728	14:42:23.90	–17:15:11.1	3C286	J1439-1659	14:42:23.89	1.00	-17:15:10.76	1.00
UGC 3193	04:52:52.58	+03:03:25.9	3C147	J0503+0203	04:52:52.56	0.11	+03:03:25.52	0.29
UGC 3789	07:19:30.92	+59:21:18.4	3C147	J0728+5701	07:19:30.95	0.08	+59:21:18.37	0.08

Notes. Column 1: name of galaxy. Column 2: *J*2000 NED right ascension. Column 3: *J*2000 NED declination. Column 4: bandpass calibrator. Column 5: amplitude and phase calibrators (these are the same for each object). Column 6 and 7: *J*2000 right ascension determined from our radio maps and their uncertainties. Column 8 and 9: *J*2000 declination determined from our radio maps and their uncertainties.

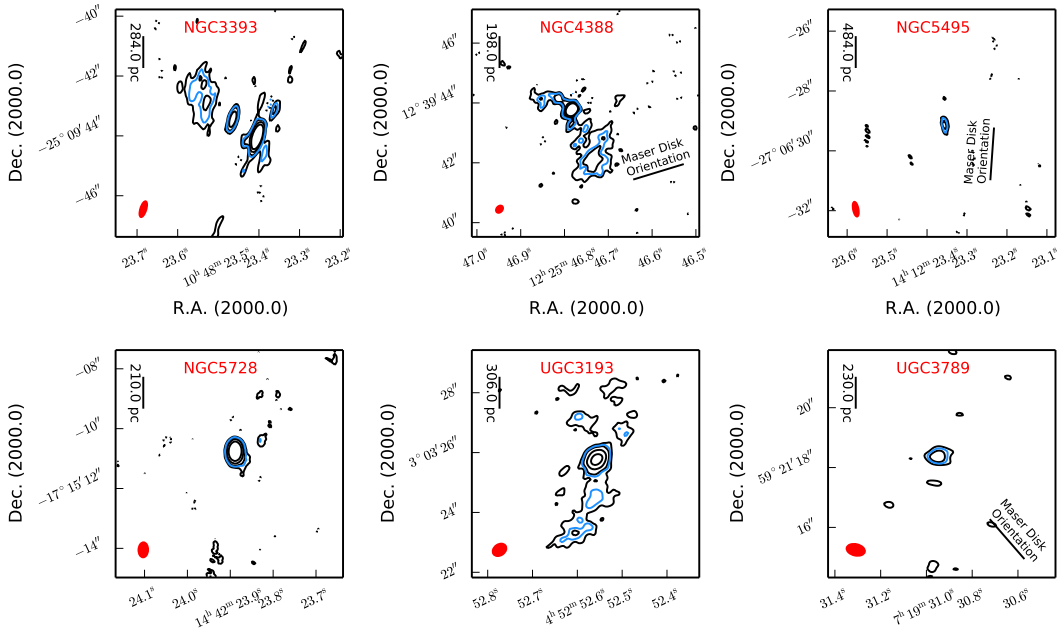

Figure 2.1: *(cont.)*

2.3 Data and data reduction

2.3.1 33 GHz observations and data reduction

Our sample of disk-maser galaxies was observed by the VLA in Ka band (26.5-40.0 GHz) in B, CnB, or BnA configurations using a phase-referencing mode (proposal code: VLA/13B-340). Synthesized full-width at half-maximum (FWHM) beam sizes ranged from 0.19 to 0.50 arcseconds. We used a total bandwidth of 8 GHz (4×2 GHz, from 29 GHz to 37 GHz), full polarization, and 3-bit sampling. The sources were grouped into 12 sets of pairs for observation, with a total time of one hour per pair and an integration time of ∼10 minutes on source per target. Table 3.1 indicates the *J*2000 coordinates, amplitude, phase, and bandpass calibrators. The data were calibrated with the NRAO VLA calibration pipeline, using standard procedures of the Common Astronomy Software Applications (CASA)[5] package (see McMullin et al. 2007). These standard procedures include radio frequency interference flagging, deterministic flagging (e.g., online flags, end channels), opacity and antenna corrections, and bandpass, amplitude and phase calibrations. The majority of our sources was not bright enough for self-calibration (∼1 mJy, see Table 3.3). However, for Mrk 1210, phase and amplitude self-calibration could be performed, which resulted in an improvement of the quality of its radio map. For imaging, the CLEAN algorithm with natural weighting was used. The latter is chosen to maximize the chance of detecting weak compact or slightly extended sources and is hence optimal for detection projects.

[5] http://casa.nrao.edu/

2.3.2 Complementary data

For further analysis and investigation we obtained from the literature 1.4 GHz radio data from the NVSS[6] (Condon et al. 1998), 1.4 GHz data from the FIRST[7] survey (Becker et al. 1995), and hard X-ray data from the *Swift*/BAT satellite in a range of 20-100 keV (Litzinger et al., in prep.), as well as 22 μm (W4) infrared WISE[8] data (Wright et al. 2010). Seventeen of the 24 galaxies in our sample were detected with the NVSS, 8 with FIRST, 13 with *Swift*/BAT, and all 24 with WISE. From radio and X-ray data, the luminosities were calculated using $L = 4\pi D^2 F$, where F stands for flux and D for distance. The infrared luminosities were calculated using $\log(L/L_\odot) = (M_{\odot,\mathrm{W4}} - M_{\mathrm{W4}})/2.5$, where $L_\odot$ is the bolometric luminosity of the Sun, $M_{\odot,\mathrm{W4}}$ is the absolute magnitude of the Sun in WISE W4 band, and M_{W4} is the absolute magnitude of our sources in this band.

2.4 Results

2.4.1 Sample

In this section we present the 33 GHz radio maps for all observed sources, centered at their NED positions, as well as a table of derived source properties. Important in this context is that our linear resolution in pc for a 0.2″ beam size is close to the distance of the galaxies measured in units of Mpc, that is, (linear resolution / pc) ≈ (D / Mpc). Therefore, our beam typically covers ∼100 pc, but with large deviations to either side. This implies that even the central beam contains not only a galaxy's very center, but also the surrounding environment, which may contain star-forming regions and supernova remnants that also contribute to activity and radio continuum emission.

Figure 2.1 presents the 33 GHz contour maps for our sample, where the contour levels are ±3, ±6, ±12, ±24 times the root-mean-square noise (rms) of an emission-free field in the CLEANed image (see Table 3.3 for the sensitivities). Since our detection limit is 4.5σ, a contour level of this value is also shown in Fig. 2.1 (in blue), to facilitate distinguishing between a weakly detected source and an undetected source. Figure 2.1 clearly shows the large number of sources exhibiting a compact core without much additional structure. While our classification depends on limited signal-to-noise ratios and is thus sometimes debatable, we count 16 such compact sources, where "compact" used here and in the following denotes a beam-convolved (and deconvolved) major axis smaller than 2.5 times the beam major axis. One source shows two main components, another source three main components, and three other sources exhibit extended emission. We note that the sources with two or three main components also contain compact cores, as do some of the extended sources.

Only three of the 24 galaxies (IC 485, J0437+2456, and J0836+3327) were not detected at 33 GHz at a level of 4.5 σ or higher. Two of these galaxies, IC 485 and J0836+3327, are at relatively large distances of 122 Mpc and 214 Mpc, respectively. IC 485 was detected with a flux density of 3.01 mJy, and J0836+3327 with 1.95 mJy by FIRST. Adopting a mean spectral index of 0.73 obtained in this work (Sect. 2.5.2) between FIRST 1.4 GHz and our 33 GHz observations[9], flux densities of ∼0.30 mJy and ∼0.19 mJy are expected to be observed at 33 GHz for IC 485 and J0836+3327, respectively. These flux densities are still higher than our 4.5 σ detection threshold. Therefore, these sources may have spectral indices steeper than 1.0.

[6] NRAO VLA Sky Survey, http://www.cv.nrao.edu/nvss/
[7] Faint Images of the Radio Sky at Twenty-cm, http://sundog.stsci.edu/
[8] Wide-Field Infrared Survey Explorer (WISE). See http://wise.ssl.berkeley.edu/
[9] Assuming a power-law dependence for the continuum flux density given by $S \propto \nu^{-\alpha}$, see Sect. 2.5.2.

Table 2.2: Sample properties.

Galaxy	Distance (Mpc)	33 GHz flux (mJy)	rms (μJy/beam)	NVSS flux (mJy)	FIRST flux (mJy)	IR magnitude	hard X-ray flux (10^{-11}erg s^{-1} cm^{-2})	log L_{H_2O} ($L_\odot$)	Type of activity
ESO558-G009	112.2 ± 7.9	0.80 ± 0.04	18.6	12.8±0.6	...	8.793	<0.34	2.9	*U*
IC 0485	122.0 ± 8.5	...	18.9	...	3.01	9.406	$1.75^{+0.19}_{-0.18}$	3.1	*U*
IC 2560	46.4 ± 3.3	2.00 ± 0.10	17.3	32.0±1.7	...	9.294	$0.41^{+0.12}_{-0.13}$	2.1	Sy2
J0126-0417	76.2 ± 5.4	0.13 ± 0.01	9.9	...	...	8.930	<0.34	2.1	*U*
J0350-0127	174.2 ± 12.2	0.14 ± 0.02	12.0	...	...	8.529	$0.45^{+0.17}_{-0.16}$	3.7	*U*
J0437+2456	68.1 ± 4.8	...	17.7	...	...	9.024	<0.41	2.3	*U*
J0437+6637	52.9 ± 3.7	0.11 ± 0.02	16.8	3.8±0.6	...	8.934	0.29±0.14	1.4	*U*
J0836+3327	214.6 ± 15.0	...	30.9	...	1.95	9.145±0.459	<0.33	3.6	Sy2
J1658+3923	146.8 ± 10.3	0.18 ± 0.04	13.4	...	3.64	9.513	<0.30	2.9	Sy2
Mrk 0001	64.2 ± 4.5	3.96 ± 0.12	10.8	75.9 ± 2.3	...	9.105	<0.32	1.9	Sy2
Mrk 0078	159.9 ± 11.2	1.75 ± 0.11	13.7	36.9±1.2	...	8.975	0.63 ± 0.18	1.6	Sy2
Mrk 1029	126.0 ± 8.8	1.18 ± 0.14	17.7	11.9±0.6	8.12	8.799	<0.35	2.8	*U*
Mrk 1210	61.3 ± 4.3	9.58 ± 0.08	17.9	114.9±3.5	...	8.523	3.58±0.20	2.0	Sy2, Sy1
Mrk 1419	75.3 ± 5.3	0.36 ± 0.06	16.0	7.4 ±0.5	5.13	8.790	<0.34	2.7	LINER
NGC 0591	61.1 ± 4.3	1.52 ± 0.07	13.6	33.3±1.1	...	8.566	$0.37^{+0.12}_{-0.11}$	1.5	Sy2
NGC 1194	55.4 ± 3.9	1.08 ± 0.04	13.0	...	1.49	8.807	2.21±0.18	2.8	Sy 1.9
NGC 2273	26.8 ± 1.9	2.69 ± 0.29	26.3	63.4±2.4	...	9.734±0.511	0.67 ± 0.16	0.9	Sy2
NGC 2979	43.8 ± 3.1	0.36 ± 0.04	14.0	15.7±1.0	...	9.158	<0.36	2.2	Sy2
NGC 3393	58.6 ± 4.1	5.30 ± 0.36	18.5	81.5±3.3	...	8.846	1.56±0.19	2.7	Sy2
NGC 4388	40.8 ± 2.9	8.57 ± 0.43	17.9	120.4±4.7	45.02	8.814	$15.81^{+0.16}_{-0.15}$	1.2	Sy2
NGC 5495	99.8 ± 7.0	0.13 ± 0.02	15.4	12.5± 1.3	...	9.301	<0.40	2.4	Sy2
NGC 5728	43.3 ± 3.1	2.27 ± 0.06	28.1	70.8±2.9	...	9.126	5.20±0.20	2.0	Sy2
UGC 3193	63.2 ± 4.4	3.95 ± 0.27	14.4	17.7±0.7	...	8.942	<0.39	2.5	*U*
UGC 3789	47.4 ± 3.3	0.21 ± 0.02	14.9	17.6± 1.0	14.43	8.326±0.142	$0.26^{+0.14}_{-0.13}$	2.7	Sy2

Notes. Column 1: name of galaxy. Column 2: Hubble flow distances (relative to the 3 K CMB), assuming H_0=70 km s^{-1} Mpc^{-1} (see Sect. 2). Column 3: 33 GHz integrated flux densities with uncertainties. The errors given in those cases are formal values and do not show the real level of uncertainty. Column 4: root mean square noise level of the clean image. Column 5: NVSS integrated flux. Column 6: FIRST integrated flux. Column 7: IR (WISE, W 4) magnitude. In our analysis, a 10% uncertainty on the magnitude is assumed for those cases where the uncertainty is not given in the literature. Column 8: *Swift*/BAT hard X-ray fluxes (20-100 keV) with uncertainties (Litzinger et al., in prep). Column 9: logarithm of water maser luminosity (isotropy assumed, Zhang et al. 2012), modified for H_0=70 km s^{-1} Mpc^{-1}. In our analysis, 10% uncertainty on the luminosity is assumed. Column 10: types of nuclear activity after NED; U stands for unidentified.

The third source, J0437+2456, is closer (68 Mpc), but remained undetected by both NVSS and FIRST.

With 21 galaxies detected at Ka band (29-37 GHz), 87% of the galaxies in our sample show radio emission at levels of 4.5 σ to 240 σ. The 33 GHz continuum luminosity distribution is presented in Fig. 2.2.

Furthermore, our 33 GHz maps have improved the accuracy of the central coordinates of some galaxies in our sample. We identify the compact radio sources as the galactic nuclei. After fitting two-dimensional Gaussians (in the image domain) on the central component, the central position of the Gaussian fit is adopted as the new position of the center of the respective galaxy. These new radio coordinates and their uncertainties are presented in Table 3.1. Our position uncertainties take into account statistical uncertainty, the uncertainty of the phase calibrator position, and systematic uncertainties. The systematic uncertainty was approximated from $(B^2 + \Psi^2)^{1/2} \times (1/\mathrm{SNR} + 1/20)$, where B is the beam size, Ψ is the source major axis, and SNR is the signal-to-noise ratio of the map (for more details see White et al. 1997). For 10 galaxies in our sample, interferometrically determined coordinates from the maser emission are also available (Kondratko et al. 2006b, 2008; Kuo et al. 2011; Gao et al. 2017). The central positions obtained in this work and those obtained from maser emission deviate on average by 121 ± 107 mas (milliarcseconds) and are mostly in agreement within the limits provided by beam size and signal-to-noise ratio (S/Ns). See Table 2.3 for a comparison of our determined positions and the H_2O maser positions. Noteworthy deviations beyond the 3σ level are found for ESO 0558–G009, NGC 1194, Mrk 1419, and NGC 4388, all sources where at least slightly extended emission is found in our continuum data. For two sources, Mrk 1029 and NGC 5495, our coordinates have lower uncertainties than those of the maser positions.

In Tables 3.3 and 2.4 we list the derived properties of the sources. Flux density and position angle (P.A.) have been determined by two-dimensional Gaussian model fitting on a region containing all the significant emission. For sources with more complex radio morphologies, multiple Gaussians were fitted in order to have a better estimate of the fluxes (NGC 0591, NGC 3393, NGC 4388, UGC 3193). In what follows we mention some relevant properties of these galaxies such as their morphology, activity type, or other interesting features that are discussed in the literature together with some basic properties that can be extracted from our maps. Statistical properties are discussed in Sect. 5.

2.4.2 Individual sources

ESO558-G009 is an Sbc galaxy. The MCP reported rapid intra-day variability in the maser spectrum, which was interpreted as the result of interstellar scintillation (Pesce et al. 2015). Compact radio emission is observed in our 33 GHz map. A two-dimensional Gaussian fit (Table 2.4) provides a formal P.A. of 155°±33°. Gao et al. (2017) reported a P.A. of 256°±2° (redshifted side, here and elsewhere) for the maser disk. While this might indicate that the radio continuum elongation and the maser disk are almost perpendicular (separated by 101°±33°), this needs to be verified by additional mesurements.

IC 0485 is an Sa Seyfert 2 galaxy. Radio continuum emission was not detected at 4.5 σ or higher levels (but it is tentatively detected at the 3.5 σ level). As mentioned before, the galaxy is at a relatively large distance of 120 Mpc.

IC 2560 is an SBb Seyfert 2 galaxy. Ishihara et al. (2001) reported a *J*2000 22 GHz peak radio continuum position of RA = 10h16m18.710s±0.006s and Dec = –33d33m49.74s±0.″01 (±1pc). The blueshifted maser features spatially coincide with the 22 GHz continuum component and are interpreted as jet maser emission (Ishihara et al. 2001). A peak and an integrated flux

density of 1.8 ± 0.3 mJy/beam and 1.7± 0.5 mJy, respectively, were reported by Yamauchi et al. (2012) at 22 GHz. The nearly edge-on Keplerian disk with a position angle of –46° is almost perpendicular to the large-scale galactic disk (Ishihara et al. 2001). This means that the rotation axis of the maser disk and that of the large-scale galactic disk are nearly perpendicular. Compact radio emission is observed in our 33 GHz radio map, where the peak position agrees within the uncertainties with the position of the 22 GHz continuum peak reported by Yamauchi et al. (2012).

J0126-0417 has compact radio continuum emission detected in our 33 GHz map.

J0350-0127 is a (within the errors) compact source detected in our 33 GHz map; this most likely represents the nucleus.

The source *J0437+2456* is not detected at 33 GHz.

The source *J0437+6637* is detected in our 33 GHz map and is unresolved in our Gaussian deconvolution.

J0836+3327 is a Seyfert 2 galaxy. No radio continuum was detected at a 4.5 σ or higher level in our 33 GHz map (but it is tentatively detected at a 4 σ level).

J1658+3923 is an Sc Seyfert 2 galaxy. A slightly extended radio continuum source is observed in our map.

Mrk 0001 is an SBa Seyfert 2 spiral galaxy. Omar et al. (2002) observed H I emission from Mrk 1 and interpreted its morphology as due to a tidal interaction with its nearby companion NGC 451. The authors also reported that the line of sight toward the nucleus of Mrk 1 is rich in both atomic and molecular gas, or in other words, that it is heavily obscured. Compact 33 GHz radio emission is observed in our map.

Mrk 0078 is classified as an SB Seyfert 2 galaxy. The narrow line region (NLR) of this galaxy is affected by a strong jet-gas interaction, and spectroscopic observations have shown that its narrow emission lines are double peaked (Sargent 1972; Adams 1973). Based on optical and 3.6 cm VLA images, Whittle & Wilson (2004) suggested that Mrk 78 is a post-merger system, with a highly extended asymmetric gas distribution and a nuclear dust lane. The radio nucleus lies within this highly obscuring dust lane (Whittle & Wilson 2004). Slightly extended radio emission might be detected east and west of the center of our 33 GHz map, but the S/Ns are low, so that this source is also rated compact.

Mrk 1029 shows extended radio emission in our 33 GHz map with a P.A. of 59°±11°. Gao et al. (2017) reported a P.A. of 218°±10° for the maser disk. While we consider our position angle as uncertain in spite of the low formal error, it would suggest that maser disk and radio continuum have approximately the same orientation (separation of 21°±15°).

Mrk 1210, also known as the Phoenix galaxy, is an amorphously looking spiral galaxy that has been classified as both Seyfert 1 and Seyfert 2. Former studies have confirmed a double structure, a core, and a southeastern jet component (Middelberg et al. 2004). Spectroscopic findings support the presence of a nuclear outflow instead of a hidden broad line region (Mazzalay & Rodríguez-Ardila 2007). A flux density of 36.28 ± 1.95 mJy at 5 GHz was reported by Xanthopoulos et al. (2010). We observe compact emission in our 33 GHz map within the uncertainties.

Mrk 1419, also known as NGC 2960, is an Sa galaxy. Mrk 1419 hosts a LINER nucleus. The P.A. of the maser disk is 49°, and the disk inner and outer radii are 0.13 pc and 0.37 pc, respectively (Kuo et al. 2011). Sun et al. (2013) reported an extension in the 20 cm radio map at a P.A. of 125°± 10 °. This extension may suggest that a jet is launched from the central black hole. In our 33 GHz map, the radio emission may show a slight extension in the northwest-southeast direction, with a P.A. of 117°±84°. Nevertheless, we rate the source as compact.

NGC 0591 is an SB0/a Seyfert 2 galaxy. Near-infrared spectral studies of stellar and gas kinematics of NGC 591 show that the gas has two kinematic components: one is located inside the plane of the galaxy with similar rotation to that of stellar motion, and the other is forming an outflow that is oriented along the radio jet directed toward the northwest from the nucleus (Riffel & Storchi-Bergmann 2011). Our 33 GHz map shows two peaks with a separation of ∼ 0.66 arcsec, more precisely, with an R.A. separation of 360 mas and a Dec separation of 550 mas at a position angle of about –34°. The central component has a flat spectrum with α_{30}^{36}=0.54±0.44 that possibly is the radio core, while the northwestern component is characterized by α_{30}^{36}=1.39±0.63. Such a steep spectrum suggests the presence of a jet as the source of radio emission, which is consistent with the above-mentioned gas kinematics of NGC 591 obtained at other wavelengths.

NGC 1194 is an S0-a Seyfert 1.9 galaxy. Of the galaxies with a determined nuclear mass in our sample, this galaxy has the most massive nuclear core, $M_{\rm SMBH} = (6.5\pm0.3) \times 10^7 M_\odot$ (Kuo et al. 2011). The position angle of the maser disk is 157° east of north and the inclination is ∼ 85°(Kuo et al. 2011). Compact radio emission is detected in our 33 GHz map.

NGC 2273 is an SBa Seyfert 2 galaxy. The H_2O maser in NGC 2273 is the least luminous of our sample with $L_{H_2O} < 10\,L_\odot$. Petitpas & Wilson (2002) reported a nuclear stellar bar with a P.A. of 45° that is located approximately perpendicular to the large-scale galactic bar with a P.A. of 115°. However, Erwin & Sparke (2003) found evidence for a circumnuclear disk. Greene et al. (2013) suggested the presence of an inner ring that manifests itself as a spike in the ellipticity profile of the inclined main galactic body at a galactocentric distance of ∼150 pc. The dust lanes interior to the ring are most readily identified with spiral arms. In our 33 GHz map we observe extended emission, with a P.A. of 82.8°± 2.8°. The P.A. of the maser disk is 153° (Kuo et al. 2011), which indicates that our radio continuum and the maser disk are misaligned by ∼70°.

NGC 2979 is an SABa Seyfert 2 galaxy. Our 33 GHz image shows compact radio continuum emission.

NGC 3393 is an SBa Seyfert 2 galaxy. Fabbiano et al. (2011) reported X-ray (3-8 keV) observations of this system and provided evidence for the existence of a binary black hole system. However, deep Chandra imaging, combined with adaptive optics and radio imaging (Koss et al. 2015), suggest a single heavily obscured radio-bright active galactic nucleus (AGN). VLA observations at 8.6 GHz (A configuration) have shown a system that consists of four radio components; one at the center, one displaced to the southwest, and two very close components to the northeast (see Schmitt et al. 2001). In our 33 GHz observations with approximately the same synthesized beam width, we see three components: one at the center, one toward the southwest, and one located to the northeast. That we see not two sources, like Schmitt et al. (2001) in the latter case, may be due to the limited S/N of this component. Our spectral analysis shows α_{30}^{36}=1.69±0.1.46 for the central component, α_{30}^{36}=2.66±3.2 for the northwestern component, and α_{30}^{36}=0.84±0.29 for the southeastern component. The high uncertainty of the indices for the central and northwestern components do not allow us to draw a conclusion on the nature of the sources. However, an index of 0.84±0.29 for the southeastern component could be indicative of radio emission from a jet. In addition, Kondratko et al. (2008) observed the H_2O maser emission in the central part of the NGC 3393, and showed that the maser disk is oriented perpendicular to both kpc-scale jet and the axis of the NLR.

NGC 4388 is an Sb edge-on Seyfert 2 galaxy. NGC 4388 is known to have a biconical narrow line region (Pogge 1988; Corbin et al. 1988, Wilson et al. 1993). The maser disk has a P.A. of 107° (Kuo et al. 2011). The kiloparsec-scale disk has a P.A. of 90° and the more nuclear stellar disk has a P.A. of 75° (Greene et al. 2014). Damas-Segovia et al. (2016) reported a southern jet

with a scale of 1 kpc. Extended radio emission is observed in our 33 GHz map with a P.A. of $24^{\circ}\pm54^{\circ}$ (Table 2.4). The large error in the latter value is mainly caused by the bending of the jet, visible in Fig. 2.1. Thus maser disk and the extended radio emission seen in our data are oriented almost perpendicular to each other.

NGC 5495 is an SABc Seyfert 2 galaxy. H_2O maser emission was detected by Kondratko et al. (2006a) with an orbital velocity of ~ 400 km s^{-1}. Gao et al. (2017) reported a P.A. of $176^{\circ}\pm5^{\circ}$ for the maser disk. Compact 33 GHz emission is observed in our map.

NGC 5728 is an SBa Seyfert 2 galaxy. Similar to NGC 4388, this galaxy is known to have a biconical narrow line region (Pogge 1988; Corbin et al. 1988, Wilson et al. 1993). Our 33 GHz map shows compact radio continuum at the central NED position.

UGC 3193 is an SBb galaxy. Extended 33 GHz emission, mainly oriented along an axis from north to south, is observed together with a compact core at the center of our map.

UGC 3789 is an SABa Seyfert 2 galaxy. There is optical evidence for a circumnuclear disk. An inner ring is visible as a spike in the ellipticity profile, and dust lanes are located interior to the ring, which are most readily identified with spiral arms (Greene et al. 2013). The well-studied maser disk traces rotation speeds of up to ~ 750 km s^{-1} (Braatz & Gugliucci 2008; Braatz et al. 2010; Reid et al. 2013). The MCP has measured an angular-diameter distance of 49.6 ± 5.1 Mpc for this galaxy (Reid et al. 2013), which is compatible with the value given in Table 3.1. The P.A. of the maser disk is 41° east of north (Kuo et al. 2011). The inner and outer radii of the disk are 0.08 pc and 0.30 pc, respectively. UGC 3789 has a black hole mass of $(1.4\pm0.05)\times 10^7\ M_{\odot}$ (Kuo et al. 2011). In addition, Castangia et al. (2013) classified UGC 3789 as a Compton-thick galaxy ($N_{\rm H} > 10^{24}\ cm^{-2}$). Radio emission is observed at the center of our 33 GHz map. While its nominal P.A. is $117^{\circ}\pm22^{\circ}$ (see Table 2.4), the 33 GHz radio continuum source is too compact with respect to our resolution to discuss any potential alignments.

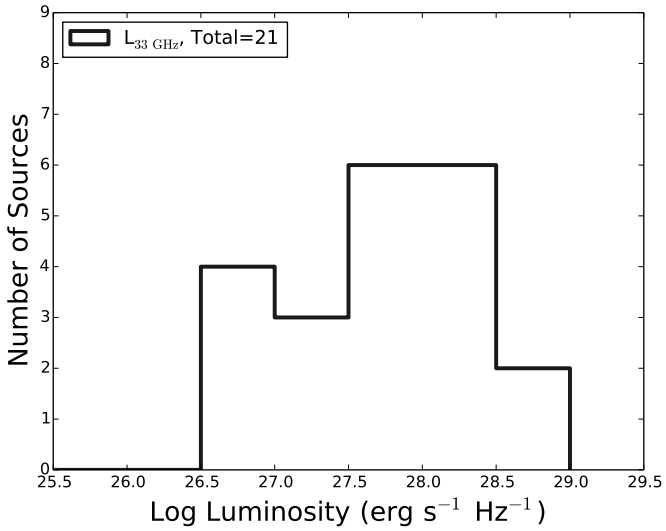

Figure 2.2: 33 GHz luminosity distribution for the 21 clearly detected targets.

2.5 Analysis and discussion

After reviewing the individual 33 GHz maps, here we discuss our results in more detail. First we analyze the encountered morphologies and spectral indices obtained for the detected sources, and then we discuss possible correlations between various physical quantities by addressing the galaxies and in particular their nuclear regions. In order to do so, we applied linear fits, accounting for errors along both axes, and a Spearman rank correlation test. Slopes and intercepts of the fits, correlation coefficients, and P-values, denoting the likelihood that the parameters are unrelated, are shown in a corner of most plots. One purpose of this analysis, in addition to identifying correlations, is to increase the chance of disk-maser detections in future surveys.

2.5.1 33 GHz morphologies - where are the jets?

As explained in Sect. 2.4.1, the bulk of our 33 GHz maps contain compact cores and clearly asks for higher resolution studies at lower frequencies, where higher fluxes may be expected. Interestingly, two of the seven sources with $D > 100$ Mpc (J1658+3923 and Mrk 1029) show extended emission. Perhaps there is even a third, Mrk 78. Apparently, the linear extent of the central emission can vary strongly, from $\lesssim$50 pc in some compact nearby sources (e.g., NGC 2979) to ~600 pc in Mrk 1029. J0350-0127, J1658+3923, and Mrk 78 might show elongated structure, but the S/Ns do not permit a clear interpretation. While some of our most distant sources show structure, the most complex sources, NGC 591, NGC 3393, NGC 4388, and UGC 3193, are with $D \lesssim 65$ Mpc all relatively nearby. Each of them contains a compact core, but additional compact sources such as in NGC 591 and NGC 3393 indicate the presence of jets. This also holds for the other two objects, NGC 4388 and UGC 3193, where extended emission in the northeast and/or south has been observed. Nevertheless, most sources only exhibit a core component. This implies that in most of our objects jets are either shorter than a few 100 pc, that they are still below our sensitivity limit due to a steep radio spectrum, or that they do not exist at all.

2.5.2 Spectral indices

Spectral indices can tell us more about the nature of observed radio emission in our sample. For instance, a steep or flat spectral index can be indicative of a jet or radio core, respectively. However, measuring spectral indices for our sources has its own challenges. Using archival data such as NVSS or FIRST, will result in misestimation of spectral indices because of the different beam sizes, which cover different areas (even when we compare the FIRST beam size with our 33 GHz beam size, the ratio of the covered areas is ~450). Additional uncertainty in our spectral index estimation is introduced by the possible variability of the nuclear radio emission. Radio variability in active galaxies is a common phenomenon, especially in compact sources (Mundell et al. 2009), which is the case for most of our targets. The variability is observed on a timescale of a few months to several years, and there are cases where the nuclear flux density has changed by 38% over seven years (Mundell et al. 2009). When we consider that our observations and other observations such as NVSS or FIRST were performed in different years (NVSS observations were conducted 16 years before our observations and FIRST observations from 2 to 19 years before), Seyfert variability is another source of uncertainty in our spectral index calculations.

To exclude such errors, we can calculate the spectral indices over the wide bandwidth of the observations. For our sample, we derived the spectral indices assuming a power-law dependence

for the continuum flux density given by $S \propto \nu^{-\alpha}$, using the 8 GHz (29-37 GHz) bandwidth of our observations. By splitting the data into 4×2 GHz parts and imaging each sub-band separately (with Briggs weighting and a robust parameter of 0), we obtain the spectral indices between 30 GHz and 36 GHz (α_{30}^{36}) using fluxes at the central frequencies of the sub-bands. In some cases the S/N was too low and the source was not detected after splitting the data. It should also be noted that the results obtained by this method have significantly higher errors. We also obtained α_{30}^{36} from spectral index maps created by CASA when using the task CLEAN with the number of Taylor coefficients set as 2. For the sources where 1.4 GHz NVSS flux densities (Condon et al. 1998) or 1.4 GHz FIRST flux densities (Becker et al. 1995) were available (Table 3.3 and 2.4), the indices were also obtained between 1.4 GHz and 33 GHz.

α_{30}^{36} obtained from CASA, based on 21 sources, has an unweighted mean value of 0.68±0.28, while for the splitting method we obtained α_{30}^{36} for 16 sources with an unweighted mean value of 0.79±0.32. For 17 sources the indices were obtained from NVSS and 33 GHz (from now on called $\alpha_{1.4,\,NVSS}^{33}$), with a mean (unweighted) value of 0.97±0.06. For the seven galaxies with measured indices between FIRST and 33 GHz ($\alpha_{1.4,\,FIRST}^{33}$), the unweighted mean value is 0.73±0.16 (errors are the standard error of the mean). See Table 2.4 for spectral index measurement of the individual sources.

2.5.3 Radio continuum versus H_2O disk-maser host galaxy properties

Correlations with optical or near-infrared morphology

As mentioned before, H_2O disk-masers are observed in Seyfert 2s and LINERs (Table 3.3), that is, in spiral galaxies. We adopted the morphological type in de Vaucouleur's scale from the HyperLeda[10] database (Makarov et al. 2014). In this scale, negative numbers represent ellipticals and positive numbers spirals, with higher positive numbers representing later-type spirals. The morphology of the galaxies in our sample lies between S0 and Sc, with the exception of two galaxies that are classified as ellipticals. However, accounting for uncertainties, these could also be S0 galaxies. Fifteen (62%) of our galaxies are barred, and 9 (37%) contain a ring. Figure 2.3 presents 33 GHz continuum and H_2O maser luminosities versus the morphological type. Galaxies with both a bar and a ring in the central parts apparently have lower radio continuum luminosities than those with only a bar. It is well known that in the presence of a bar, gas will be driven inward by angular momentum transport. This transport drives turbulence within the gas that temporarily keeps it strongly gravitationally stable and prevents the onset of rapid star formation. However, at some point, the rotation curve must transition from an approximately flat to an approximately solid body, and the resulting reduction in shear reduces the transport rates and causes gas to build up, eventually producing a gravitationally unstable region, a ring, that is subject to rapid and violent star formation (e.g., Piner et al. 1995; Krumholz & Kruijssen 2015). The region inside the ring might be characterized by a lower rate of inflow, leading to less star formation and synchrotron emission of the ambient gas as well as to a less active nucleus with a lower radio luminosity. We note, however, that our finding is based on small number statistics. Moreover, following the "stuff inside stuff" scenario (Hopkins & Quataert 2010), there may be yet another so far undetected bar inside the ring channeling material closer to the center. Furthermore, not in all our sample galaxies searches for a bar or ring have been performed. Additional morphological studies (see, e.g., Greene et al. 2010; Riffel & Storchi-Bergmann 2011; Greene et al. 2013) would thus be highly desirable.

[10] HyperLeda is a database for physics of galaxies. For more information see: http://leda.univ-lyon1.fr

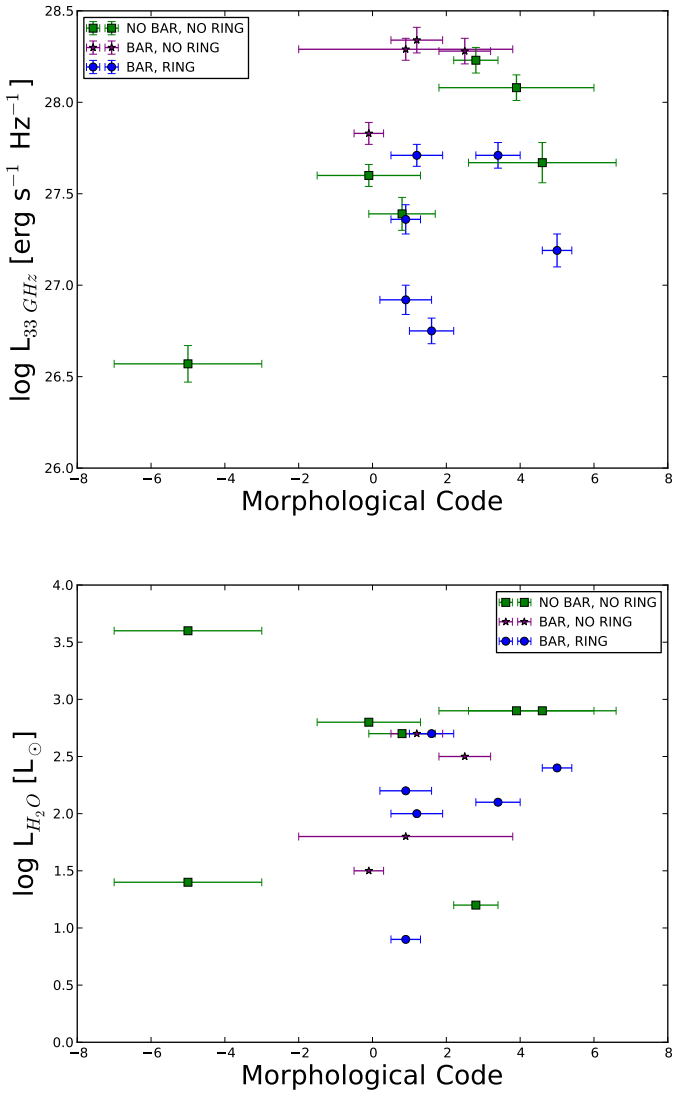

Figure 2.3: Top: 33 GHz radio continuum luminosity versus morphological type. Bottom: H_2O-maser luminosity versus morphological type.

Position angle and inclination

For four galaxies in our sample maser disk inclinations have been reported, with values between 84° and 90° (Kuo et al. 2011). This inclination range for the maser disk should hold for the entire sample. In spiral galaxies, the inclination of the central region is independent of the inclination of the large-scale disk (Ulvestad & Wilson 1984; Nagar & Wilson 1999; Kinney et al. 2000). Apparently, this is also the case for circumnuclear disks and bars at galactocentric distances of several 100 pc (Greene et al. 2014). Although the inclination of the H_2O maser disks of our sample is almost 90°, the large-scale inclination of their host galaxies can reach any value. In Table 2.4 we list P.A. and inclination of the galaxies taken from HyperLeda. The distribution of the inclination is displayed in Fig. 2.4.

We also checked for possible relations between the H_2O maser luminosity and large-scale

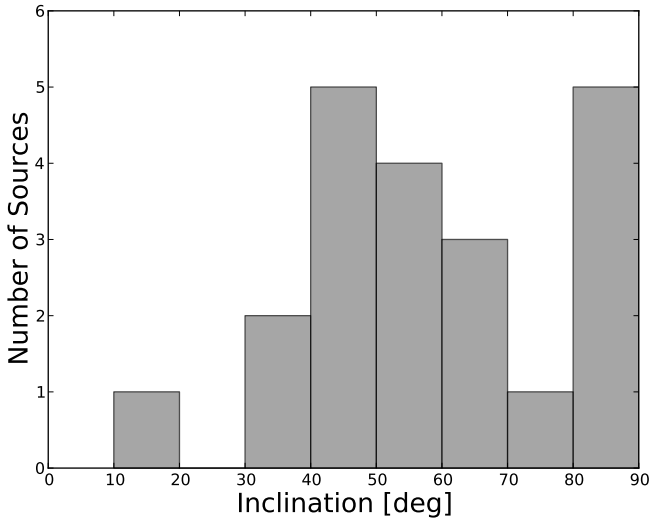

Figure 2.4: Distribution of the inclinations of the galactic large-scale disks.

inclination, and for 33 GHz continuum luminosity and large-scale inclination. As shown in Fig. 2.5, no correlation is found. Of the four galaxies of our sample in which jet-like features can be identified (NGC 591, NGC 3393, NGC 4388, and UGC 3193; see Fig. 2.1), two sources have also reported maser disk orientation from high resolution 22 GHz H_2O line observations. One of them, NGC 3393, was observed by Kondratko et al. (2008). They showed that the maser disk is oriented perpendicular to the kpc-scale radio jet. The other source is NGC 4388, where Kuo et al. (2011) found an edge-on disk with a P.A. (blueshifted side) of 107°. As stated in Sect. 2.4.1, our supposed jet with a P.A. = 24° ± 54° appears to be perpendicular to the maser disk. Inspecting the image shown in Fig. 2.1, the formal error in this position angle, accounting for all the emission seen, may well overestimate the actual uncertainty. The other interesting case is NGC 2273 (see again Sect. 2.4.1 and Fig. 2.1), where an angle not far from 90° is also likely.

Stellar velocity dispersion and circular velocity

The discovery of a correlation between SMBH mass and the velocity dispersion of the bulge component of bright elliptical galaxies, together with similar correlations with bulge luminosity and mass, led to the widespread belief that SMBHs and bulges coevolve by regulating each other's growth (e.g., Kormendy & Ho 2013). However, by studying less luminous spiral galaxies and making use of the quite accurately determined SMBH masses of H_2O megamaser galaxies, it has become clear more recently that the relationship between $M_{\rm SMBH}$ and velocity dispersion has a larger scatter and more structure than was originally thought (Greene et al. 2010; Sun et al. 2013; Greene et al. 2016). In particular, it seems (although still based on small number statistics) that the megamaser galaxies may show a different scaling relation than galaxies of similar size and Hubble type studied at other wavelengths, possibly indicating an observational bias in either the masing or the non-masing galaxy samples. It is thus essential to look deeper into this apparent scatter to shed more light onto the underlying physics that probably involves inflow, black hole growth, and subsequent feedback.

We searched for possible relations between the 33 GHz luminosity, the stellar velocity

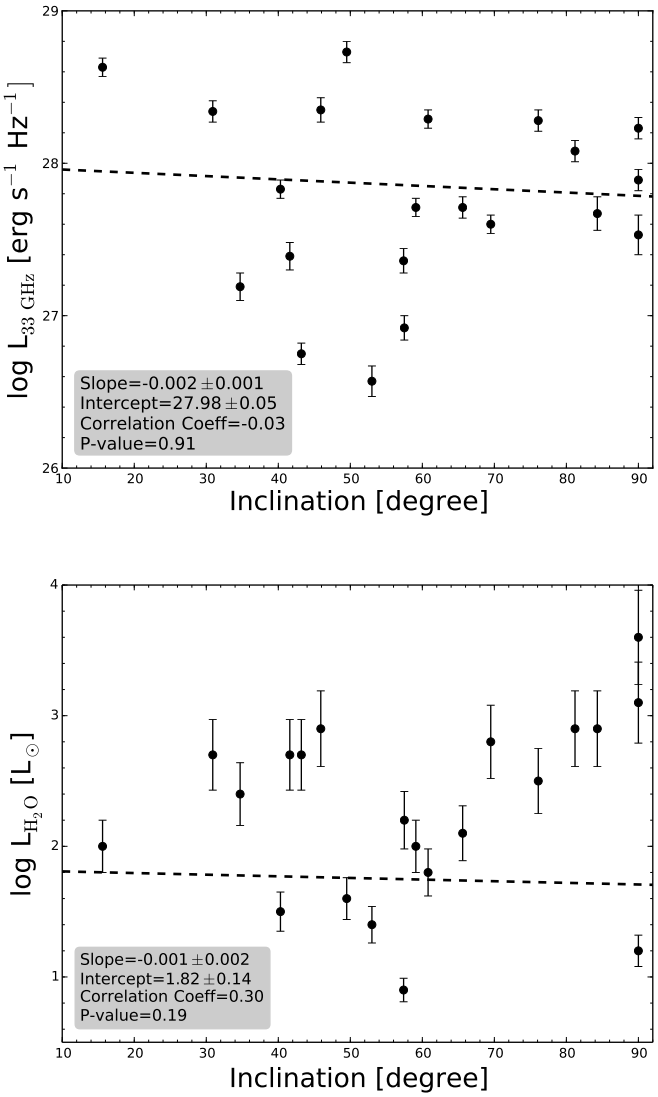

Figure 2.5: Top: 33 GHz continuum luminosity versus large-scale inclination. Bottom: H_2O-maser luminosity versus large-scale inclination of the galaxies. The dashed lines show linear fits to the data points. The slope and intercept of the fits, the correlation coefficient, and the *P*-value of the Spearman test, indicating the likelihood that the two quantities are unrelated, are indicated in a corner of each panel.

dispersion σ_* , and the maximum rotation velocity of the gas, V_{rot}. As shown in the bottom panel of Fig. 2.6, σ_* and 33 GHz continuum luminosity are not correlated. Surprisingly, however, we find an anticorrelation between the 33 GHz continuum luminosity and circular velocity of the galaxies, with a correlation coefficient of –0.70 and an associated *P*-value of 0.0056. For a better understanding of the implications, we note that the HyperLeda rotation velocities are obtained from HI 21 cm line data and corrected for the inclination of the main body of the respective galaxy. In spiral galaxies, HI is most prominent outside the cerntral region, so that here we compare a central parameter with a parameter obtained from emission originating outside of the central region. How can these be related? And why do we find

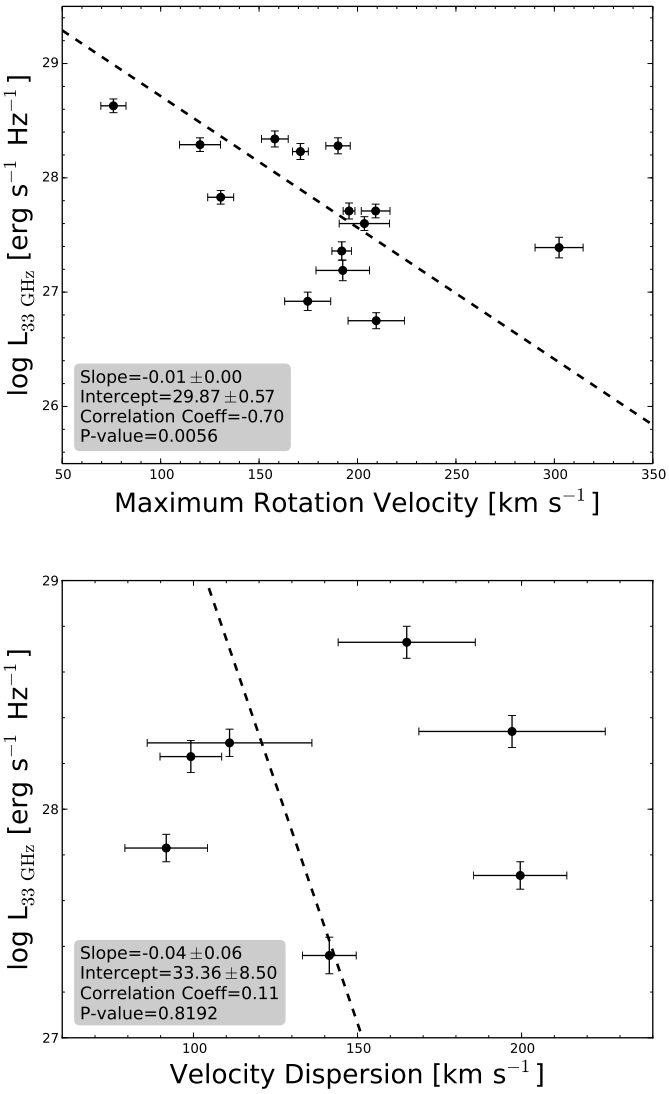

Figure 2.6: Top: Radio continuum versus circular velocity (from HyperLeda). Bottom: Radio continuum versus central stellar velocity dispersion. "Central" refers to standardized aperture r_{norm} of 0.595 h^{-1}kpc, which is equivalent to an angular diameter of 3.4 arcsec at the distance of the Coma cluster. The lines show linear fits to the data points accounting for errors along both axes. The slope and intercept of the fit, the correlation coefficient, and the *P*-value of the Spearman test (see also Fig. 2.5) are shown in a corner of each plot.

an anticorrelation? The rotation velocity of spirals tends to reach near-maximum values at $r \lesssim 2$ kpc (e.g., Hlavacek-Larrondo et al. 2011; Chemin et al. 2015), while our images typically cover 1 kpc with most of the detected emission arising from an even smaller region.

Following Safronov (1960), Toomre (1964) and Quirk (1972), for a gaseous differentially rotating disk, the following criterion must hold:

$$Q = \frac{\sigma_{\rm gas}\ \kappa}{\pi\ {\rm G}\ \Sigma_{\rm gas}} > 1,$$

with $\sigma_{\rm gas}$ denoting the velocity dispersion, κ the epicyclic frequency, and G the gravitational constant. $\Sigma_{\rm gas}$ stands for surface density. Thus, a higher rotational velocity keeps the disk more stable and less prone to fragmentation and subsequent star formation, reducing radio continuum emission that is due to star formation. More regular motion may also reduce accretion by the AGN and the luminosity of the radio core. Nevertheless, this may be a far-fetched explanation. Although the correlation is statistically convincing, we find the result surprising, and confirmation is needed by measurements of more such galaxies by employing both lower and higher angular resolution to fully cover the relevant linear scales.

Infrared versus radio luminosity

As pointed out by Diamond-Stanic et al. (2009), the radio luminosity can be an indicator of the AGN isotropic luminosity. On the other hand, in Seyfert 2 galaxies, the UV/optical photons of the AGN are absorbed by the circumnuclear dusty torus and are re-emitted in the mid-IR. Therefore the mid-IR photometry can also be used as an indicator of the AGN activity (e.g., Stern et al. 2012; Fiore et al. 2008; Georgantopoulos et al. 2008). Hence we investigate the radio to mid-infrared correlation of our disk-maser sample, since both bands can be indicators of the total AGN power. As shown in Fig. 2.7, a weak correlation with correlation coefficient of 0.30 is observed.

2.5.4 Radio continuum, X-ray, and IR luminosities versus maser-disk properties

H_2O maser luminosity

Since the AGN luminosity is most likely the power source for H_2O megamasers (Lo 2005), we expect correlations between AGN luminosity and H_2O maser luminosity. For example, Henkel et al. (2005) reported a correlation between far-infrared (FIR) and H_2O maser flux densities for maser sources that are related to either star-forming regions or AGNs. We also observe a weak correlation between IR and H_2O maser luminosity with a correlation coefficient of 0.63. Henkel et al. (2005) proposed that for the case of maser emission associated with AGN, the observed correlation between IR and H_2O maser luminosity can be related to the existence of spatially extended dust-rich bars that fuel the central engine. Our observed weak positive correlation between the mass of the central engine and the H_2O maser luminosity (see Sect. 2.5.4) may support the suggestions of Henkel et al. (2005). However, we do not detect such a relation between H_2O maser and radio (33 GHz and 1.4 GHz) luminosities, or between H_2O-maser and hard X-ray luminosities (see Fig. 2.8).

Van den Bosch et al. (2016) reported a weak correlation between maser and [OIII] luminosities from studying all maser sources, while this correlation vanishes when only the disk masers are considered. Kondratko et al. (2006b) also reported a possible correlation between soft X-ray (2-10 KeV) and maser luminosities, where again most of the correlation is due to the

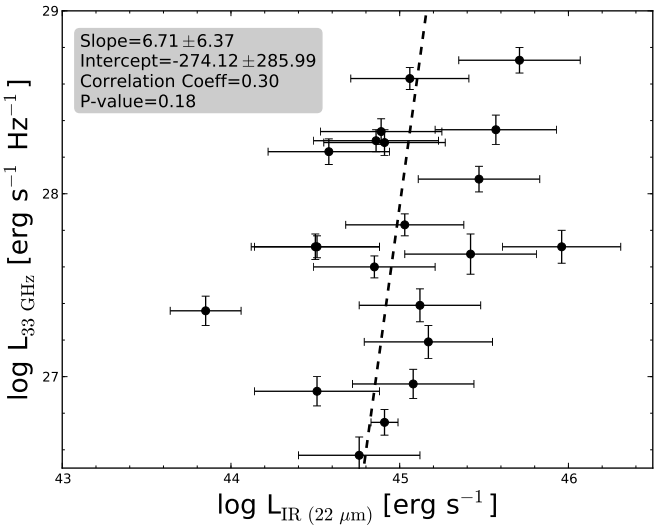

Figure 2.7: Radio luminosity versus infrared luminosity (WISE 22 μm). The line shows a linear fit to the data points accounting for errors along both axes. For the inset in the upper left corner, see the caption to Fig. 2.5.

non-disk masers. More investigations to determine possible correlations between soft X-ray (2-10 KeV) and H_2O maser luminosity for a sample of 14 disk-maser galaxies were carried out by Castangia et al. (2013). They did not find any correlation either. Following Van den Bosch et al. (2016), the disk-maser galaxies, even though they cover a range of two orders of magnitude in isotropic maser luminosity, may be quite similar with respect to galaxy and SMBH mass. Their properties do not provide a sufficiently broad range of parameters, given the constant surface density predicted by Neufeld et al. (1994) and the similar sizes (~0.5 pc) for most of the masing disks. The reason that we do not see correlations between H_2O maser and hard X-ray or radio luminosities might be that the small differences in the disk inclination angle and/or different support through seed photons from the nuclear continuum (which are probably responsible for the strong systemic maser features in NGC 4258 (Herrnstein et al. 1998)) may lead to significant scatter that efficiently hides any expected correlation.

Maser-disk radius

An empirical upper envelope for a scaling relation between $M_{\rm SMBH}$ and the outer radii of the megamaser disks, $r_{\rm max} = 0.3 \times M_{\rm SMBH}/10^7$ M$_\odot$, was reported by Wardle & Yusef-Zadeh (2012) for 12 disk maser sources. We have searched for additional relations associated with disk radii (see Table 2.4), addressing a connection to radio, IR, and X-ray luminosity. Recently, Masini et al. (2016) have searched for correlations between the ratio of inner and outer radii and X-ray luminosity in the 2-10 keV band for 14 disk-maser sources. They did not find any clear correlation.

Although it is more plausible to see correlations at high radio frequencies (where mainly the core that is directly related to the AGN may be seen) than at low frequencies (where the possible presence of jets with steep spectra might cause the emission to be less correlated with the maser disk size), we do not find a large difference (see Fig. 2.9). The strongest correlations apparently belong to the radio luminosities versus the disk inner radius (correlation coefficients of 0.87

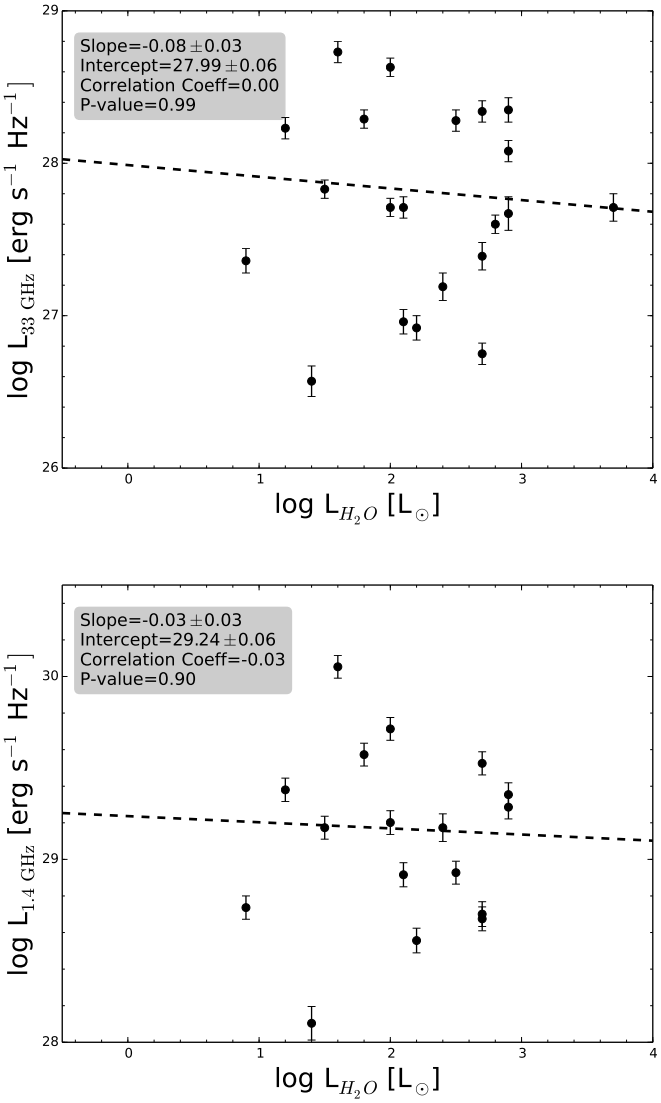

Figure 2.8: **Top:** 33 GHz continuum luminosity versus H_2O maser luminosity. **Bottom:** 1.4 GHz continuum luminosity versus H_2O maser luminosity. The H_2O maser luminosity (isotropic emision assumed) is on a logarithmic scale, in units of $L_\odot$. The lines show linear fits to the data points. The slope and intercept of the fit, as well as the correlation coefficient and the *P*-value of the Spearman test are shown in the upper left corner of each plot.

and 0.73 for 1.4 GHz and 33 GHz, respectively) and disk outer radius (correlation coefficients of 0.40 and 0.54 for 1.4 GHz and 33 GHz, respectively). Generally, as seen in Fig. 2.9, the disk inner radii show stronger correlations with luminosity than the disk outer radii.

This may suggest that the core has a greater influence at the inner than at the outer radii, where disk warping, star formation, or peculiar density distributions may reduce the direct impact of the SMBH. However, Gao et al. (2017) found a correlation between maser disk outer radius (and not the inner radius) and WISE IR luminosity at Band 3 (λ=12 μm), with a Spearman rank correlation coefficient of 0.83.

Within this context, it should be noted that our radio luminosities trace the 100 pc scale, so

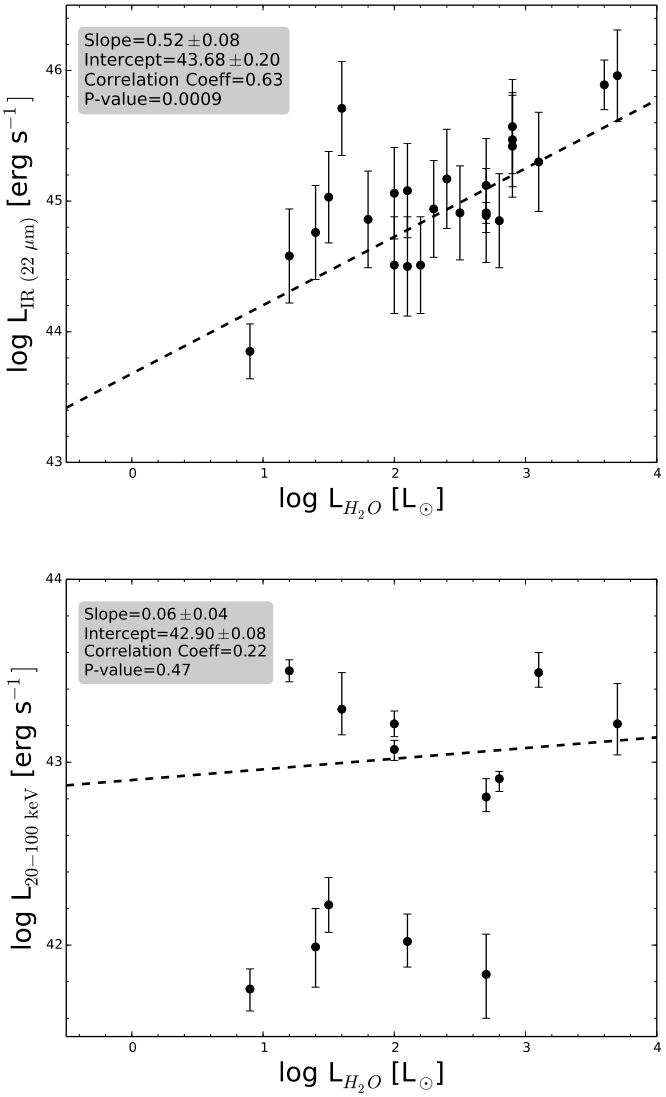

Figure 2.8: *(cont.)* ***Top:*** *IR luminosity versus H_2O maser luminosity.* ***Bottom:*** *Hard X-ray luminosity versus H_2O maser luminosity.*

that any relation with properties of sub-pc maser disks requires follow-up investigations with higher resolution.

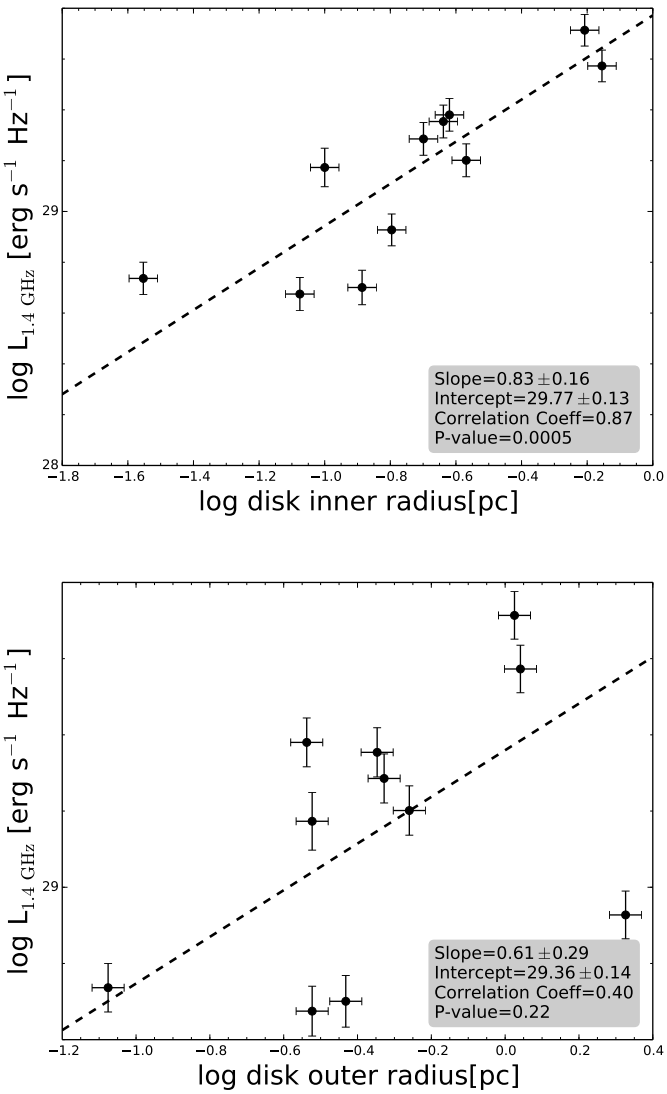

Figure 2.9: Maser disk inner **(top)** and outer radius **(bottom)** versus 1.4 GHz continuum luminosity. The inner and outer radii are taken from from Kuo et al. (2011), Braatz et al. (2015a), and Gao et al. (2017). The black dashed lines are linear fits to the data. The slope and intercept of the fit, as well as the correlation coefficient and the *P*-value of the Spearman test (see also Fig. 2.5) are shown in a corner of each plot.

Black hole masses

As mentioned in Sect. 2.5.3, relations between $M_{\rm SMBH}$ and other properties of galaxies have extensively been studied in recent decades (e.g., Kormendy & Ho 2013). Accurate measures of the black hole masses are essential to study such relations.

In nearby galaxies, VLBI observations of masers with high angular resolution provide a

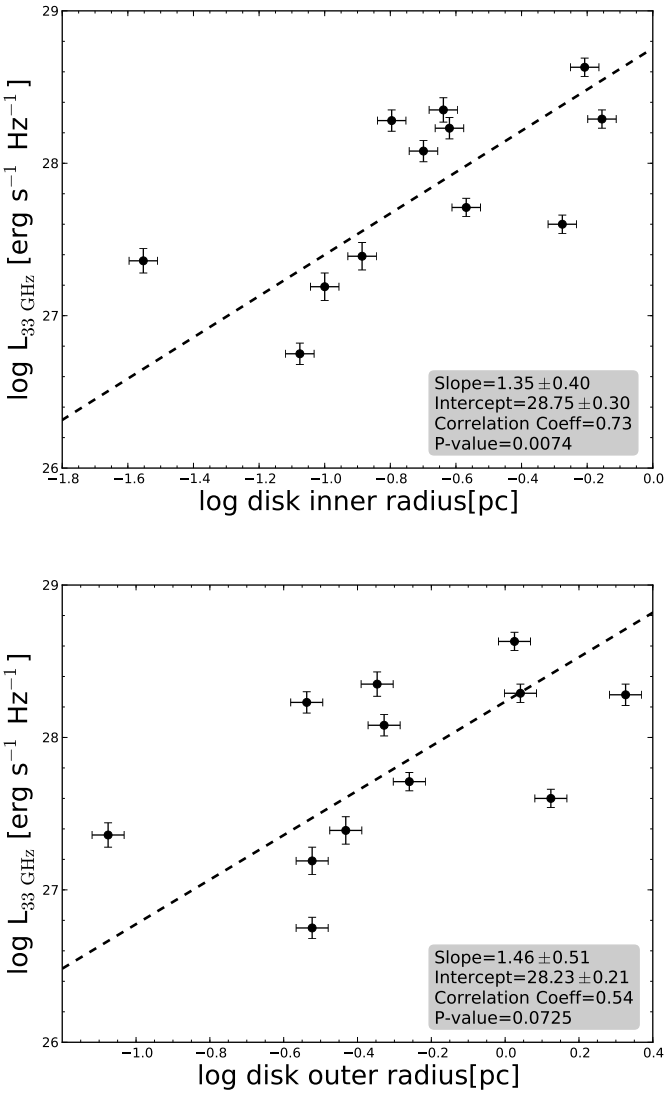

Figure 2.9: *(cont.)* Maser disk inner **(top)** and outer radius **(bottom)** versus 33 GHz continuum luminosity.

direct and precise measurement of the $M_{\rm SMBH}$ (see Miyoshi et al. 1995; Herrnstein et al. 1999; Humphreys et al. 2013). The MCP has provided precise measures of the $M_{\rm SMBH}$ for 13 galaxies (Kuo et al. 2011; Braatz et al. 2015a; Gao et al. 2017). In Fig. 2.10 we present $M_{\rm SMBH}$ versus the continuum luminosity for these galaxies. The strongest correlation is seen for H_2O maser luminosity versus $M_{\rm SMBH}$ with a correlation coefficient of 0.33. For continuum luminosities, no significant correlation is observed. We should nevertheless keep in mind that a sample of 13 galaxies is small for statistical considerations.

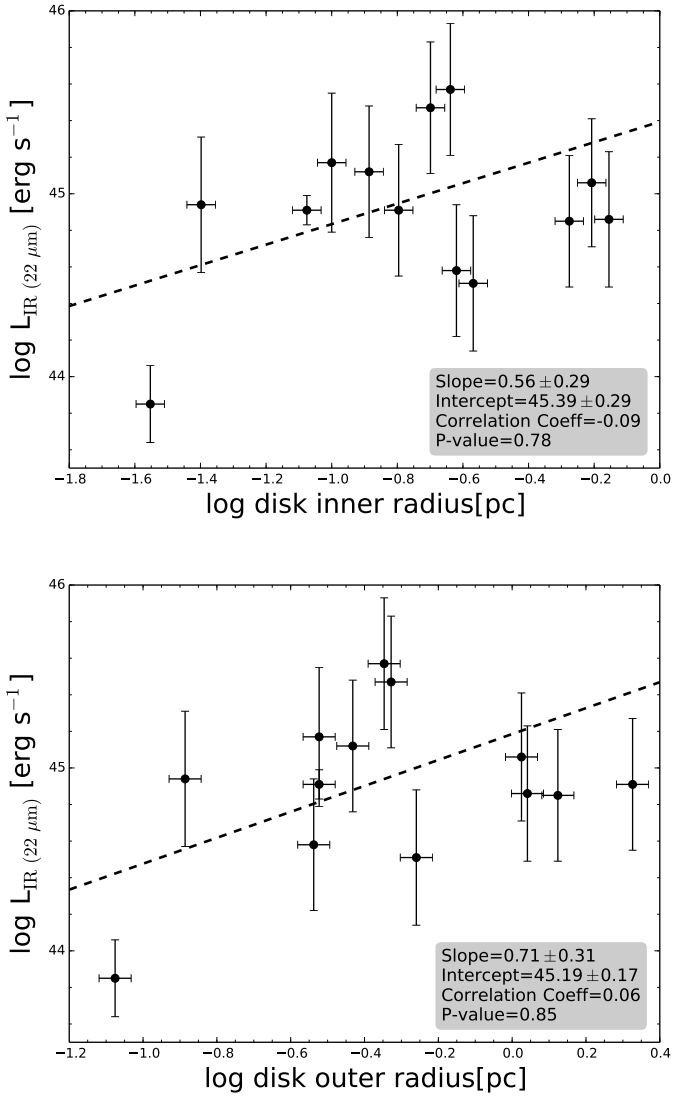

Figure 2.9: *(cont.)* Maser disk inner **(top)** and outer radius **(bottom)** versus IR luminosity, deduced from WISE 22 μm data.

2.6 Summary

VLA observations of 24 mostly Seyfert 2 galaxies with edge-on H_2O megamaser disks were obtained at Ka band (29–37 GHz) to investigate the radio continuum emission from the center of these galaxies with ~0.2-0.5 arcsec resolution. With respect to the distance distribution of the sample galaxies, this corresponds to a linear resolution on the order of 100 pc. Out of 24 galaxies, 21 show radio emission at a 4.5 σ or higher level, giving a detection rate of 87%. Almost all of the galaxies contain compact cores with beam-convolved (and deconvolved) major axes smaller than 2.5 times the beam major axis, which even holds for most of the sources with more complex structure. NGC 591 exhibits two main components, and NGC 3393 even three main components, which is indicative of >100 pc scale radio jets. Four additional galaxies have extended structure, possibly also revealing jet-like features, but the majority shows a single

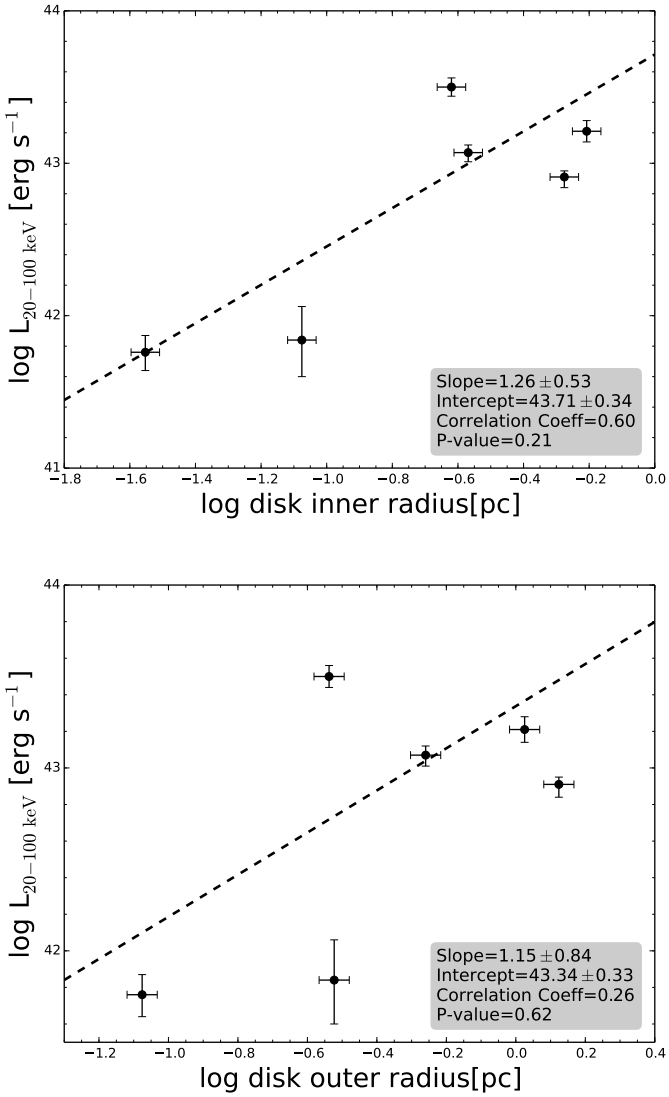

Figure 2.9: *(cont.)* Maser disk inner **(top)** and outer radius **(bottom)** versus hard X-ray luminosity.

compact emission region.

The radio continuum luminosity at 1.4 GHz, 22 GHz H_2O maser luminosity, infrared luminosity (22 μm), the hard X-ray luminosity (20-100 keV), optical or near-infrared morphology, position angle and inclination of the host galaxies, and their stellar velocity dispersions and circular velocities, maser-disk radii and black hole masses were taken into account for the further analysis of disk-maser host galaxy properties, as summarized below.

Beside NGC 3393 that the perpendicular orientation of its maser disk and its kpc-scale jet is already reported by Kondratko et al. (2008), we find that the relative orientation of the maser disk and a jet-like 33 GHz continuum feature in NGC 4388 appears to be orthogonal. NGC 2273 may show a similar scenario, but here alignments are less certain. Galaxies with inner rings appear to exhibit less 33 GHz emission than those without. The maximum rotation velocity of the disk-maser host galaxies appears to be anticorrelated with 33 GHz radio continuum luminosities,

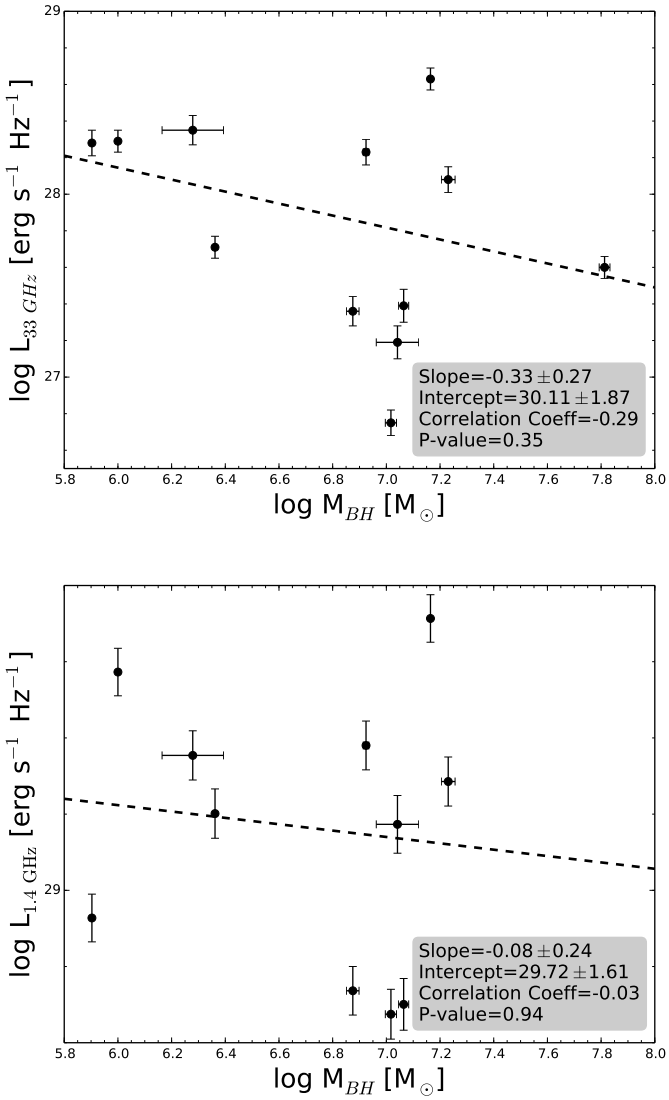

Figure 2.10: **Top:** 33 GHz continuum luminosity versus black hole mass. **Bottom:** 1.4 GHz luminosity versus black hole mass. Black hole masses are given on a logarithmic scale in units of solar mass, taken from Kuo et al. (2011), Braatz et al. (2015a), and Gao et al. (2017). The lines show linear fits to the data. The slope and intercept of the fit, as well as the correlation coefficient and the *P*-value of the Spearman test (see also Fig. 2.5) are shown in a lower corner of each panel.

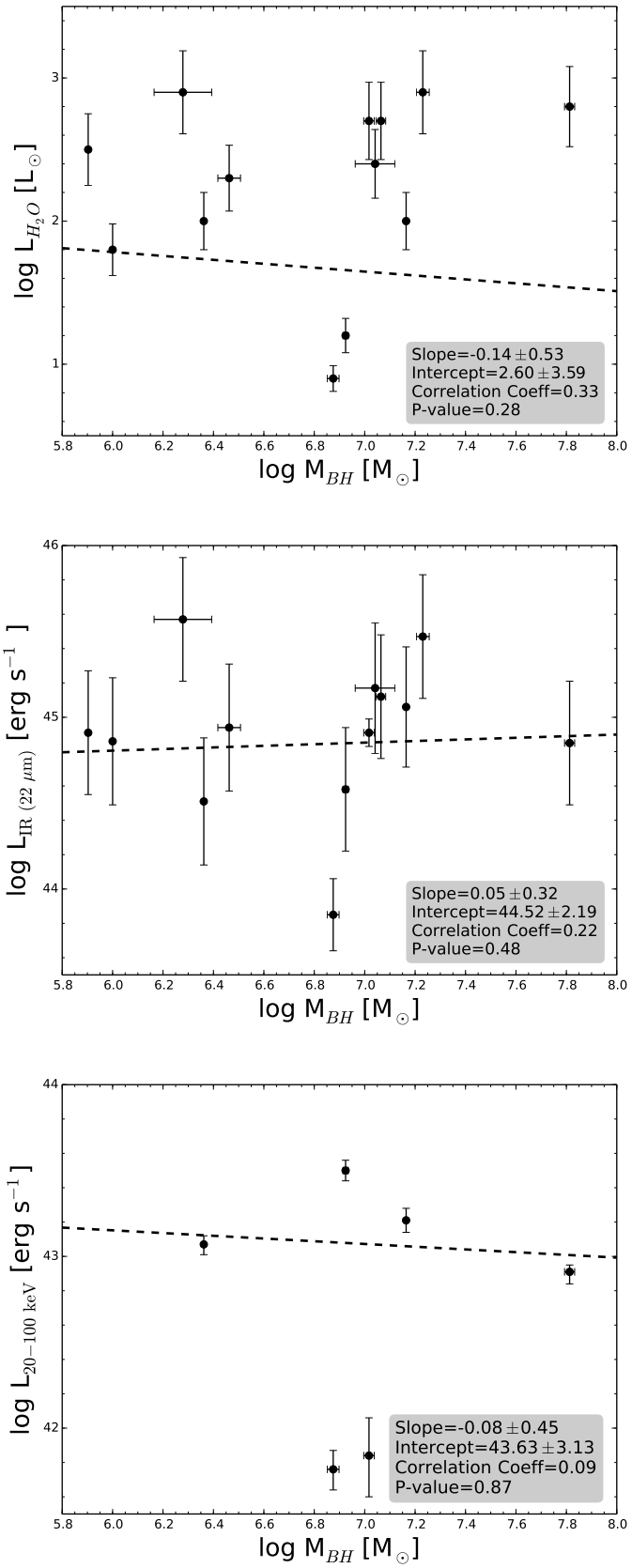

Figure 2.10: **Top:** H_2O-maser luminosity versus black hole mass. **Middle:** IR luminosity (WISE 22 μm data) versus black hole mass. **Bottom:** Hard X-ray luminosity versus black hole mass.

with a Spearman rank correlation coefficient of –0.70. The 33 GHz radio continuum shows a weak correlation with IR luminosity at 22 μm derived from the WISE satellite. The H_2O maser luminosity does not exhibit any correlations with the radio (1.4 GHz and 33 GHz) or hard X-ray luminosities. The black hole masses show stronger correlations with the H_2O maser luminosity than with the 1.4 GHz, 33 GHz, or hard X-ray luminosities. The H_2O maser-disk inner radii show stronger correlations with 1.4 GHz, 33 GHz, and hard X-ray luminosities than the disk outer radii. The strongest correlation is found with low-frequency 1.4 GHz radio data.

Further studies with higher spatial resolution would be highly desirable to reveal the nature of the detected 33 GHz continuum sources, to identify and map jets on scales å@*centerstack*<∼100 pc, and to better distinguish between radio emission arising from the AGN and that from surrounding star-forming regions.

Acknowledgments

F.K. would like to thank Sergio Dzib Quijano for his useful comments on the data reduction process. This work made use of the NASA/IPAC extragalactic Database (NED), which is operated by the Jet Propulsion Laboratory, California Institute of Technology, under contract with NASA. We further acknowledge the usage of the HyperLeda database (http://leda.univ-lyon1.fr) and the SAO/NASA ADS Astronomy Abstract Service (http://adsabs.harvard.edu) and Kapteyn Package (Terlouw & Vogelaar 2015).

Table 2.3: H_2O maser positions versus our 33 GHz positions.

Galaxy	Maser				33GHz				Difference		Maser
	*J*2000 R.A.	δR.A. ($''$)	*J*2000 Dec.	δDec. ($''$)	*J*2000 R.A.	δR.A. ($''$)	*J*2000 Dec.	δDec. ($''$)	ΔR.A. ($''$)	ΔDec. ($''$)	Position Reference
ESO558-G009	07:04:21.0113	0.014	–21:35:18.948	0.014	07:04:21.01	0.06	–21:35:19.03	0.05	0.02	0.08	1
IC 2560	10:16:18.710	0.075	–33:33:49.74	0.01	10:16:18.71	0.16	–33:33:49.60	0.16	0.00	0.14	2
Mrk 1029	02:17:03.566	0.5	+05:17:31.43	0.5	02:17:03.57	0.18	+05:17:31.15	0.18	0.06	0.28	1
Mrk 1419	09:40:36.38370	0.01	+03:34:37.2915	0.01	09:40:36.38	0.14	+03:34:37.36	0.13	0.06	0.07	3
NGC 1194	03:03:49.10864	0.0002	–01:06:13.4743	0.0004	03:03:49.11	0.03	–01:06:13.48	0.03	0.02	0.01	3
NGC 2273	06:50:08.65620	0.01	+60:50:44.8979	0.01	06:50:08.69	0.28	+60:50:45.10	0.27	0.25	0.20	3
NGC 3393	10:48:23.4659	0.001	–25:09:43.477	0.001	10:48:23.46	0.03	–25:09:43.44	0.03	0.08	0.04	4
NGC 4388	12:25:46.77914	0.0004	+12:39:43.7516	0.0003	12:25:46.78	0.02	+12:39:43.77	0.02	0.01	0.02	3
NGC 5495	14:12:23.35	0.3	–27:06:29.20	0.3	14:12:23.35	0.05	–27:06:29.14	0.06	0.00	0.06	5
UGC 3789	07:19:30.9490	0.01	+59:21:18.3150	0.01	07:19:30.95	0.08	+59:21:18.37	0.08	0.01	0.06	3

Notes. Column 1: source name. Columns 2 and 3: *J*2000 right ascension determined from H_2O maser observations and their uncertainties. Columns 4 and 5: *J*2000 declination determined from H_2O maser observations and their uncertainties. Columns 6 and 7: *J*2000 right ascension determined from our radio maps and their uncertainties. Columns 8 and 9: *J*2000 declination determined from our radio maps and their uncertainties. Columns 10 and 11: right ascension and declination difference between H_2O maser observations and our observations. Column 12: references for H_2O maser observations: (1) Gao et al. (2017); (2) Ishihara et al. (2001); (3) Kuo et al. (2011); (4) Kondratko et al. (2008) and (5) Kondratko et al. (2006a).

Table 2.4: Position angle and inclination of the host galaxies, the spectral indices, and the disk maser properties.

Galaxy	Spectral indices				Galaxy scale		This work	Maser disk					
	$\alpha^{33}_{1.4\,NVSS}$	$\alpha^{33}_{1.4\,FIRST}$	α^{36}_{30}	α^{36}_{30}	P.A. (°)	Inclination (°)	P.A. (°)	P.A. (°)	Inclination (°)	$R_{\rm in}$ (pc)	$R_{\rm out}$ (pc)	$M_{\rm SMBH}$ ($10^7 M_\odot$)	ref
ESO558-G009	0.88 ± 0.02	...	1.11±0.94	0.76±0.22	8.0	81.2	155±33	256	98	0.20	0.47	1.7	1
IC 0485	...	...	...	...	153.9	90.0	...	...	...	...	...	...	...
IC 2560	0.88± 0.02	...	1.31±0.88	0.88±0.21	45.7	65.6	25±11	...	...	...	...	...	...
J0126-0417	...	...	-2.06±2.58	0.87±2.34	100.0	...	146±86	...	...	...	...	...	...
J0350-0127	...	...	...	-2.63±4.32	155.0	...	134.6±8.1	...	...	...	...	...	...
J0437+2456	...	...	...	...	...	...	...	20	81	0.04	0.13	0.29	1
J0437+6637	1.12 ± 0.08	...	...	-0.52±1.58	117.0	53.0	...	...	...	...	...	...	...
J0836+3327	...	...	...	...	51.6	57.7	...	...	...	...	...	...	...
J1658+3923	...	0.95±0.07	...	2.36±2.77	104.3	90.0	81.4±4.7	...	...	...	...	...	...
Mrk 0001	0.93 ± 0.01	...	1.06±0.30	0.93±0.06	77.5	60.8	119.6±2.1	...	...	0.70	1.10	1.0	2
Mrk 0078	0.96 ± 0.02	...	0.82±0.58	1.01±0.17	87.0	49.5	81±10	...	...	...	...	...	...
Mrk 1029	0.73 ± 0.04	0.61±0.04	...	0.72±2.37	73.5	45.9	59±11	218	79	0.23	0.45	0.19	1
Mrk 1210	0.79 ± 0.01	...	0.03±0.08	-0.12±0.93	160.0	15.6	179±83	...	...	0.62	1.06	14.6	2
Mrk 1419	0.96 ± 0.06	0.84±0.05	3.0 ±2.72	-0.67±1.92	40.2	41.5	117±84	229	89	0.13	0.37	1.16	3
NGC 0591	0.98 ± 0.02	...	2.47±1.49	1.31±1.60	0.2	40.3	153.3±2.8	...	...	...	...	...	...
NGC 1194	...	0.10±0.03	-0.20±0.63	-0.25±0.27	139.3	71.1	75±82	157	85	0.54	1.33	6.5	3
NGC 2273	1.00 ± 0.04	...	0.55±1.13	1.86±1.15	63.3	57.4	82.8±2.8	153	84	0.028	0.084	0.75	3
NGC 2979	1.19 ± 0.04	...	0.91±1.94	0.65±0.92	21.0	57.5	138±51	...	...	...	...	...	...
NGC 3393	0.87 ± 0.03	...	1.02±0.26	2.10±3.18	12.8	30.9	165±50	...	...	...	...	...	...
NGC 4388	0.84 ± 0.02	0.52± 0.02	-0.10±0.22	3.36±3.58	91.1	90.0	24±54	107	...	0.24	0.29	0.84	3
NGC 5495	1.44 ± 0.06	...	...	0.43±1.38	44.5	34.7	167±24	176	95	0.10	0.30	1.1	1
NGC 5728	1.09 ± 0.02	...	-1.26±0.37	-1.53±0.17	14.5	59.1	...	...	...	0.27	0.55	2.3	2
UGC 3193	0.47 ± 0.02	...	2.08±1.12	0.96±1.92	177.4	76.1	167.2±4	...	...	0.16	2.12	0.8	2
UGC 3789	1.40 ± 0.04	1.34±0.03	1.89±4.26	2.83±1.76	166.0	43.2	117±22	41	>88	0.084	0.30	1.04	3

Notes. Column 1: source name. Column 2: spectral indices between NVSS 1.4 GHz and 33 GHz, with uncertainties. Column 3: spectral indices between FIRST 1.4 GHz and 33 GHz, with uncertainties. Columns 4 and 5: spectral indices between 30 GHz and 36 GHz from our 8 GHz bandwidth observations, first by splitting the data and second by setting the Taylor coefficients as two in CASA (see Sect. 2.5.2). Column 6 and 7: large scale position angle and inclination (from HyperLeda database). Column 8: position angle of the 33 GHz continuum component with formal errors, obtained from Gaussian fits to a region containing all the significant emission. Columns 9 and 10: maser disk position angle and inclination. Columns 11 and 12: maser disk inner and outer radii in pc. Column 13: black hole mass. Column 14: references for disk maser radii and $M_{\rm SMBH}$: (1) Gao et al. (2017); (2) Braatz et al. (2015b); (3) Kuo et al. (2011).

CHAPTER 3

Accretion disk versus jet orientation in H_2O megamaser galaxies

The content of this chapter, with the same title, was published as an article in the Astronomy & Astrophysics journal.
Credit: ***F. Kamali et al., A&A, 624, A42, 2019, reproduced with permission ©ESO.***

Abstract

Context. An essential part of the paradigm describing active galactic nuclei is the alignment between the radio jet and the associated rotation axis of the sub-pc accretion disks. Because of the small linear and angular scales involved, this alignment has not yet been checked in a sufficient number of low luminosity active galactic nuclei (LLAGNs).
Aims. The project examines the validity of this paradigm by measuring the radio continuum on the same physical scale as the accretion disks to investigate any possible connection between these disks and the radio continuum.
Methods. We observed a sample of 18 LLAGNs in the 4.8 GHz (6 cm) radio continuum using the Very Long Baseline Array (VLBA) with 3.3 to 6.5 milliarcsecond resolution. The sources were selected to show both an edge-on accretion disk revealed by 22 GHz H_2O megamaser emission and signatures of a radio jet. Furthermore, the sources were previously detected in 33 GHz radio continuum observations made with the Very Large Array.
Results. Five out of 18 galaxies observed were detected at $8\,\sigma$ or higher levels (Mrk 0001, Mrk 1210, Mrk 1419, NGC 2273, and UGC 3193). While these five sources are known to have maser disks, four of them exhibit a maser disk with known orientation. For all four of these sources, the radio continuum is misaligned relative to the rotation axis of the maser disk, but with a 99.1% confidence level, the orientations are not random and are confined to a cone within 32° of the maser disk's normal. Among the four sources the misalignment of the radio continuum with respect to the normal vector to the maser disk is smaller when the inner radius of the maser disk is larger. Furthermore, a correlation is observed between the 5 GHz VLBA radio continuum and the [OIII] luminosity and also with the H_2O maser disk's inner radius.

key words. Galaxies: active – Galaxies: ISM – Galaxies: jets – Galaxies: nuclei - Galaxies: Seyfert – Radio continuum: galaxies

3.1 Introduction

Accretion of material onto the central engine of an active galactic nucleus (AGN) is often accompanied by ejection of material, either in the form of outflows or collimated jets. Conservation of angular momentum implies that the distribution of any material ejected from the accretion disk surrounding the supermassive black hole (SMBH) should be perpendicular to the disk unless an external torque is present. On the other hand, studies have shown that the jet direction and the rotation axis of the large-scale galactic disk are not necessarily aligned (e.g., Pringle et al. 1999; Nagar & Wilson 1999). Further studies have been carried out to investigate the alignment of the jet axis with the vector perpendicular to the smaller 20-150 pc scale disks such as dust disks in active galaxies, and have reported that the jets are not always perpendicular to these disks (Schmitt et al. 2002). This misalignment indicates that gas on different scales has different angular momentum orientations. Whether this is a result of past mergers or warping of the accretion disk, or a general physical condition required for accretion, is still a matter of debate (see Greene et al. 2010, and references therein). With the discovery of H_2O maser emission from the water vapor $J_{K_-K_+}$=6_{16}-5_{23} rotational transition in the sub-pc disk surrounding the SMBH in NGC 4258 (e.g., Nakai et al. 1993; Greenhill et al. 1995; Miyoshi et al. 1995; Herrnstein et al. 1999), an opportunity arose to observe the accretion disk of AGNs with the extremely high angular resolution only offered by Very Long Baseline Interferometry (VLBI) observations. The other unique feature of galaxies with H_2O masers in their nuclear accretion disk is that these accretion disks are viewed within a few degrees edge-on, otherwise linear scales for coherent amplification would be too short, and thus we expect the putative jets to be on the plane of the sky and free of viewing angle biases. Therefore, the nuclear region of galaxies hosting maser disks are good laboratories for studying the alignment between the jet and the normal to the pc-size disks. Greene et al. (2013) and Pjanka et al. (2017) investigated this alignment by observing the radio continuum jets on >50 pc scales. They also observed the structures such as galaxy-scale disks, bars, and spiral arms on <5 kpc scales and compared the alignment of these structures with the smaller scale sub-pc maser disks. They reported that the orientation of the 100 pc scale disks and galaxy scale disks are distributed randomly with respect to the orientation of the maser disks. However, the radio continuum jets (observed on tens of pc to kpc scale) are found to align within $< 15^{\circ}$ of the maser disk's rotation axis (Greene et al. 2013). With the purpose of investigating the jet-disk alignment on smaller scales (~ 2 pc) and also of providing a larger sample compared to that already existing in the literature, in this work we attempt to study the alignment of the jet and the rotation axis of the accretion disk in low luminosity active galactic nuclei (LLAGN) with H_2O megamaser disks seen approximately edge-on. Recently we have observed a sample of 24 such galaxies with a resolution of $0.''2$ – $0.''5$ using the Karl G. Jansky Very Large Array (VLA) at 33 GHz in a pilot project (Kamali et al. 2017). Radio synchrotron emission was detected on kpc scales in 21 of these galaxies. In the follow-up observations presented here, we look for radio emission on scales of <50 pc (~5 mas or ~2 pc resolution at a fiducial distance of 90 Mpc) using the Very Long Baseline Array (VLBA). We chose C band because the synchrotron emission is supposedly brighter at this lower frequency compared to the previous VLA Ka-band observations. Our goal is to measure the radio continuum and investigate the relation between the jet axis and the maser disk orientation. This paper is organized in the following way: In Sect. 3.2 we present our sample. In Sect. 3.3 we present the observations and data reduction process. The description of the observational results is presented in Sect. 3.4, followed by analysis and subsequent discussions in Sect. 3.5. A summary is given in Sect. 3.6.

3.2 Sample

We selected a sample of 18 LLAGNs with declinations greater than -5°, including 14 sources from our 33 GHz survey (Kamali et al. 2017) plus four more from the Megamaser Cosmology Project (MCP, e.g., Reid et al. 2009, 2013; Braatz et al. 2010; Greene et al. 2010; Kuo et al. 2011, 2013; Pesce et al. 2015; Gao et al. 2017). These sources have signatures of megamasers disks, i.e., they show three groups of H_2O megamaser emissions in their spectrum; one set of maser features has velocities grouped around the recession velocity of the galaxy, and those of the two other sets of maser features are offset from this recession velocity, representing the approaching and receding sides of the disk. In our selected sample, 12 sources are considered "clean disks," where the maser emission from the disk dominates over any other maser emission from the jets or outflows (Pesce et al. 2015). These sources are shown in boldface in all tables. The maser emission in six other sources of our sample may not arise from the disk, but rather from the nuclear outflows or star forming regions in these galaxies. Detections for three out of these six non-clean disks are reported in this work. The maser distributions in two of these three galaxies (Mrk 0001 and Mrk 1210) have been mapped using the VLBI and the consequent fitting of disk models does not rule out a disk maser scenario (see Sect. 3.4.1 for further details on the maser disk observations for the individual sources). Therefore, since it is unclear whether either of the scenarios applies (the maser emission may actually arise from the disks), we consider all the sources as maser disks and our analysis is based on this assumption. The MCP is an ongoing project and the maser disk properties such as disk sizes and orientations have not yet been measured for all the candidates.

For instance, the distances measured by the MCP (which are among the most accurate ones), are only available for four sources in our sample. These distances are in agreement within uncertainties with the distances listed in the NASA/IPAC Extragalactic Database (NED)[1]. For consistency we adopted the NED distances since they are available for all sources in our sample. The NED distances were obtained using H_0=70.0 km s^{-1} Mpc^{-1}, Ω_{matter}=0.27, and Ω_{vacuum}=0.73 as the cosmological parameters. H_2O maser luminosities from the literature were also rescaled to H_0=70.0 km s^{-1} Mpc^{-1} to be consistent with other luminosities in this work.

3.3 Observations and data reduction

Our sample was observed between October and November 2015 using the VLBA in C band. The synthesized beamwidth was in the range from 3.3 to 6.5 mas. We used a total bandwidth of 128 MHz (2×64 MHz IFs, 4.644 to 4.708 GHz and 4.836 to 4.900 GHz) and right-hand circular polarization. The sources were grouped into six sets of three for observation, with a total time of 7 hours per group and an integration time of ~1.5 hours per target after (i.e., excluding) calibration. Our observations included two scans of fringe finders, one placed at the beginning and one at the end of the observations. The sources and their associated calibrators were observed alternating in scans of ~1 minute. Table 3.1 indicates fringe finders and calibrators, and the *J*2000 coordinates obtained from previous VLA observations. Of the 18 observed sources, 5 were detected at a signal-to-noise ratio (S/N) of 8 or higher. In the case of four of these detected sources, Mrk 0001, Mrk 1210, Mrk 1419, and UGC 3193, the initial images did not have a sufficiently high quality. Therefore, to check our detections and obtain higher S/N values, we re-observed them with the VLBA in C band, between October and November 2017. This time they were grouped in two sets of two sources, with a total

[1] https://ned.ipac.caltech.edu/

Table 3.1: VLBA observations.

Galaxy	**Right Ascension/ Declination** *J*2000	**Fringe Finder**	**Calibrator**	**RA/Dec uncertainty** (arcsec)
Mrk 0001/NGC 0449	$01^h16^m07^s.20/ + 33°05'21.''75$	2007+777/ 3C84	J0137+3122/J0112+3208	0.02 / 0.02
J0126-0417	$01^h26^m01^s.64/ - 04°17'56.''23$	2007+777/ 3C84	J0123-0348	0.04 / 0.04
NGC 0591/Mrk 1157	$01^h33^m31^s.23/ + 35°40'05.''79$	2007+777/ 3C84	J0137+3309	0.10 / 0.11
Mrk 1029	$02^h17^m03^s.57/ + 05°17'31.''15$	2007+777/ DA193	J0215+0524	0.18 / 0.18
NGC 1194	$03^h03^m49^s.11/ - 01°06'13.''48$	2007+777/ DA193	J0259-0019	0.03 / 0.03
J0350-0127	$03^h50^m00^s.35/ - 01°27'57.''40$	2007+777/ DA193	J0351-0301	0.15 / 0.15
J0437+6637	$04^h37^m08^s.28/ + 66°37'42.''10$	2007+777/ DA193	J0449+6332/ J0429+6710	0.12 / 0.12
UGC 3193	$04^h52^m52^s.56/ + 03°03'25.''52$	2007+777/ DA193	J0453+0128	0.11 / 0.29
NGC 2273	$06^h50^m08^s.69/ + 60°50'45.''10$	2007+777/ DA193	J0638+5933	0.28 / 0.27
UGC 3789	$07^h19^m30^s.95/ + 59°21'18.''37$	3C84/ 4C39.25	J0737+5941	0.08 / 0.08
Mrk 0078	$07^h42^m41^s.73/ + 65°10'37.''39$	3C84/ 4C39.25	J0737+6430	0.03 / 0.03
Mrk 1210/Phoenix	$08^h04^m05^s.86/ + 05°06'49.''83$	DA193/ 4C39.25/ 3C345	J0803+0421	0.03 / 0.03
Mrk 1419/NGC 2960	$09^h40^m36^s.38/ + 03°34'37.''36$	3C84/ 4C39.25	J0930+0034	0.14 / 0.13
NGC 4388	$12^h25^m46^s.78/ + 12°39'43.''77$	DA193/ 4C39.25/ 3C345	J1225+1253	0.02 / 0.02
NGC5765b	$14^h50^m51^s.5/ + 05°06'52.''0$	DA193/ 4C39.25/ 3C345	J1458+0416	1.25/ 1.25
UGC 9639/Mrk 0834	$14^h58^m35^s.99/ + 44°53'01.''0$	4C39.25/ 2007+777	J1459+4442	0.5/ 0.5
NGC 6264	$16^h57^m16^s.13/ + 27°50'58.''5$	4C39.25/ 2007+777	J1659+2629	0.5/ 0.5
NGC 6323	$17^h13^m18^s.07/ + 43°46'56.''8$	4C39.25/ 2007+777	J1707+4536	0.5/ 0.5
Mrk 0001	$01^h16^m07^s.209/ + 33°05'21.''634$	3C84	J0119+3210	0.001/ 0.001
UGC 3193	$04^h52^m52^s.5569/ + 03°03'25.''768$	3C84	J0459+0229	0.001/ 0.001
Mrk 1210	$08^h04^m05^s.8570/ + 05°06'49.''846$	4C39.25/ 3C84	J0803+0421	0.0008/ 0.002
Mrk 1419	$09^h40^m36^s.3835/ + 03°34'37.''289$	4C39.25/ 3C84	J0930+0034	0.001/ 0.001

Notes. Column 1: Name of galaxy. The sources in bold hold clean maser disks (see Sect. 3.2). Column 2: *J*2000 right ascension and declination. For NGC 5765b, NGC 6323, NGC 6264, and UGC 9639 the coordinates are taken from NED, and for the remaining sources the coordinates are from Kamali et al. (2017). Column 3: Fringe finders. Column 4: Phase calibrators. Column 5: Right ascension and declination uncertainties. The second VLBA observations are presented in the lower part. The pointing coordinates for the second observations were taken from the first run of VLBA observations.

time of 8 hours per group (2.5 hours on-source per target, after calibration), bandwidth of 256 MHz (8×32 MHz IFs, from 4.836 to 5.092 GHz) and dual polarization. The data were calibrated using the Astronomical Image Processing System (AIPS) software package developed by the National Radio Astronomy Observatory (NRAO). At first, the ionospheric dispersive delays and the Earth orientation parameters were corrected using AIPS tasks VLBATECR and VLBAEOPS, respectively. Then, using the task CLCOR, the parallactic angle correction was applied. The visibilities were normalized by the auto-correlations with the task ACCOR. The instrumental phases and delays were removed using the fringe finders listed in Table 3.1 and task VLBAMPCL. Amplitude corrections were applied using system temperature and the antenna gain information by the APCAL task in AIPS. We solved phases, delays, and rates by performing fringe fitting on the calibrators listed in Table 3.1 assuming a point source model, and applied the solutions to the targets. For imaging, we used the task IMAGR in AIPS. Different weighting functions (including tapering of the uv-distances) were tried to find the optimum solution for a better S/N.

3.4 Results

Out of 18 sources observed, 5 were detected: Mrk 0001, Mrk 1210, Mrk 1419, NGC 2273, and UGC 3193. Figure 3.1 shows the 5 GHz radio continuum maps. For all images, phase self-calibration was employed to improve the image quality, using a solution interval of 1 minute. For Mrk 0001 the S/N was improved from 8 to 32, for Mrk 1210 from 36 to 62, for Mrk 1419 from 12 to 18, for NGC 2273 from 56 to 61, and for UGC 3193 from 8 to 36. For detected sources we fitted two-dimensional Gaussians on the individual components using the task JMFIT in AIPS in order to obtain source properties such as peak and integrated flux, position, and its uncertainty (when the continuum components are more complicated, multi-Gaussians are fitted over emission $> 3\,\sigma$). The result is presented in Table 3.2. For detected sources, when a source has more than one component, the flux reported in Table 3.2 is the total flux density which includes all the components[2]. For positions reported in Tables 3.1 and 3.2, the uncertainties include the statistical uncertainty, the uncertainty in the phase calibrator position or the calibrator's size if the calibrator is resolved, and the systematic errors which are estimated from $(\Psi^2 + \mathrm{beam}^2)^{1/2} \times (1/[\mathrm{S/R}] + 1/20)$, where Ψ is the source major axis, beam is the beam size, and S/R is the signal-to-noise ratio (White et al. 1997).

3.4.1 Continuum images and previous radio observations

Here we review our maps and other radio observations available in the literature for the five detected sources.

- Mrk 0001
We observed compact radio emission in our 33 GHz radio maps with a position angle (PA) of $120^\circ \pm 2^\circ$. In the C-band VLBA data we see extended emission, also in the northwest-southeast direction. The maser disk has a PA of $6.4^\circ \pm 10^\circ$ and its rotation axis is by $17^\circ \pm 11^\circ$ misaligned from the jet propagation direction. The systemic masers are not observed in this source (Kuo et. al. in. prep.).

[2] The radio luminosities are also obtained from the total flux densities unless mentioned otherwise.

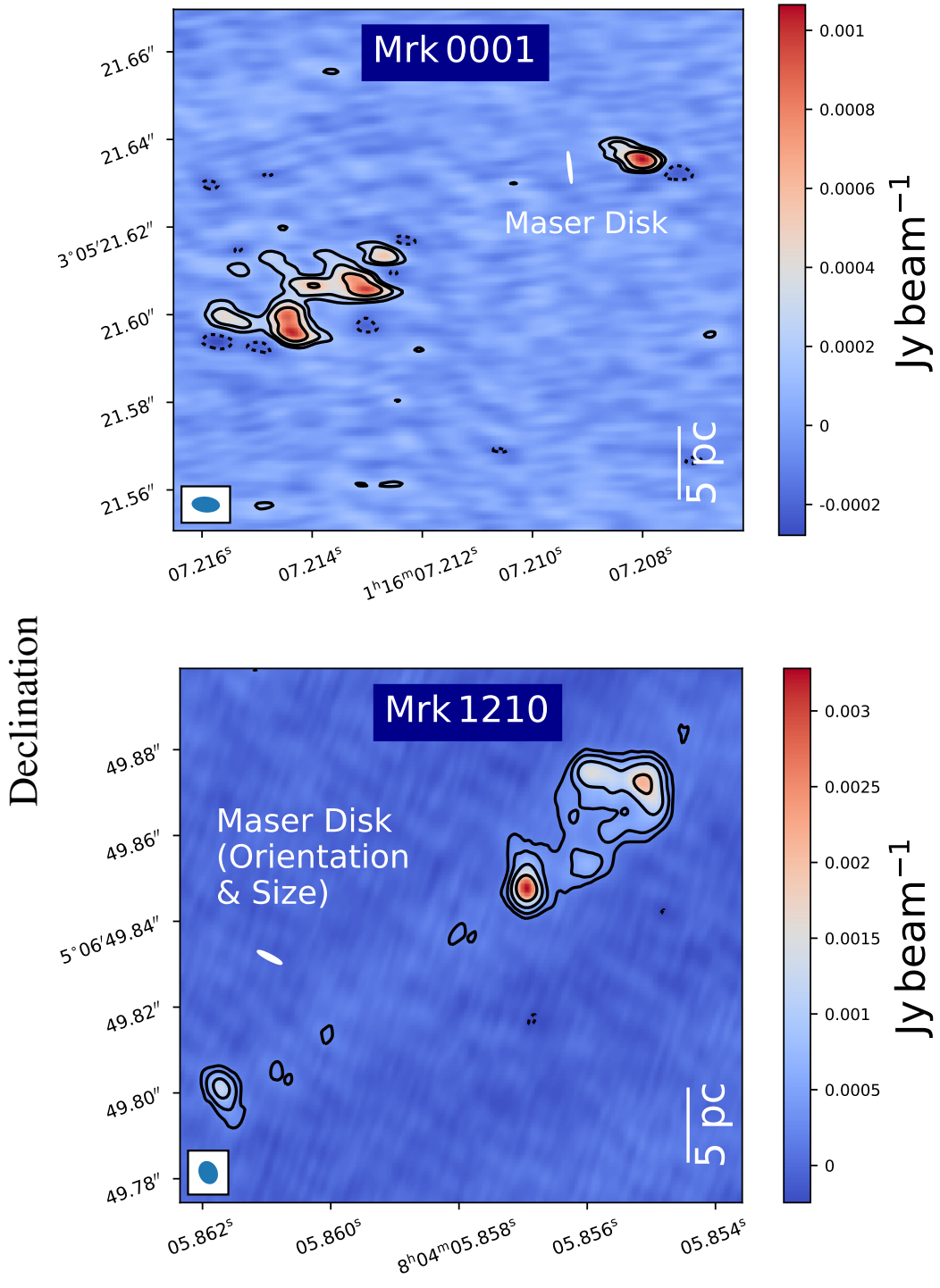

Figure 3.1: 5 GHz contour maps. The contour levels are ±3, 6, 12, and 24 times the rms given in Table 3.3. The synthesized beam is shown in the lower left corner of each plot. For UGC 3193 the maser disk size; for Mrk 1210 the maser disk size and orientation; and for Mrk 0001, Mrk 1419, and NGC 2273 the maser disk size, orientation, position, and position uncertainties (light orange squares) are shown. For Mrk 0001 the maser position uncertainty is small. For Mrk 1210 and UGC 3193 the positions of the maser disks are not yet known. For NGC 2273, two contour maps using different Briggs weighting functions are shown: robust parameter 5, which is a pure natural weighting (left) and 0, which is between natural and uniform (right).

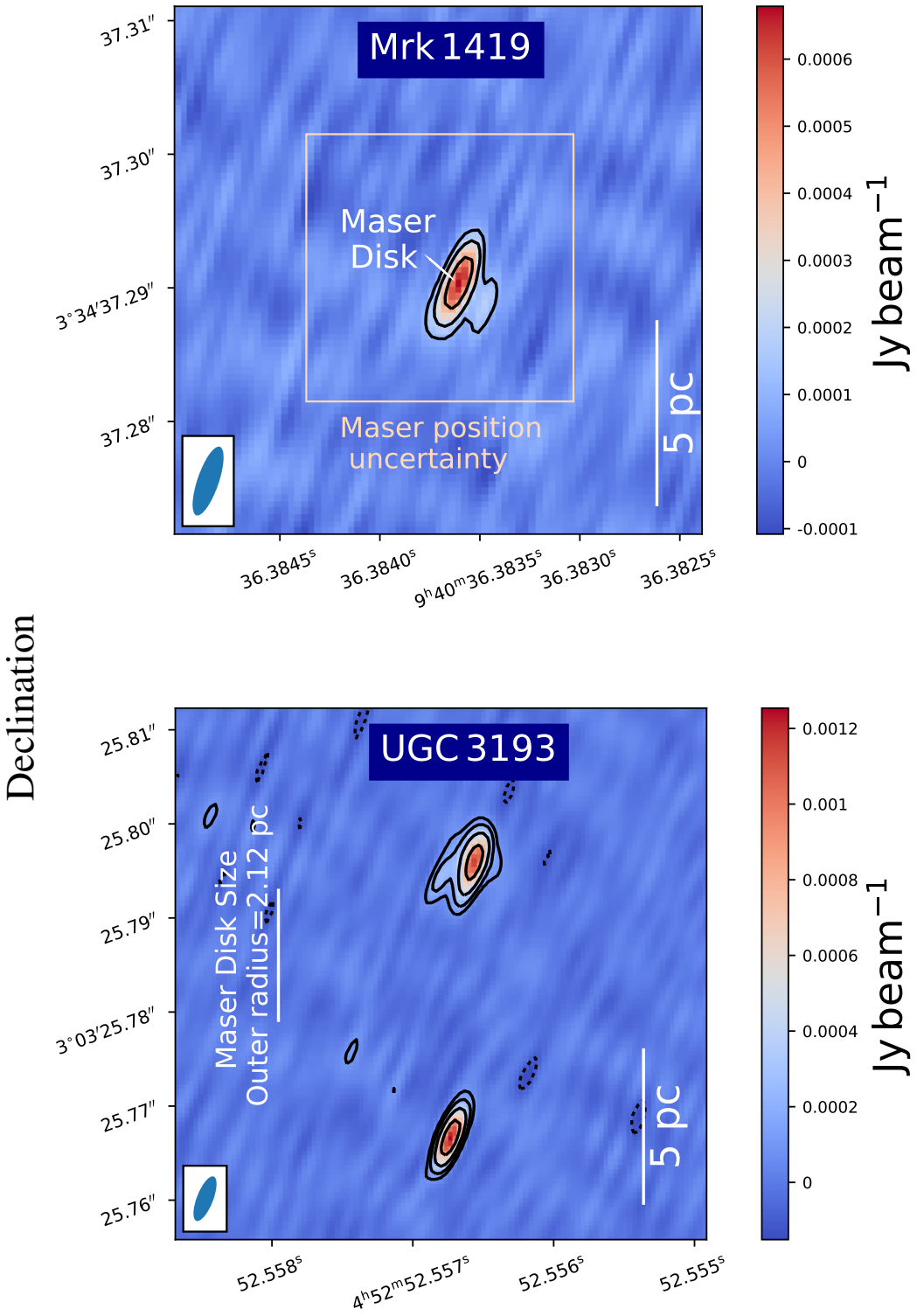

Figure 3.1: *(cont.)*

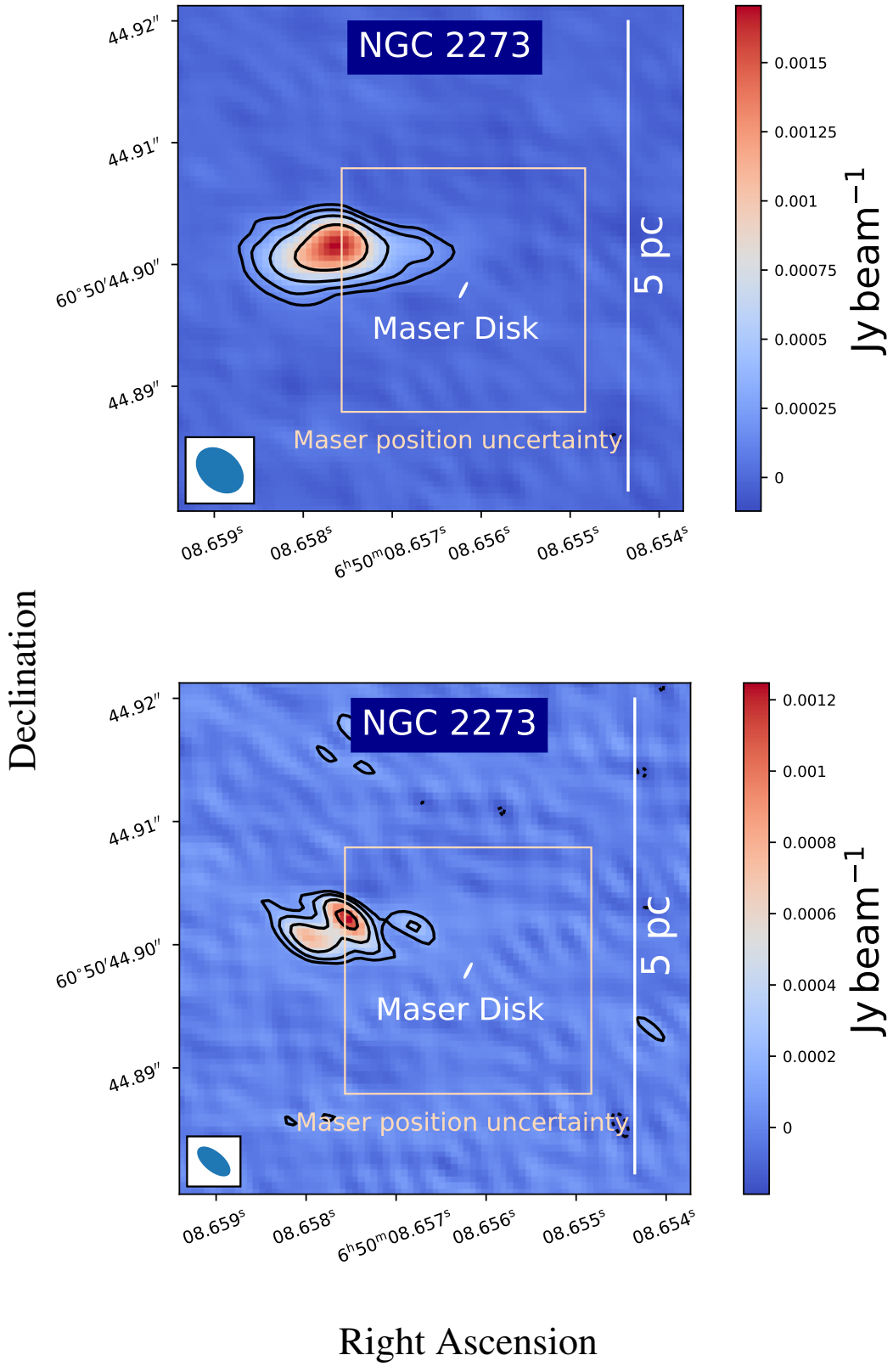

Figure 3.1: *(cont.)*

Table 3.2: Obtained properties for detected sources.

Galaxy	**5 GHz peak flux** (mJy/beam) first obs || second obs	**5 GHz integrated flux** (mJy) first obs || second obs	**Right Ascension/ Declination**	**Uncertainties** (mas/mas)	α_5^{33}	T_b (K)	**Putative core**
Mrk 0001	1.30±0.09 || 1.05 ± 0.05	8.6±0.8 || 8.9±0.3	$01^h16^m07^s.208/ +33°05'21.''636$	0.018/ 0.017	0.39±0.03	6.5×10^6	NW
Mrk 1210	0.92±0.07 || 3.10 ± 0.07	15.05±0.8 || 17.9± 0.7	$08^h04^m05^s.8570/ +05°06'49.''848$	0.0008/ 0.002	0.40±0.01	1.3×10^7	CN
Mrk 1419	0.94±0.06 || 0.66 ± 0.03	1.7±0.2 || 0.7±0.3	$09^h40^m36^s.3835/ +03°34'37.''289$	0.001/ 0.001	0.31±0.09	$> 2.6 \times 10^6$	...
NGC 2273	1.6 ± 0.03 || ...	3.3±0.1 || ...	$06^h50^m08^s.6577/ +60°50'44.''9012$	0.0005/ 0.0006	0.11±0.06	9.1×10^6	...
UGC 3193	0.7±0.06 || 1.3 ± 0.03	2.0±0.1 || 3.0±0.9	$09^h40^m36^s.3836/ +03°34'37.''290$	0.0004/ 0.001	-0.14±0.04	1.3×10^7	N

Notes. Column 1: Name of galaxy. The sources in bold hold clean maser disks (see Sect. 3.2). Column 2: 5 GHz peak flux density of the brightest component. Column 3: 5 GHz integrated flux. For detected sources with multiple components the reported flux is the sum of the fluxes from all the components. Column 4: $J2000$ right ascension and declination obtained (except for NGC 2273) from the second observations for the peak position of the brightest component. Column 5: Right ascension and declination uncertainties. Column 6: Spectral index obtained from 33 GHz VLA observation and 5 GHz VLBA observations assuming a power law dependence of $S \propto \nu^{-\alpha}$. Column 7: Brightness temperatures. If the source is unresolved, a lower limit is given. Column 8: Putative core of the AGN, corresponding to the component with highest brightness temperature. NW stands for northwestern, CN for central, and N for northern.

- Mrk 1210
As mentioned before, four of our VLBA detected sources were re-observed to obtain higher S/N values. While morphologies are very similar for three sources in both observations, for Mrk 1210 the southeastern component was not detected in the data set from the first observations and the northwestern extended emission is less prominent in this data, likely due to insufficient sensitivities. A former 6 cm VLBA observation of this galaxy has shown a structure similar to those found in our re-observations, which is shown in Fig. 3.1, except that the northwestern component is resolved into four subcomponents (Middelberg et al. 2004). The flux reported by Middelberg et al. (2004) for the central component in Fig. 3.1 is the same as in our observations (5 mJy). However, the flux reported for the northwestern component is less than ours (9.1±1.1 mJy compared to 13.7±0.4 mJy). The southeastern component is considered a tentative detection in the work of Middelberg et al. (2004) and therefore no flux is reported for this component. Identifying the core of the galaxy the jet is emanating from is not easy since both northwestern and central components have steep spectra. Middelberg et al. (2004) reported a spectral index of $\alpha_{6\,\mathrm{cm}}^{18\,\mathrm{cm}}$=1.26 for the northwestern and $\alpha_{6\,\mathrm{cm}}^{18\,\mathrm{cm}}$=0.78 for the central component obtained from VLBI observations with matching beam sizes using the $S \propto \nu^{-\alpha}$ convention. The maser configuration is consistent with a rotating disk. However, only one single maser component is detected at the systemic velocity of the galaxy. The high velocity masers also deviate slightly from an edge-on, flat, Keplerian disk model. This implies that if the masers arise from a disk, its inclination is deviating $\sim 10^\circ$ from an edge-on disk (inclination=$100.68^{+1.13\circ}_{-0.90}$), and there is potential warping or eccentricity in the disk (Zhao et al. 2018). Mrk 1210 shows long-term variability in the X-rays and has changed from Compton-thick to Compton-thin over a period of approximately 17 years (Masini et al. 2017). This variability was interpreted as a combination of the intrinsic variability of the AGN and presence of an obscuring cloud passing through the line of sight.
- Mrk 1419
This galaxy poses a clean maser disk (Kuo et al. 2011). Sun et al. (2013) reported extended emission with a PA of $125^\circ \pm 10^\circ$ from 20 cm radio data. In our VLA maps we see a weak extension in the southeast-northwest direction with a PA of $117^\circ \pm 84^\circ$. Gaussian deconvolution of our 5 GHz map shows a compact component that is not clearly resolved and may contain a weak extension with a PA of $159^\circ \pm 2^\circ$. The outer part of the maser disk shows some degree of warping (Kuo et al. 2011).
- NGC 2273
This galaxy poses a clean maser disk (Kuo et al. 2011). NGC 2273 was previously observed with the VLBA at C band in 2004 by Lal et al. (2004) and showed a compact radio core. Anderson & Ulvestad (2005) observed this galaxy at 8.4 GHz with the VLBA and detected radio emission extended along the northwest to southeast direction with a beam width of approximately 2 mas × 1 mas. The structure is similar to our map shown in the lower right panel of Fig. 3.1. The distribution of the masers shows a hint of a warp in the disk (Kuo et al. 2011).
- UGC 3193
In our 33 GHz data, we see extended emission in the north-south direction, the same as we observe in the C-band VLBA data. The southern component is not resolved in the Gaussian deconvolution. The maser disk orientation and position is not yet known for UGC 3193.

3.4.2 A note on the non-detections

About 72% of the sources in our original sample of 18 sources were not detected. Considering that ~70% of the undetected sources were previously detected in our VLA observations and

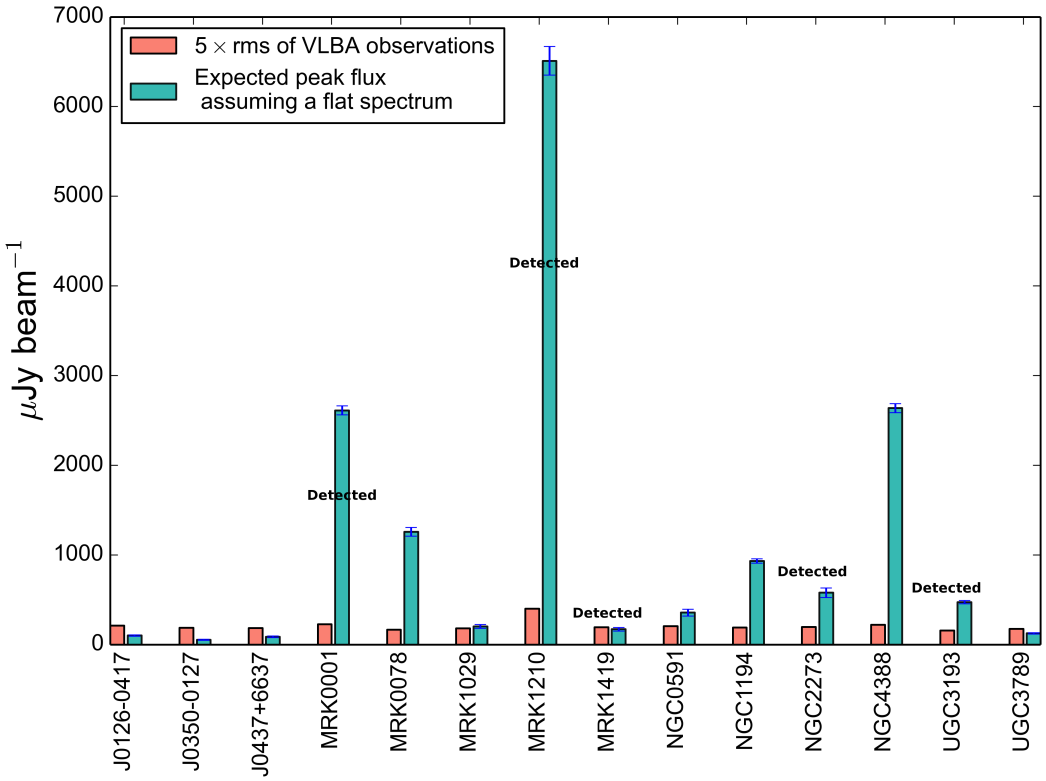

Figure 3.2: Expected flux densities in the case of a flat radio spectrum compared to the rms noise of the maps. The five detected sources are labeled.

assuming a flat spectrum or rising flux densities with decreasing frequency, we might expect to detect these sources in the VLBA observations. Figure 3.2 shows the expected flux at 5 GHz (assuming a flat spectrum) and the 5×rms noise of our VLBA maps (for a 5σ detection limit of a single spatially unresolved continuum component). The five detected sources are among the brightest ones as shown in Fig. 3.2. However, there are similarly bright sources among the undetected ones. Either these sources have inverted spectra, or extended emission is resolved out. Time variability of AGNs is another issue that could affect the detection rates. We searched for trends of common properties among the detected sources, such as X-ray, IR, radio, or maser luminosity limits, but did not succeed in finding any. We report 3σ upper limits for the undetected sources, rms of our maps, as well as hard X-ray and 33 GHz fluxes in Table 3.3.

3.5 Discussion

3.5.1 Orientation of the jets with respect to the maser disks

In NGC 4258, the prototypical H_2O megamaser galaxy, the rotation axis of the maser disk is aligned with the inner part of the extended jet (Cecil et al. 1992). Here we focus on identifying the orientation of the jet with respect to that of the maser disk in our sample. Once again we note that two of the detected sources, Mrk 1419 and NGC 2273, are among the clean maser disks (see Sect. 3.2), while the other three detected galaxies, Mrk 0001, Mrk 1210, and UGC 3193, are among those exhibiting a non-clean disk, i.e., the masers might arise from either disks or outflows. In the following discussion, we consider the possibility that the masers arise from the

Table 3.3: Sample properties.

Galaxy	**Distance** (Mpc)	**5 GHz upper limits** (mJy)	**rms** (μJy/beam) first obs || second obs	**33 GHz flux** (mJy)	**Hard X-ray flux** (10^{-11}erg s^{-1} cm^{-2})	**log L_{H_2O}** ($L_\odot$)	**Type of activity**
J0126-0417	76.2 ± 5.4	< 0.13	42.5	0.14 ± 0.02	<0.34	2.1	*U*
J0350-0127	174.2 ± 12.2	< 0.13	37.6	0.17 ± 0.04	$0.45^{+0.17}_{-0.16}$	3.7	*U*
J0437+6637	52.9 ± 3.7	< 0.13	36.8	0.11 ± 0.02	0.29±0.14	1.4	*U*
Mrk 0001	64.2 ± 4.5	...	45.6 || 49.7	3.97 ± 0.13	<0.32	1.9	Sy2
Mrk 0078	159.9 ± 11.2	< 0.10	33.4	1.69 ± 0.11	0.63 ± 0.18	1.6	Sy2
Mrk 1029	126.0 ± 8.8	< 0.11	36.7	1.29 ± 0.16	<0.35	2.8	*U*
Mrk 1210	61.3 ± 4.3	...	80.0 || 32.0	8.14 ± 0.43	3.58±0.20	2.0	Sy2, Sy1
Mrk 1419	75.3 ± 5.3	...	39.0 || 37.0	0.36 ± 0.07	<0.34	2.7	LINER
NGC 0591	61.1 ± 4.3	< 0.11	41.3	1.52 ± 0.12	$0.37^{+0.12}_{-0.11}$	1.5	Sy2
NGC 1194	55.4 ± 3.9	< 0.12	38.5	1.05 ± 0.04	2.21±0.18	2.8	Sy 1.9
NGC 2273	26.8 ± 1.9	...	39.7	3.04 ± 0.36	0.67 ± 0.16	0.9	Sy2
NGC 4388	40.8 ± 2.9	< 0.13	44.6	3.01 ± 0.08	$15.81^{+0.16}_{-0.15}$	1.2	Sy2
NGC 5765b	122.0 ± 8.5	< 0.11	37.2	...	$0.40^{+0.17}_{-0.18}$	3.6	*U*
NGC 6264	145.4 ± 10.2	< 0.12	38.5	...	<0.32	3.1	Sy2
NGC 6323	110.6 ± 7.8	< 0.12	39.1	...	<0.30	2.7	Sy2
UGC 3193	63.2 ± 4.4	...	31.3 || 34.0	0.80 ± 0.05	<0.39	2.5	*U*
UGC 3789	47.4 ± 3.3	< 0.11	35.0	0.20 ± 0.02	$0.26^{+0.14}_{-0.13}$	2.7	Sy2
UGC 9639	155.9 ± 10.9	< 0.09	30.0	...	<0.26	2.6	LINER

Notes. Column 1: Name of galaxy. The sources in bold hold clean maser disks (see Sect. 3.2). Column 2: Hubble flow distances (relative to the 3 K Cosmic Microwave Background) in Mpc, assuming H_0=70 km s^{-1} Mpc^{-1} (see Sec. 2). Column 3: 3σ upper limit for the non-detections in the VLBA 5 GHz observations. Column 4: rms of the 5 GHz maps. Column 5: 33 GHz integrated flux densities with uncertainties (Kamali et al. 2017). Column 6: Swift/BAT hard X-ray fluxes (20-100 keV) with uncertainties (Litzinger et al.in prep.). Column 7: Logarithm of water maser luminosity in units of solar luminosity (Zhang et al. 2012, modified for H_0=70 km s^{-1} Mpc^{-1}). The NGC 5765b and UGC 9639 data are from Kuo et al. (2018). Column 8: Types of nuclear activity following NED; *U* stands for unidentified.

Table 3.4: Position angles (PAs).

Galaxy	maser disk (degree)	5 GHz jet direction (degree)	jet offset (degree)	33 GHz continuum (degree)	galaxy scale (degree)	ref
Mrk 0001	6.4±10	113±5	17±11	120±2	77.5	1
Mrk 1210	62.58±0.45	127±22	26±22	179±83	160.0	2
Mrk 1419	49±0.7	159±2	20±1	117±84	40.2	3
NGC 2273	153±4.6	95±1	32±5	83±3	63.3	3
UGC 3193	—	175±0.2	—	167±4	177.4	—

Notes. Column 1: Name of galaxy. The sources in bold hold clean maser disks (see Sect. 3.2). Column 2: Maser disk PAs and their uncertainties. Column 3: Jet propagation direction, obtained from a linear fit on the position of the flux maxima in multicomponent sources (see Sect 3.5.1). If there is only one component, the 5 GHz continuum PA of this component represents the jet propagation direction. Column 4: PA difference between the disk rotation axis (the normal vector to the disk) and jet propagation direction and the uncertainties. Column 5: 33 GHz larger scale PAs from Kamali et al. (2017). Column 6: Large-scale galactic disk PA from HyperLeda. Column 7: References for maser disk PA. (1) Kuo et. al. (in prep.); (2) Zhao et al. (2018); (3) Kuo et al. (2011).

circumnuclear disk surrounding the SMBHs[3]. Then for four out of the five detected galaxies in our sample, Mrk 0001, Mrk 1210, Mrk 1419, and NGC 2273, the maser disk orientation is known (see Sect. 3.4 for more information). As mentioned before, in our sample the maser disk is viewed edge-on (±10°) and the normal vector to the disk is in the plane of the sky. We do not apply any inclination corrections to the measured PAs. Instead we assume that the PA (measured east of north) of the radio continuum shows the PA of the elongation of the jet. If more than one component is detected, we assume that a line going through the central position of each component (obtained from Gaussian fits) represents the jet propagation direction. The same convention for measuring the PAs (east of north) is used for all other reported PAs.

For all four sources, the jets are misaligned with respect to the normal vector to the maser disk. However, they are confined to a cone within ~0.6 radians (32°) of the disks' normal. Table 3.4 presents PAs obtained in this work and from the literature, and Fig. 3.3 shows a comparison between the PAs of different scale disks and the radio continuum. For the null hypothesis that the jets have random distribution in space (which means they are not linked with the maser disk's rotation axis), the probability that we observe these four measured PA offsets is 0.009, indicating that the jet orientations are not random with a 99.1% confidence level (see Appendix 3.7 for more details). On the other hand, the PA offset may be related to the outer and inner radii of the disk: the larger the disk size, the smaller the offset (see Figs. 3.4 and 3.5). We note, however, that our conclusion is based on a sample of four sources only (where two of them are non-clean disks), so that a study of a larger sample is needed to verify or falsify our finding.

3.5.2 Multiscale position angle

The PAs of disks on different scales are available for three of the VLBA-detected sources (Greene et al. 2013; Pjanka et al. 2017). Therefore, we can compare the alignment of the

[3] For clarity, clean maser disks and non-clean maser disks are shown with different markers in our plots.

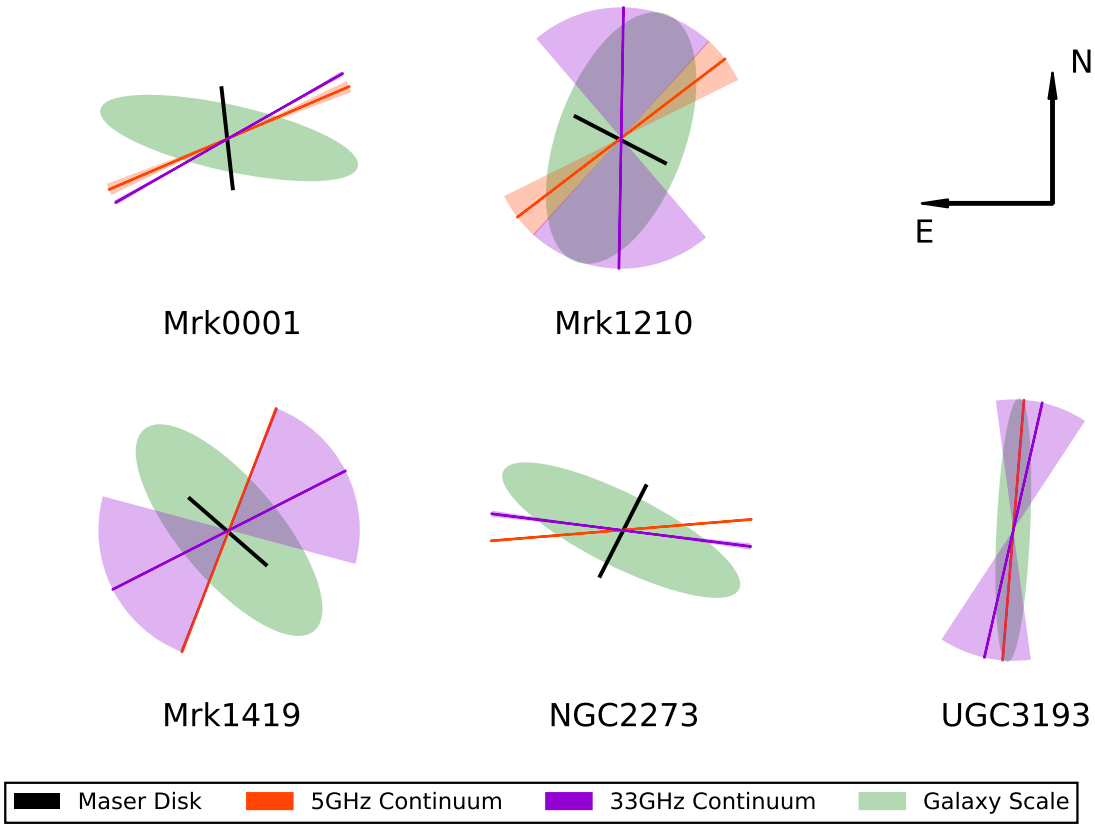

Figure 3.3: Position Angles (PAs) on different scales. The galaxy scale PA is shown as a green ellipse. The minor axis of the ellipse represents the inclination of the galaxy, i.e., the broader the minor axis, the lower the inclination. The 5 GHz VLBA and 33 GHz VLA radio continuum PAs are shown with orange and violet solid lines, respectively, and the uncertainties on the PA of the radio continuum are shown as shaded wedges. The maser disk is shown as a black solid line. For UGC 3193 detailed maser images are not yet available. The sizes of the ellipses, lines, and wedges do not represent correct relative scales.

jet with the angular momentum orientation of the disks on different scales. Our VLBA radio continuum in Mrk 1210 is misaligned by ~26° with the maser disk's normal. However, it is misaligned with the nuclear region of the galaxy (with size of 170 pc) by only ~8°. The radio continuum orientation is displaced by ~57° from the angular momentum orientation of the large-scale disk. For NGC 2273, the VLBA radio continuum is not aligned with any of the rotation axes: ~32° from the maser disk's normal, ~36° from the angular momentum orientation of the nuclear 150 pc scale disk, and ~58° from the normal vector to the galaxy's large-scale disk. In Mrk 1419, which has likely experienced a merger or some interaction (Läsker et al. 2016), the maser disk and the nuclear region with a size of 270 pc are aligned and the jet is ~20° from the angular momentum direction of this disk, while the galaxy's large-scale disk has a normal vector that is ~29° away from the jet direction.

3.5.3 Radio continuum positions relative to the maser positions

Compact radio emission is detected in the nuclei of most galaxies (Herrnstein et al. 1997, and references therein). Since the centers of the maser disks are the gravitational centers of the nuclear regions, we expect the centers of the maser disks to coincide with their radio

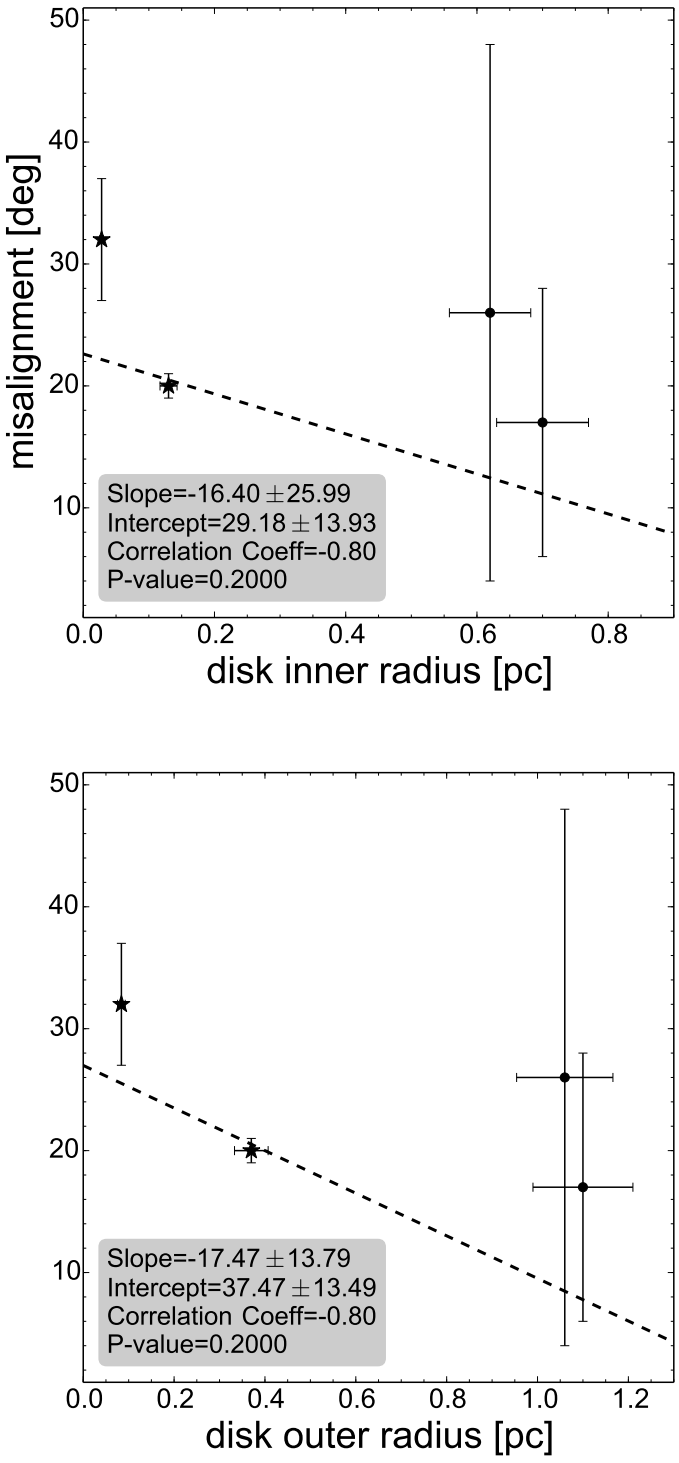

Figure 3.4: Misalignment of the jet and the normal to the maser disk vs. inner (left) and outer (right) radius of the maser disk. The clean maser disks are shown as stars and the non-clean disks as dots.

Table 3.5: Separation of the maser disk from the continuum sources.

Galaxy	**δ RA** (mas)	**δ Dec** (mas)	**Reference**
Mrk0001	4.5±1.0	0.4±1.0	1
Mrk1419	1.5±10.0	1.5±10.0	2
NGC2273	22.5±10.0	3.3±10.0	2

Notes. Column 1: Name of galaxy. Column 2: Separation of the maser disk from the center of the 5 GHz nuclear continuum source and the uncertainties. For Mrk 0001 the separation is for our first observation and with respect to the continuum source in the northwest of the image. Column 3: References for maser disk positions. (1) Kuo et al. in prep.; (2) Kuo et al. (2011).

continuum core representing the nucleus of the galaxy. For three sources among the detected ones, Mrk 0001, Mrk 1419, and NGC2273, the maser positions are available. For our radio continuum data the central position from the Gaussian fit of the component with the highest brightness temperature (if there is more than one) is considered as the position of the nuclear source (see Sect.3.5.4). In Table 3.5 we present the spatial offsets of the maser disk with respect to the radio continuum. For Mrk 1419 and NGC 2273, the maser positions are from VLA observations. Within the uncertainties, the maser positions for all three sources are consistent with those of the radio continuum. For Mrk 0001, however, in our second observations the phase calibrator was resolved with a major axis of ~ 15 mas and therefore we report the position offset with respect to the continuum position in our first observations which has a higher position accuracy. The proper motion of the galaxies can be neglected. In the case of a speed of 1000 km s^{-1} in the plane of the sky and a distance D = 50 Mpc, the expected shift is only 4 μarcsec yr^{-1}.

3.5.4 Spectral indices and brightness temperatures

We obtained the spectral indices for the detected sources between 33 GHz and 5 GHz. They are presented in Table 3.2. The indices were obtained assuming a power-law dependence for the fluxes ($S \propto \nu^{-\alpha}$). We should note that the VLA observations have linear beam sizes about 100 times those of the VLBA observations. The spectral indices have a mean of α=0.21±0.20.

We also obtained the brightness temperatures (T_B), using

$$T_b = \frac{2\,ln(2)}{k_B\,\pi}\frac{\lambda^2\,S_{tot}}{\theta_{maj}\,\theta_{min}}, \tag{3.1}$$

where k_B is the Boltzmann constant, S_{tot} is the total flux density, λ is the wavelength of observation, and θ_{maj} and θ_{min} are the deconvolved sizes of the major and minor axes of the source. When the component is unresolved, the beam size is used as an upper-limit for the source size. Therefore, the corresponding T_B is a lower limit. The obtained brightness temperatures are listed in Table 3.2. For sources with more than one component, we give the measurement for the component with highest T_b, which we identify as the putative core of the

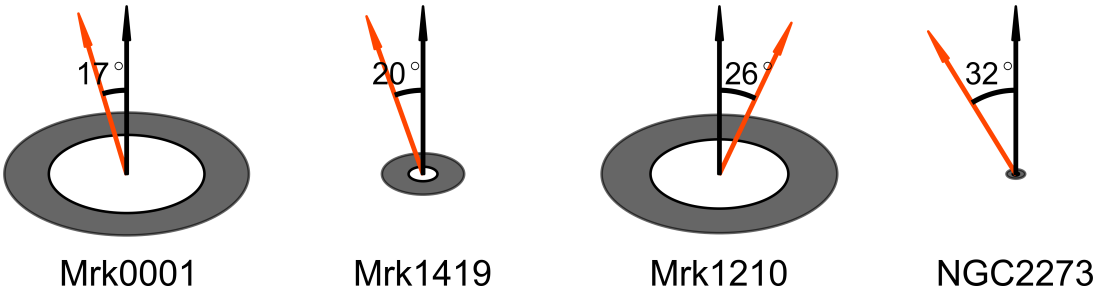

Figure 3.5: Misalignment of the jet (orange arrow) and the rotation axis (black arrow) of the maser disk (see also Table 3.4). The disk sizes are to scale with respect to each other.

AGN. It should be noted that we do not know the spectral indices for the individual components; therefore, the brightness temperature is the only tool that can tentatively define the AGN's core. All sources have $T_B > 10^6$, consistent with non-thermal emission.

3.5.5 Radio luminosity versus other properties of the galaxies

Radio luminosity versus X-ray luminosity and the SMBH mass: fundamental plane of black hole activity

The fundamental plane (FP) of black hole activity is an empirical relation between the radio continuum luminosity, X-ray luminosity, and black hole (BH) mass. This relation holds for 10 orders of magnitude in radio luminosity and ranges from stellar mass BHs (in X-ray binaries) to SMBHs, supporting the idea that jet physics is scale invariant (Merloni et al. 2003). For many years there have been efforts to understand the accretion mechanism in the SMBHs and how the accretion rate is related to the SMBH mass and the radio and X-ray luminosities. Studies have suggested that the radio luminosity depends on both SMBH mass and accretion rate of material onto the black hole (Falcke & Biermann 1995). The SMBH mass can be determined observationally, and the accretion rate can be inferred through measuring the luminosity at those frequencies at which the accretion process dominates. For example, the accretion flow can be inferred from the X-ray luminosity since the X-ray emission is produced by the accretion of material onto the SMBHs. The scaling of the X-ray luminosity with the accretion rate depends on the physics of the disk, e.g., whether it is radiatively efficient or not (a quantitative description of these models is beyond the scope of this paper; see Merloni et al. 2003, and references therein). The X-ray emission could also be produced by the inverse Compton effect involving synchrotron radiation. In summary, we expect the core radio luminosity to be correlated with the X-ray luminosity and also with the black hole mass.

The following plane equation describes the FP of BH activity

$$log\, L_R\, [erg\, s^{-1}] = \xi_X\, log\, L_X\, [erg\, s^{-1}] + \xi_M\, log\, M\, [M_\odot] + b_R, \tag{3.2}$$

where L_R, L_X, and M are the radio luminosity, X-ray luminosity, and the BH mass, respectively; b_R is the zero intercept; and ξ_X and ξ_M are the linear regression coefficients. The coefficients in Eq. 3.2 depend on the accretion efficiency, electron spectral index, viscosity of the disk and initial conditions at the base of the jet such as dependence of magnetic energy density on the SMBH mass and accretion rate. Others have followed the lead of Merloni et al. (2003) and investigated the FP using different subsamples (e.g., Saikia et al. 2015; Körding et al. 2006; Gültekin et al. 2009; Bonchi et al. 2013; Nisbet & Best 2016). All these studies fit similar

coefficients, which is somewhat surprising since the SMBH mass determinations differ from sample to sample. We note that a sample for which accurate BH mass measurements have been obtained from edge-on megamaser disks has not yet been analyzed.

Adopting X-ray luminosities from Litzinger et al. (in. prep.), obtained using data from the *Swift*/BAT instrument in a range of 20-100 keV (see Table 3.3), the black hole masses from the MCP and radio luminosities from this work, we fitted the same function to our data using the least-squares method. The fitting parameters are shown in the first row of Table 3.6. We considered increasing the number of sources for this analysis by extrapolating the 5 GHz luminosities from the 33 GHz radio luminosities, using the mean of the indices between our 33 GHz and 5 GHz observations (see Table. 3.2). This sample with extrapolated fluxes includes 12 sources that have known SMBH masses. The result of the fit is presented in the second row of Table 3.6. We should note that the mentioned studies that probe the FP use soft X-ray data (2-10 keV) and this can cause a discrepancy with our result. We also tried to fit Eq.3.2 to a sample of five sources for which we have soft X-ray data (Masini et al. 2016) and extrapolated 5 GHz fluxes. The fitting parameters are shown in the third row of Table 3.6. We present the fitting parameters for the FP in Fig. 3.6. A selection of parameters reported in the literature is also presented with dashed lines. As seen in Fig. 3.6, in our sample the black hole mass decreases with increasing radio luminosity. This is opposite to what is found in other studies and could be responsible for the significant difference between this work and other studies for the obtained value of ξ_M. On the other hand, galaxies with H_2O megamaser disks may not follow the well-known scaling relation between the BH mass and the stellar dispersion velocity of the galaxies. They may show an offset with respect to the early-type galaxies, while other spiral galaxies with non-maser dynamically determined BH masses do not show such an offset (Greene et al. 2016), perhaps because the maser disks are preferentially formed in spirals with particularly low mass nuclear sources or because the non-maser dynamical measurements are missing the low mass end of the BH distribution due to their too small spheres of influence. It should be noted that these interpretations are only two of the possible scenarios available.

Radio luminosity versus [OIII] luminosity

Previous studies have shown a strong correlation between the optical narrow emission-line luminosity and the radio luminosity of radio galaxies (e.g., Baum & Heckman 1989; Rawlings & Saunders 1991). This correlation is valid over four to five orders of magnitude for both radio and line luminosities, and could be the result of a common energy source for optical line and radio emissions, suggesting that the luminosity depends on the properties of the central engine. It is also possible that both optical line and radio luminosities depend on a third parameter, e.g., the amount of cold gas present on kpc scales (Baum & Heckman 1989). A correlation was reported by Baum & Heckman (1989) between the Hα+[N II] line luminosity, L_{line}, and total radio luminosity at the VLA scales for a sample of radio galaxies, where L_{line} is proportional to $L_{radio}^{0.73}$. Other studies have compared the radio core luminosity and the luminosities from the narrow line region, where the core is defined as the unresolved component with highest flux density in the radio observations. Buttiglione et al. (2010) reported $L_{[OIII]} \propto L_{core}^{0.75}$ for a sample of high excitation galaxies and Baldi et al. (2018) reported $L_{[OIII]} \propto L_{core}^{0.35\pm0.20}$ for a sample of LINER galaxies. Therefore, we checked for a possible linear correlation between the optical emission-line luminosities and radio luminosities in our sample. We obtained the 5007 Å[OIII] luminosities from NED taken by the SDSS. Four of our five detected sources, Mrk 0001, Mrk 1210, Mrk 1419, and NGC 2273, have [OIII] luminosities. Using a Spearman rank correlation test, we find a correlation between 5 GHz (derived from VLBI) and the [OIII]

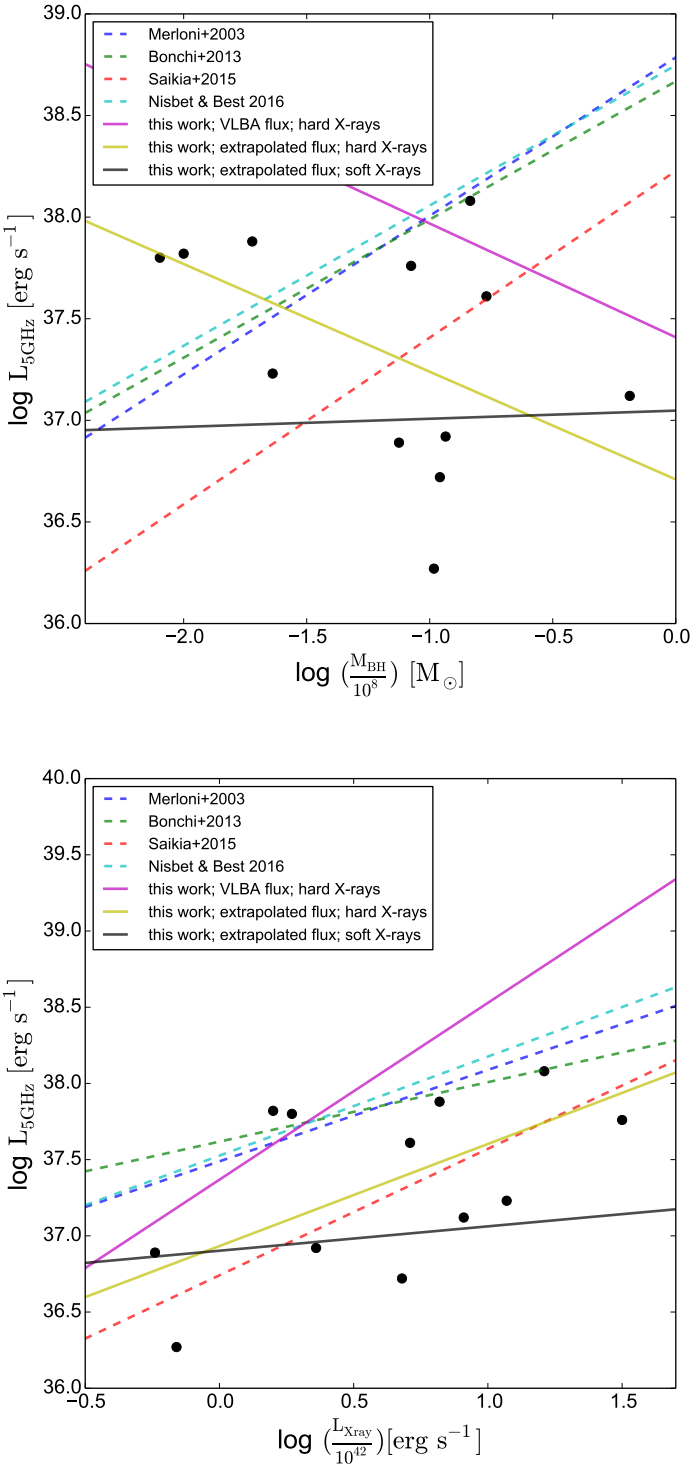

Figure 3.6: Parameters of the fundamental plane of the black hole activity. Top panel: 5 GHz radio luminosity vs. black hole mass. The data points are the extrapolated 5 GHz fluxes obtained from the 33 GHz data (Kamali et al. 2017), using a spectral index of 0.21 (see Sect. 3.5.5). Dashed lines represent $\xi_{\rm M}$ available in the literature (see equation 3.2), assuming a constant X-ray luminosity (mean value of our data) and the solid lines represent $\xi_{\rm M}$ obtained in this work. Lower panel: 5 GHz radio luminosity vs. X-ray luminosity. Dashed lines represent $\xi_{\rm X}$ available in the literature, assuming a constant black hole mass (mean value of our data) and the solid lines represent $\xi_{\rm X}$ obtained in this work.

Table 3.6: Fit parameters of fundamental plane for black hole activity.

ξ_X	ξ_M	b_R	Notes
1.16±1.11	-0.56±0.97	-7.61±45.13	this work, hard X-rays, 5 GHz VLBA fluxes, 5 sources
0.67±0.20	-0.53±0.19	12.27±8.18	this work, hard X-rays, extrapolated 5 GHz fluxes using α=0.21, 12 sources
0.16±3.3	0.04±5.6	30.1±141	this work, soft X-rays, extrapolated 5 GHz fluxes using α=0.21, 5 sources

Notes. Column 1: Coefficient of X-ray luminosity in Eq.3.2. Column 2: Coefficient of SMBH masses in Eq.3.2. Column 3: Intercept of Eq.3.2. Column 4: Notes. Extrapolated 5 GHz fluxes are obtained using spectral index 0.21 between 33 GHz VLA observation and 5 GHz VLBA observations assuming a power-law dependence of $S \propto \nu^{-\alpha}$.

luminosities, $L_{[OIII]} \propto L_{5\,GHz}^{0.87\pm0.09}$. The correlation coefficient is 0.80, and the P-value, indicating that the likelihood that parameters are unrelated, is 0.2 (see Fig. 3.7). While this suggests reasonable agreement with previously mentioned studies, we note that the result is based on very few sources. We also note that the correlation of radio luminosity with emission-line luminosity extends over five orders of magnitude in L_{radio} and four orders of magnitude in L_{line}, i.e., there is ~ one order of magnitude scatter in the radio luminosity for a given line luminosity, suggesting that other criteria such as environment or different accretion modes play a role in determining the radio and optical emission-line luminosities of these galaxies (Baum & Heckman 1989).

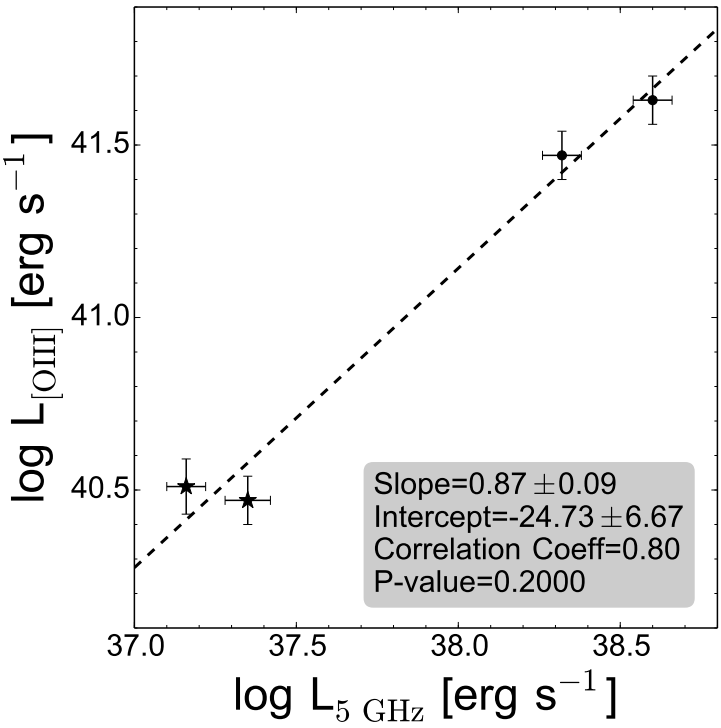

Figure 3.7: 5007 Å [OIII] vs. 5 GHz luminosity. The slope and the intercept of the fitted line, correlation coefficient, and the P-value of the rank correlation test are shown in the plot. The clean maser disks are shown as stars and the non-clean disks as dots.

Radio luminosity versus maser disk radius

In our pilot project (Kamali et al. 2017) we demonstrated a correlation between the disk's inner and outer radii and the 33 GHz radio luminosity of galaxies with H_2O masers in their nuclear disks (i.e., both inner and outer radii of the disk increase as the radio luminosity increases). In this work, we find a similar correlation for inner and outer disk radius versus the 5 GHz luminosities (Fig. 3.8). Correlations between the maser disk size and luminosity at other frequencies were investigated previously. For example, Gao et al. (2017) reported a correlation between the infrared (IR) luminosity and the maser disk's outer radius. This correlation exists because the gas temperature should be higher than the minimum kinetic temperature of ~ 400 K for masing to occur. The H_2O molecules are mixed with dust and the dust temperature depends

on the bolometric luminosity. Therefore, the outer radius of the maser disk also depends on the bolometric luminosity of the AGN. In Sect. 3.5.5 we showed a correlation between the 5 GHz luminosity and the [OIII] luminosity (which is a proxy for the AGN's bolometric luminosity; e.g., Bassani et al. 1999; Heckman et al. 2005). Thus, a correlation between the outer radius of the maser disk and 5 GHz luminosities is expected. Furthermore, the pressure outside the outer disk is lower than the critical pressure, which permits the molecules to exist (Neufeld et al. 1994), and this critical pressure depends on the X-ray luminosity (for a detailed analysis, see Neufeld & Maloney 1995). Although a correlation between the X-ray luminosity and the maser disk size is expected, former studies did not find such a correlation (Kamali et al. 2017). High energy electrons are responsible for both synchrotron radio emission and the synchrotron self-Compton X-ray radiation (Falcke & Biermann 1995). However, our sources are Compton thick and an incorrect estimate of the column densities can affect the estimation of the intrinsic unobscured X-ray luminosities. Radio emission does not suffer from extinction and might be a better tool for estimating the impact of these high energy electrons that are confining the disk.

3.6 Summary

We observed a sample of 18 LLAGNs with the VLBA at C band (6 cm) and detected five sources: Mrk 0001, Mrk 1210, Mrk 1419, NGC 2273, and UGC 3193. We measured the orientations of the putative jets with respect to those of the maser disks. The maser disk orientation is known for all the detected sources, except for UGC 3193. All four sources have jet directions that are misaligned with the disk's normal by < 0.6 radian. For the null hypothesis that the jets have random distribution in space, the probability that all four sources have a misalignment of less than 0.6 radian is 0.009, indicating that the jet orientations are not random. The PA differences seem to be related to the disk size: the larger the disk size, the more aligned the radio continuum is to the disk's normal. A tight correlation with correlation coefficient of 0.87 is observed between the 5007 Å[OIII] line luminosity and the 5 GHz radio continuum luminosity. The disk's inner and outer radii show a linear correlation with the 5 GHz continuum luminosity: the larger the inner radius of the maser disk, the brighter the central region of the galaxy at 5 GHz. We note, however, that all these results are based on a very small sample of sources. Further observations and maps of maser disks and of the nuclear regions of maser host galaxies will provide a larger sample for a more detailed investigation on the alignment of the accretion disk and jets in the galaxies where both phenomena are directly observable.

Acknowledgments

F.K. would like to thank the anonymous referee for the critical and constructive feedback. F.K. is also grateful to Gisela Noemi Ortiz-Leon for her constructive comments and discussions on the data reduction process. This work made use of the NASA/IPAC extragalactic Database (NED), which is operated by the Jet Propulsion Laboratory, California Institute of Technology, under contract with NASA. We further acknowledge the use of the Kapteyn Package (Terlouw & Vogelaar 2015), the HyperLeda database (http://leda.univ-lyon1.fr), and the SAO/NASA ADS Astronomy Abstract Service (http://adsabs.harvard.edu) and the National Radio Astronomy Observatory, which is a facility of the National Science Foundation operated under cooperative agreement by Associated Universities, Inc.

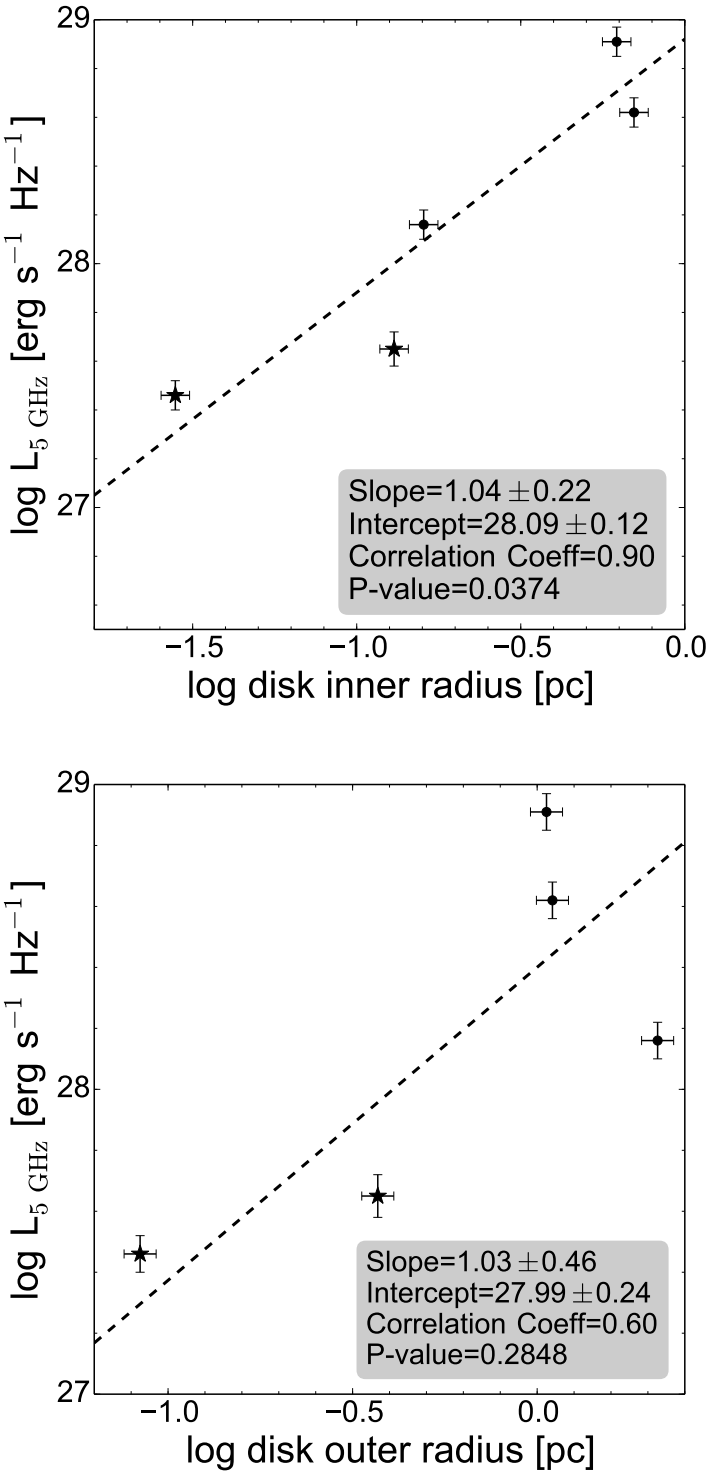

Figure 3.8: 5 GHz luminosities vs. the inner radius (upper panel) and the outer radius (lower panel) of the maser disk. The slope and the intercept of the fitted line, correlation coefficient, and the P-value of the rank correlation test are shown in the plot. The clean maser disks are shown as stars and the non-clean disks as dots.

3.7 Appendix: Probability distribution of the observed PA offsets

Detectable maser disks are edge-on so their normal lies in the plane of the sky. For the null hypothesis that jets have an isotropic distribution of orientations in space (i.e., they are not linked with the maser disk's rotation axis), what is the probability distribution $\rho(\delta)$ of the observed (projected onto the sky) PA offsets δ where $0 < \delta < \pi/2$? Let ϕ be the magnitude of the polar angle between the jet and the normal to the disk. Let θ be the azimuth angle in the disk plane, where θ=0 corresponds to the line from the disk center pointing away from the observer. Thus, $\delta = \phi \sin(\theta)$. The differential probability of observing δ for a given ϕ is

$$p_\delta(\delta|\phi)\, d\delta = p_\delta(\delta|\phi)\, \phi\, d sin(\theta) = p_\theta(\theta)\, d\theta = \frac{2\, d\theta}{\pi}, \tag{3.3}$$

so

$$p_\delta(\delta|\phi) = \frac{2\, d\theta}{\pi\, \phi\, d sin\theta} = \frac{2}{\pi\, \phi\, cos\theta} = \frac{2}{\pi\, \phi\, (1 - sin^2\theta)^{1/2}} = \frac{2}{\pi(\phi^2 - \delta^2)^{1/2}} \quad (\delta \leq \phi) \tag{3.4}$$

For an isotropic distribution of jets, the probability distribution of polar angles ϕ is $p_\phi(\phi)d\phi = sin\,\phi\, d\phi$.

The differential probability distribution of δ for all jets is obtained by integrating over ϕ.

$$p(\delta) = \int_\delta^{\pi/2} p_\delta(\delta|\phi)\, p_\phi(\phi) d\phi. \tag{3.5}$$

Thus, the differential distribution is

$$p(\delta) = \frac{2}{\pi} \int_\delta^{\pi/2} p_\delta \frac{sin\,\phi\, d\phi}{(\phi^2 - \delta^2)^{1/2}} \tag{3.6}$$

and the corresponding cumulative distribution is

$$P(< \delta) = \int_0^\delta p(\acute{\delta})\, d\acute{\delta}. \tag{3.7}$$

Both $p(\delta)$ and $P(< \delta)$ are plotted in Fig. 3.9.

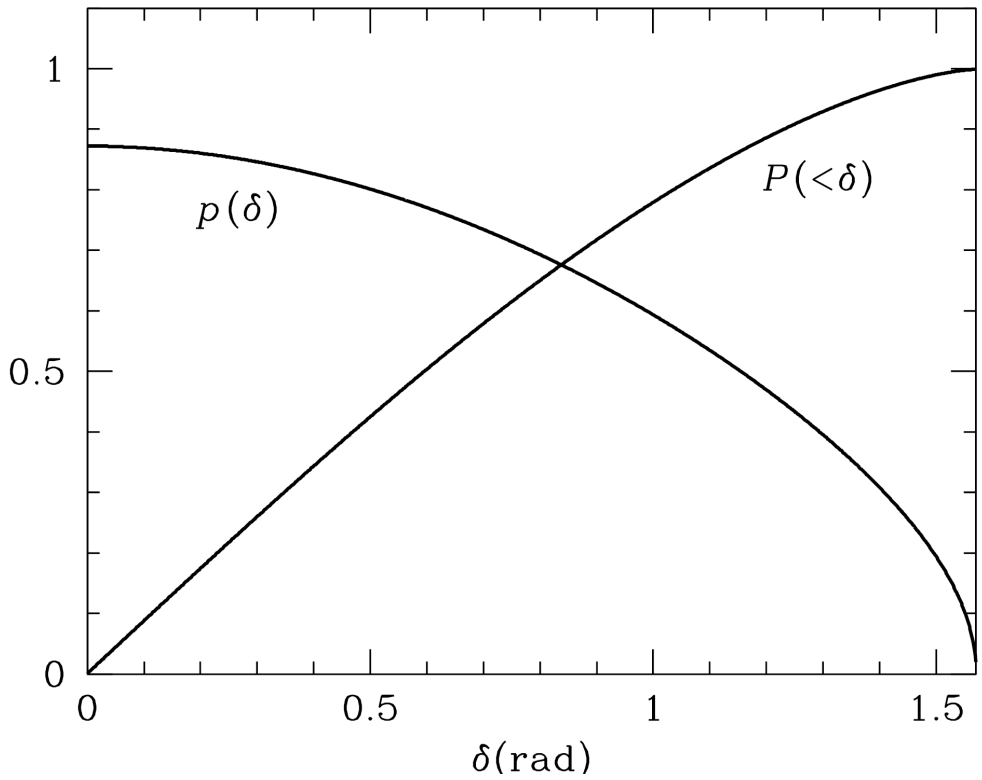

Figure 3.9: Differential probability distribution $p(\delta)$ of the PA difference δ between the disk normal and isotropic radio jets for edge-on maser disks and the cumulative distribution $P(<\delta)$ of PA differences smaller than δ.

CHAPTER 4

The nature of radio emission in H_2O-megamaser galaxies

This chapter is work in progress, planned to be submitted to the A&A journal.

Abstract

We present C-band (5.1 GHz) radio observations of a sample of 18 low luminosity active galactic nuclei obtained using the enhanced Multi-Element Radio Linked Interferometer Network with 45 to 120 milliarcsecond resolution. We aim to investigate the alignment of the kpc-scale jets with the rotation axis of the maser disks orbiting the suppermassive black holes at the centers of these sources. Furthermore we would like to find out what caused the low detection rate of the higher resolution observations of the same sample with the Very Long Baseline Array (see Chapter 3). We also study the origin of radio emission from H_2O-megamaser galaxies, using spectral indices, brightness temperatures, and multi-scale radio morphologies. Ten out of the 18 sources are detected at 4σ or higher levels. Four galaxies among those with known maser disk orientation exhibit radio emission misaligned up to 37° of the maser disk's rotation axis. We conclude that in the majority of the sources in our sample the radio emission is possibly contaminated by a contribution from star formation, partially in the form of free-free radiation. Besides fast jets, outflows are also another dominant source of radio emission in our sample.

4.1 Introduction

Radio emission from active galactic nuclei (AGNs) originates from different physical mechanisms such as star-formation (SF), coronal activity around and accretion of material onto the central supermassive black hole (SMBH) and its associated outflows, and the interaction of jets with the surrounding interstellar and intergalactic medium (Panessa et al. 2019). Despite observational diagnostics such as radio morphologies, radio power and spectral indices, it is not an easy task to disentangle these processes since degeneracies are common among the diagnostics. Probing these different physical mechanisms is not straightforward in radio-loud AGNs due to the dominance of radio synchrotron emission from the jet. On the other hand, radio quiet AGNs are better laboratories to investigate the nature of radio emission from the nuclei themselves, since they lack the strong radio emission from the jet, while a jet might still be present.

The main contribution to the radio synchrotron emission related to AGNs comes form jets. Flat or slightly inverted spectral indices from a compact source which is unresolved on parsec

scales, could be associated with the jet base (also called core, Blandford & Königl 1979). Jet bases typically have high brightness temperatures resulting from non-thermal processes related to relativistic electrons (Blundell & Beasley 1998). For example, low-ionization nuclear emission-line regions (LINERs) usually show core-brightened radio jets (Capetti et al. 2017) and most Seyfert galaxies exhibit high brightness temperature ($\gtrsim 10^7$ K) compact sub-pc scale nuclear emission (Middelberg et al. 2004; Kamali et al. 2017, 2019).

Other contributions to the synchrotron emission on kpc-scales arise from outflows associated with diffuse radio emission. Winds (typically defined as uncollimated outflows) are observed on different physical scales in AGNs (e.g., Laor & Brandt 2002; Zakamska & Greene 2014). Wind shocks could accelerate the relativistic electrons and produce synchrotron emission on kpc-scale. This will result in low brightness temperatures below 10^5K.

Putative accretion disk corona is another contributor to the radio emission, also via synchrotron emission. The emission from the corona originates from a milli-pc region close to the SMBH and therefore is unresolved by most contemporary instruments (Panessa et al. 2019).

The presence of an AGN may also be connected to vigorous SF in the nuclear environments. SF contributes extensively to both thermal and non-thermal radio emission in galaxies with radio quiet AGNs. The magnetic field of the supernova remnant accelerates the relativistic electrons (Condon 1992), and the resulting radio emission appears typically as diffuse or clumpy extended emission in radio images.

The radio emission from an optically thin plasma in the disk winds could also contribute to observed radio emission via the bremsstrahlung process (Blundell & Kuncic 2007). Supernovae in star forming regions can also account for some of the extended radio structure in Seyferts and starburst galaxies (see e.g., Panessa et al. 2019, and references there in).

All the above mentioned different physical mechanisms contribute to what we observe in the radio regime. With the help of our observations made at different resolutions, here we attempt to find the dominant source of radio emission for each source of our sample. It should be noted that the observations presented in this chapter, were initially carried out to search for the cause of the low detection rate of our observations conducted using the Very Long Baseline Array (VLBA), published in Kamali et al. (2019, Chapter 3). We discussed the 33 GHz observations which were carried out using the Very Large Array (VLA) in Kamali et al. (2017, Chapter 2). Radio emission was detected in 21 out of 24 galaxies in our sample on kpc-scales. Later in chapter 3 we discussed the high resolution observations of a selected sub-sample of galaxies previously detected in our VLA data, using the VLBA this time at 5 GHz. Only five out of 14 galaxies were detected with the VLBA on pc-scales. We speculated that this low detection rate at high resolution could be due to the fact that the emission is resolved out in the VLBA observations. Therefore we observed our sample with another radio interferometer array which has an intermediate resolution between that of the VLBA and the VLA. This array, called enhanced Multi-Element Radio Linked Interferometer Network (eMERLIN, see Sect. 1.7), consists of seven antennas with a maximum baseline of $\sim$ 217 km and a resolution of $\sim$ 40 mas.

In this chapter, we briefly review the emission mechanisms relevant to the scales we probe, and try to identify the dominant source of radio emission in our studied sample. We also use correlation analysis to identify or rule-out the possible source of radio emission.

4.2 Sample

The sample studied here consists of 18 low luminosity active galactic nuclei (LLAGNs) with declinations > -5, selected from a sample of H_2O -megamaser galaxies obtained by the Megamaser Cosmology Project (MCP, e.g., Reid et al. 2009; Braatz et al. 2010; Gao et al. 2017).

From these 18 LLAGNs, 14 sources were observed in the course of our previous VLA pilot project at 33 GHz. Out of these, five sources are also detected in the 5 GHz VLBA observations (see Chapters 2 and 3). In our sample, 12 sources are clean maser disks, where clean refers to the level of certainty in our knowledge about the origin of the maser emission. In clean maser disks, the maser emission from the disk dominates over maser emission from the jets or outflows (Pesce et al. 2015, see Sect. 3.2 for more details). On the other hand, the origin of the non-clean maser disks is not clear. The emission might arise from maser disks or from outflows or star forming regions. As already mentioned, in our sample 12 sources are clean disks while the nature of the other six maser sources remain unclear. The clean masers are shown in bold face in all the tables, and are mentioned again if required in the discussion. We adopted distances from NED, using H_0=70.0 km s^{-1} Mpc^{-1}, Ω_{matter}=0.27 and Ω_{vacuum}=0.73 as the cosmological parameters.

4.3 Observations and data reduction

The observations were carried out in C-band (4.82-5.33 GHz) between September 2017 and July 2018. The Lovell telescope was not operating at the time of our observations, therefore the interferometer consisted of six antennas. We used a total bandwidth of 512 MHz (4 spectral windows of 128 MHz width each), dual polarization, and a total time of ~ 1.5 to 11 hour per target, different for each source. The synthesized beam width ranges from 45 to 120 milliarcsecons (mas). A scan of bandpass calibration was placed at the start of the observations followed by alternating observations of phase calibrators and the actual megamaser targets. A flux calibration scan and another bandpass calibration scan were placed at the end of the observations. Table 4.1 lists the sources, their pointing coordinates and their associated calibrators. The data were calibrated using the eMERLIN calibration pipeline[1]. The pipeline follows standard calibration steps, including flagging radio interference, antenna slewing and edge channels, bandpass, phase, and amplitude calibrations. The resulting calibration weblogs were checked for any failures and if needed, additional flagging was applied. After the initial calibrations, for sources with sufficient signal-to-noise ratio (S/N), self calibration of both phases and amplitudes (or only phases) was carried out to improve the quality of our images. All images are constructed using the Common Astronomy Software Applications (CASA) package (McMullin et al. 2007), using the CLEAN algorithm with robust parameter of 0.5.

4.4 Results

The sample targeted in this work was previously observed with the VLBA also in C-band (Kamali et al. 2019). While only 28% of the sources (five out of 18) were detected with the VLBA, in this work ~ 56% of the sample are detected with S/N greater than 4 σ. This includes ten out of 18 sources: Mrk 0001, Mrk 0078, Mrk 1210, Mrk 1419, NGC 0591, NGC 1194, NGC 2273, NGC 4388, UGC 3193 and UGC 9639. From these ten detected sources, all sources except UGC 9639 were also detected with our lower angular resolution 33 GHz VLA observations. Among them are five sources also detected with higher angular resolution in the 5 GHz VLBA observations (Mrk 0001, Mrk 1210, Mrk 1419, NGC 2273 and UGC 3193, see Chapter 3). The eMERLIN observations aim to investigate whether the high resolution of the VLBA observations resulted in resolving out the extended emission in the undetected sources.

[1] http://www.e-merlin.ac.uk/tools/eMCP-2.pdf

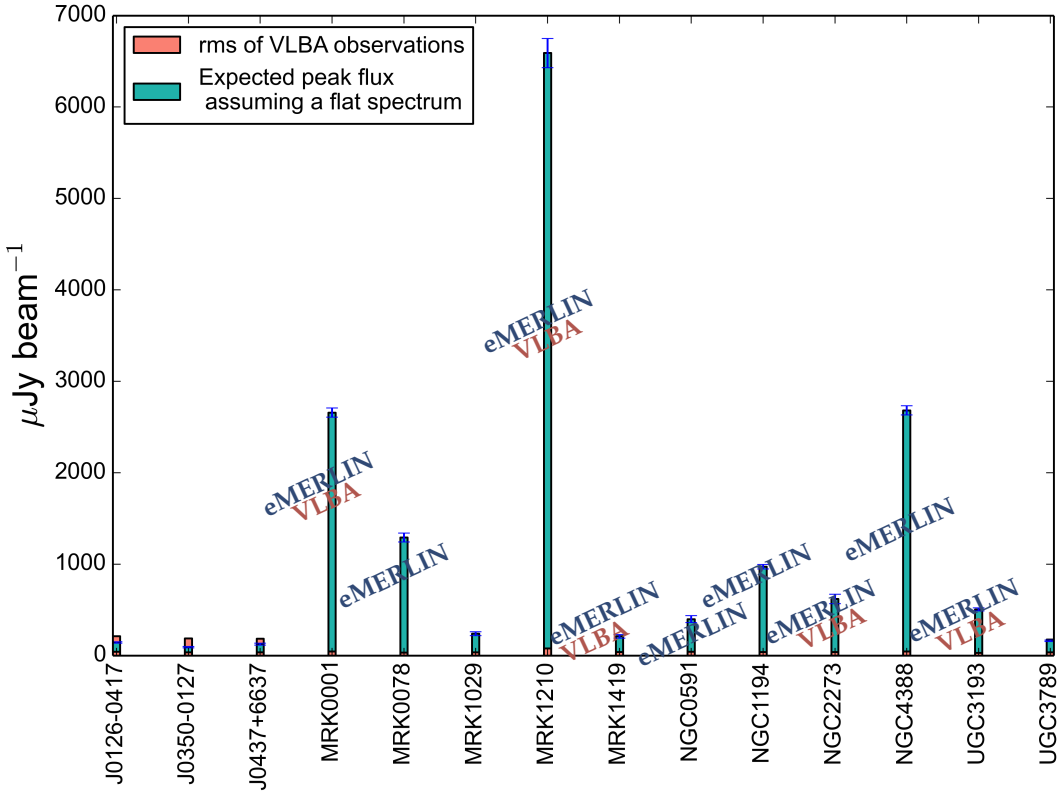

Figure 4.1: Expected flux densities at 5 GHz obtained from the 33 GHz VLA observations, assuming a spectral slope of zero. The noise levels of the VLBA observations are also shown (see Chapter 3). The five detected sources with the VLBA and nine detected sources with the eMERLIN are labeled. One source (UGC 9639) is not presented here. This source was not observed in our pilot project, therefore its expected peak flux density is not listed here.

As shown in Fig. 4.1, the five detections not seen in our VLBA data are among the brightest sources in the VLA observations.

For detected sources, two-dimensional Gaussians were fitted to the individual components using task IMFIT in CASA. If the source structure is more complex, multiple Gaussians were fitted over emission greater than $4\,\sigma$. The resulting peak flux densities and integrated flux densities are reported in Table 4.2. Figures 4.2 to 4.12 present the radio continuum maps of the detected sources. If available, the maser disk's orientation and position are also presented in the maps. Of the ten detected sources, seven possess a clean maser disk (see Sect. 4.2).

4.5 Discussion

4.5.1 Spectral indices and brightness temperatures

Spectral indices were obtained using broad (512 MHz) bandwidth data of our observations. The spectral index maps are created by CASA with the number of Taylor coefficients set to 2 in the imaging procedure using the task tCLEAN. However due to insufficient S/N and bandwidth, the obtained $\alpha_{4.9}^{5.3}$ indices (reported in Table 4.2) have high uncertainties. We also estimated the spectral indices between 33 GHz and 5 GHz, α_{5}^{33}, assuming a power-law dependence for the

Table 4.1: eMERLIN observations.

Galaxy	Right Ascension/ Declination *J*2000	Phase Calibrator	Bandpass Calibrator	Flux Calibrator	Pointing Calibrator
Mrk 0001/NGC 0449	$01^h16^m07^s.209/+33°05'21.''634$	0112+3522	1407+0284	1331+0305	0319+0415
J0126-0417	$01^h26^m01^s.66/-04°17'56.''2$	0138-0540	1407+0284	1331+0305	0319+0415
NGC 0591/Mrk 1157	$01^h33^m31^s.27/+35°40'05.''7$	0152+3716	1407+0284	1331+0305	0319+0415
Mrk 1029	$02^h17^m03^s.57/+05°17'31.''4$	0224+0659	1407+0284	1331+0305	0319+0415
NGC 1194	$03^h03^m49^s.11/-01°06'13.''5$	0259-0019	1407+0284	1331+0305	0319+0415
J0350-0127	$03^h50^m00^s.35/-01°27'57.''7$	0339-0146	1407+0284	1331+0305	0319+0415
J0437+6637	$04^h37^m08^s.26/+66°37'42.''3$	0449+6332	1407+0284	1331+0305	0319+0415
UGC 3193	$04^h52^m52^s.5569/+03°03'25.''768$	0453+0128	1407+0284	1331+0305	0319+0415
NGC 2273	$06^h50^m08^s.6577/+60°50'44.''9012$	0638+5933	1407+0284	1331+0305	0319+0415
UGC 3789	$07^h19^m30^s.92/+59°21'18.''4$	0707+6110	1407+0284, 1459+4442	1331+0305	0319+0415
Mrk 0078	$07^h42^m41^s.73/+65°10'37.''5$	0756+6347	1407+0284, 1459+4442	1331+0305	0319+0415
Mrk 1210/Phoenix	$08^h04^m05^s.8570/+05°06'49.''846$	0803+0421	1407+0284, 0319+0415	1331+0305	0319+0415
Mrk 1419/NGC 2960	$09^h40^m36^s.3835/+03°34'37.''289$	0938+0314	1407+0284	1331+0305	0319+0415
NGC 4388	$12^h25^m46^s.75/+12°39'43.''5$	1225+1253	1407+0284	1331+0305	0319+0415
NGC5765b	$14^h50^m51^s.5/+05°06'52.''0$	1458+0416	1407+0284	1331+0305	0319+0415
UGC 9639/Mrk 0834	$14^h58^m35^s.99/+44°53'01.''0$	1459+4442	1407+0284, 1459+4442	1331+0305	0319+0415
NGC 6264	$16^h57^m16^s.13/+27°50'58.''5$	1659+2629	1407+0284, 1459+4442	1331+0305	0319+0415
NGC 6323	$17^h13^m18^s.07/+43°46'56.''8$	1707+4536	1407+0284, 1459+4442	1331+0305	0319+0415

Notes. Column 1: name of galaxy. The sources in bold hold clean maser disks (see Sect. 3.2). Column 2: *J*2000 right ascension and declination. For Mrk 0001, NGC 2273, UGC 3193, Mrk 1210 and Mrk 1419 the coordinates are from Kamali et al. (2019), for NGC 5765b, NGC 6323, NGC 6264 and UGC 9639 the coordinates are taken from NED and for the remaining sources the coordinates are from Kamali et al. (2017). Column 3: Phase calibrator. Column 4: Bandpass calibrators. Column 5: Flux calibrator. Column 6: Pointing calibrator.

continuum flux density given by $S \propto \nu^{-\alpha}$, where in 5 GHz observations the beam linear sizes are approximately five times smaller than the 33 GHz beam sizes. These spectral indices are also listed in Table 4.2. The brightness temperatures (T_B) were obtained using

$$T_B = \frac{2\,ln(2)}{k_B\,\pi}\frac{\lambda^2\,S_{tot}}{\theta_{maj}\,\theta_{min}}, \tag{4.1}$$

where k_B is the Boltzmann constant, S_{tot} is the total flux density, λ is the observed wavelength, and θ_{maj} and θ_{min} are the deconvolved sizes of the major and the minor axes of the source. In case the component is unresolved, the beam size is used as an upper-limit for the source size, resulting in a lower limit for T_B. The obtained brightness temperatures are listed in Table 4.2.

4.5.2 The nature of the radio emission in H_2O -megamaser galaxies

This section is based on an observational diagnostic method presented in Panessa et al. (2019). Using this method, based on the morphologies, brightness temperatures, spectral indices, and correlation analysis, we attempt to find the dominant source of radio emission in our sample. If the radio source is resolved at arcsec resolution and possesses a steep spectrum ($\alpha > 0.5$ for $S \propto \nu^{-\alpha}$), we tentatively can distinguish between SF and outflows by the difference in their morphologies. Radio emission originating from SF appears as clumpy or diffuse, while the radio emission from an outflow has a biconical shape (Panessa et al. 2019). If the radio emission is resolved on kpc (arcsec) scale but the spectral index is inverted and the brightness temperatures are smaller than $\sim 10^5$K, free-free emission could be the potential source of radio emission. In the case of a resolved radio source at arcsec resolution with a flat spectrum, the nature of the radio emission remains unknown.

On the other hand, if the radio emission is not resolved at arcsec resolution, observations with higher resolution (mas-scale) are required to further investigate the origin of the emission. A resolved mas-scale radio source is possibly representing jets, while an unresolved radio source with a flat spectrum possibly originates from the accretion disk's corona or jet base. An unresolved radio source on mas scale possessing a steep spectrum is presumably an outflow or caused by mass ejection from the corona. Another observational diagnostic for investigating the origin of the radio emission are the observed correlations between the radio luminosities and the far-infrared (FIR) or the X-ray luminosities. The FIR-radio luminosity correlation, typically applying for star-forming galaxies, has been found also in Seyfert galaxies and low redshift radio quiet quasars (Sopp & Alexander 1991; Sargent et al. 2010). A correlation between the X-ray and radio luminosities has been observed in X-ray binaries in their low-accretion rate hard state (Fender et al. 2004). Using the assumption that the underlying jet physics is scale invariant (i.e., the jets from stellar mass black holes and those from the SMBHs follow the same basic physical laws, see Merloni et al. 2003, and references therein), if the radio emission is dominated by synchrotron emission from the jet, we expect to see a correlation between the X-ray and radio luminosities (Corbel et al. 2013).

Here we discuss the above mentioned characteristics for the individual sources, followed by a summary at the end of this section.

– Mrk 0001

In Chapters 2 and 3 we presented the 33 GHz VLA and 5 GHz VLBA radio observations of Mrk 0001, respectively. In both maps we see extended emission along a northwest-southeast direction, similar to what we observe in the eMERLIN map presented in Fig. 4.2. The radio emission is resolved on arcsec resolution with both the VLA and eMERLIN. The spectral index,

Table 4.2: Obtained properties from eMERLIN data.

Galaxy		**Peak flux**	**Integrated flux**	T_B	**Spectral index**	**Spectral index**
		mJy	**mJy**	K	$\alpha_{4.9}^{5.3}$	α_{5}^{33}
Mrk 0001	tot	—	21.23 ± 0.73	—	—	0.89±0.02
	C1	0.42 ± 0.10	0.89 ± 0.33	$>5.0 \times 10^3$	0.69 ± 1.6	—
	C2	6.78 ± 0.12	10.43 ± 0.30	$(4.4 \pm 1.8) \times 10^5$	—	—
	C3	2.32 ± 0.12	8.75 ± 0.58	$(6.8 \pm 2.8) \times 10^4$	—	—
	C4	0.64 ± 0.03	1.16 ± 0.08	$(2.0 \pm 0.5 \times 10^4$	1.5 ±1.9	—
Mrk 0078	tot	3.66 ± 0.12	5.17 ± 0.25	$(4.2 \pm 1.2) \times 10^4$	-0.95 ± 3.9	0.57±0.04
Mrk 1210	tot	—	44.11 ± 0.96	—	—	0.81±0.01
	C1	6.22 ± 0.23	8.49 ± 0.60	$(3.6 \pm 6.0) \times 10^6$	-1.4 ± 5.7	—
	C2	20.03 ± 0.26	35.62 ± 0.75	$(0.9 \pm 1.2) \times 10^6$	-0.06 ± 5.9	—
Mrk 1419		0.40 ± 0.02	0.61 ± 0.06	$>5.6 \times 10^3$	1.8 ± 1.2	0.35±0.09
NGC 0591	tot	—	6.99 ± 0.38	—	—	0.81±0.04
	CN1	0.27 ± 0.03	0.38 ± 0.07	$(1.2 \pm 1.5) \times 10^4$	-3.7 ± 1.8	
	CN2	0.54 ± 0.03	0.83 ± 0.07	$(1.1 \pm 0.4) \times 10^4$	1.9 ± 1.5	CN = 0.89±0.07
	CN3	0.57 ± 0.06	2.31 ± 0.32	$(6.2 \pm 2.6) \times 10^3$	2.7 ± 1.3	
	CS1	1.25 ± 0.03	1.61 ± 0.09	$(4.0 \pm 1.0) \times 10^4$	-2.9 ± 2.0	
	CS2	0.40 ± 0.04	1.03 ± 0.15	$(5.5 \pm 3.3) \times 10^3$	-3.1 ± 4.9	CS = 0.74±0.05
	CS3	0.28 ± 0.01	0.44 ± 0.03	$(5.6 \pm 1.1) \times 10^3$	1.9 ± 10.9	
	CS4	0.30 ± 0.01	0.39 ± 0.03	$> 2.0 \times 10^3$	-1.2 ± 2.7	
NGC 1194		0.53 ± 0.02	0.56 ± 0.04	$>6.3 \times 10^3$	8.28 ±10.5	-0.35±0.05
NGC 2273	tot	—	8.74 ± 0.52	—	—	0.62±0.07
	C1	4.76 ± 0.20	6.94 ± 0.44	$(1.2 \pm 0.5) \times 10^5$	4.8 ± 3.5	—
	C2	0.45 ± 0.55	1.80 ± 0.27	$(4.6 \pm 1.5) \times 10^3$	6.8 ± 8.3	—
NGC 4388	tot	—	5.31 ± 0.35	—	—	-0.25±0.04
	CN1	1.26 ± 0.02	1.77 ± 0.08	$(5.0 \pm 2.1) \times 10^4$	3.1 ± 1.5	0.05±0.03
	CN2	0.15 ± 0.01	3.54 ± 0.34	$(1.6 \pm 0.3) \times 10^3$	-3.2 ± 6.7	0.86±0.13
UGC 3193		1.48 ± 0.11	1.91 ± 0.22	$> 5.8 \times 10^3$	-0.03 ± 7.05	0.33±0.05
UGC 9639	tot	—	1.56 ± 0.09	—	—	—
	CN1	0.24 ± 0.01	0.33 ± 0.02	$(2.3 \pm 0.6) \times 10^4$	0.06 ± 0.57	—
	CN2	0.20 ± 0.02	0.43 ± 0.07	$(1.1 \pm 0.7) \times 10^4$	24.6 ± 25.8	—
	CS1	0.26 ± 0.01	0.37 ± 0.03	$(3.2 \pm 1.6) \times 10^4$	-21.5 ± 1.5	—
	CS2	0.17 ± 0.01	0.42 ± 0.05	$(7.4 \pm 1.8) \times 10^3$	-15.6 ± 8.2	—

Notes. Column 1: name of galaxy. The sources in bold have clean maser disks (see Sect. 3.2). Column 2: 5 GHz eMERLIN peak flux density in mJy. Column 3: The Integrated flux density in mJy. Column 4: Brightness temperature in K. If the source is unresolved, a lower limit is given (see Sect. 4.5.1). For sources with multi-component Gaussian fitting, the highest brightness temperature is given. Column 5: Spectral index obtained from the 512 MHz bandwidth eMERLIN observations, assuming a power-law dependence for the continuum flux density given by $S \propto \nu^{-\alpha}$. Column 6: Spectral index obtained from 5 GHz eMERLIN observations and 33 GHz VLA observations, assuming a power-law dependence for the continuum flux density given by $S \propto \nu^{-\alpha}$.

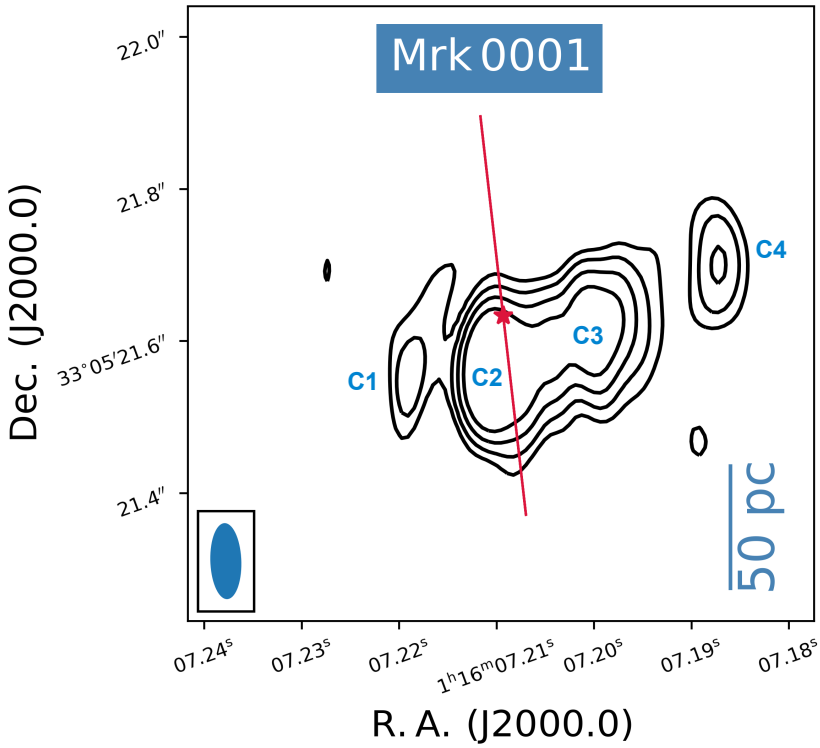

Figure 4.2: Radio continuum map of Mrk 0001, obtained using the eMERLIN array in C-band. The contour levels are ±4, 8, 16 and 32 times the rms noise level of an emission-free region in the CLEANed image (~ 37 μJy/beam). The maser position is shown with a red star, and the maser disk's orientation with a red solid line. The synthesized beam and the physical linear scale are shown in the bottom left and right corner respectively.

α_5^{33}=0.89± 0.02, represents a steep spectral slope; however the diffuse morphology of this galaxy's radio emission in our eMERLIN observations could indicate that the dominant source of radio emission is SF. Nevertheless, we cannot rule out the outflow scenario. If the radio emission extending in the west-east direction (almost perpendicular to the putative maser disk) represents indeed an outflow, then component 2 with the highest brightness temperature, is at the core of this outflow. It should be noted, that the maser has an offset from the center of the radio continuum map here. When over-plotting the maser's position and the radio maps from all three observations (33 GHz VLA, 5 GHz VLBA and eMERLIN), we recognize an offset between the center of all these emissions. Usage of different phase calibrators could partially account for this offset. The nature of the H_2O -megamaser in Mrk 0001 is also mysterious. The systemic masers are not observed in this galaxy. However a fit on the high velocity masers indicates that the putative maser disk has a position angle (PA) of 6.4°±10° (Kuo et al. in. prep.).

– Mrk 0078

Figure 4.3 shows Mrk 0078 which was undetected in our VLBA observations, while it was detected by the VLA at 33 GHz. A single component with an extension in northeast-southwest direction is observed. The radio emission is resolved on arcsec resolution with both VLA

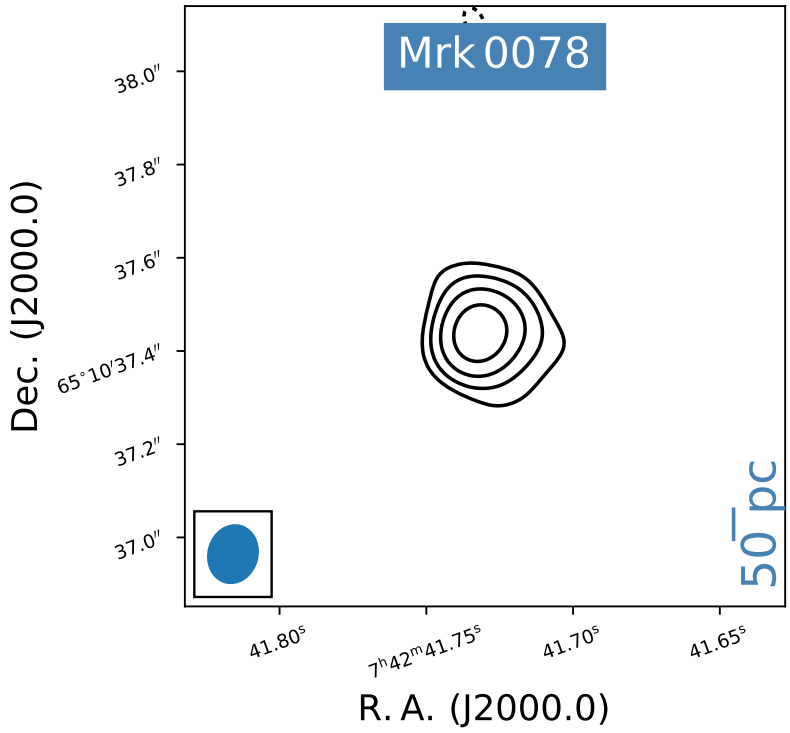

Figure 4.3: Radio continuum map of Mrk 0078, obtained using the eMERLIN array in C-band. The contour levels are ±4, 8, 16 and 32 times the rms noise level of an emission-free region in the CLEANed image (~ 71 μJy/beam). The synthesized beam and the physical linear scale are shown in the bottom left and right corner respectively.

and eMERLIN. The α_5^{33}=0.57± 0.04 spectral index is steep, however the radio morphology is neither biconical nor diffuse or clumpy. The information on the maser disk's properties are also not available yet. Therefore, it is not trivial to draw conclusions about the dominant source of the radio emission in this source.

– Mrk 1210

This galaxy, known as the Phoenix galaxy, shows variability in our radio observations. We have three observations of this source with eMERLIN in C-band, and the integrated flux density of the source has doubled in the second observations which was carried out one day after the first observations. This galaxy is known to be variable also at the X-rays (Masini et al. 2017). The radio emission is resolved on arcsec resolution with both VLA and eMERLIN. The biconical shape seen in Fig. 4.4 (also observed in high resolution VLBA data, see Kamali et al. 2019) and steep spectrum with a slope of α_5^{33}=0.81± 0.02 imply that the main contribution to the radio emission is due to outflows. We identify component 2 (C2) with $T_B = (0.9 \pm 1.2) \times 10^6$ as the core of the outflow. However, in our VLA observation, the morphology is diffuse and clumpy (see Kamali et al. 2017), suggesting that SF is also contributing to the observed radio emission.

– Mrk 1419

The radio emission from this galaxy detected also with the VLA and VLBA, is unresolved in the eMERLIN observations. However, it was resolved with the VLA beam. The maser disk's

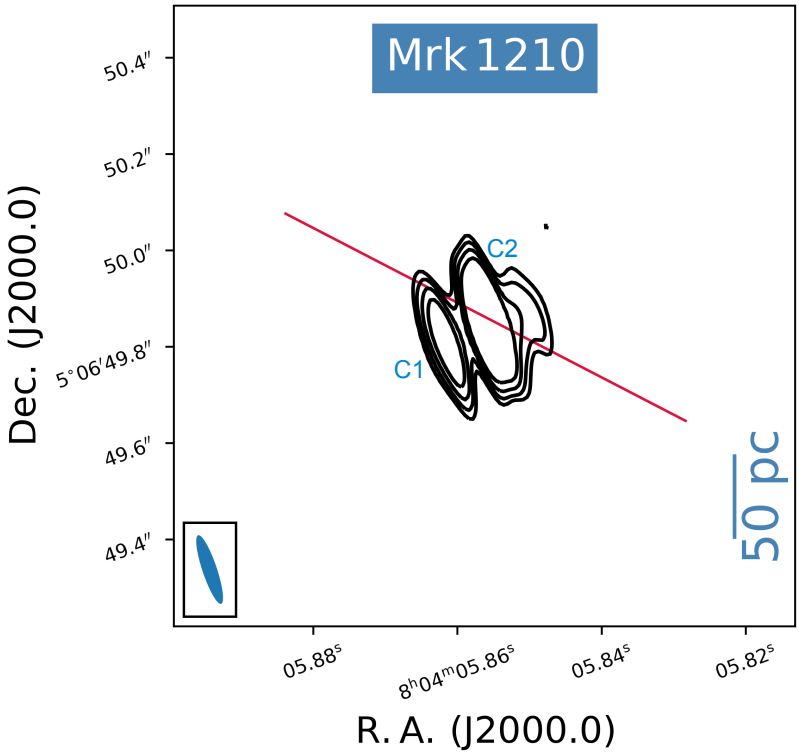

Figure 4.4: Radio continuum map of Mrk 1210, obtained using the eMERLIN array in C-band. The contour levels are ±4, 8, 16 and 32 times the rms noise level of an emission-free region in the CLEANed image (~ 64 μJy/beam). The maser disk's orientation is indicated with a red solid line. The maser disk's position is not available for this source. The synthesized beam and the physical linear scale are shown in the bottom left and right corner respectively.

position coincides with the center of the radio continuum as shown in Fig. 4.5. A flat index, $\alpha_5^{33} = 0.35 \pm 0.09$, and the unresolved mas-scale structure indicates that possibly the radio emission observed here is dominated by the radiation from the jet base or a putative corona.

– NGC 0591

This galaxy was not detected in our VLBA observations. However two components, one in the north and one in the south are detected in our 33 GHz VLA map. Using the higher resolution of eMERLIN, we are able to detect more blobs within the northern and southern components of the VLA image (see Fig. 4.6). The observed biconical shape is an indicator of outflow. Figure 4.7 shows the result of both our VLA and eMERLIN observations. We measured the indices for the northern and southern components separately. The northern component shows a somewhat steeper spectral index ($\alpha_5^{33} = 0.89 \pm 0.07$) compared to the southern one ($\alpha_5^{33} = 0.74 \pm 0.05$), in agreement with the previous spectral indices obtained from the VLA observations (Kamali et al. 2017). Studies of gas kinematics revealed that the Narrow Line Region (NLR) is extended in the northwestern-southeastern direction with a PA of 153° (Riffel & Storchi-Bergmann 2011), where the northeastern component is the blueshifted side. This PA is 11° misaligned with the outflow PA that we obtained here from the eMERLIN observations.

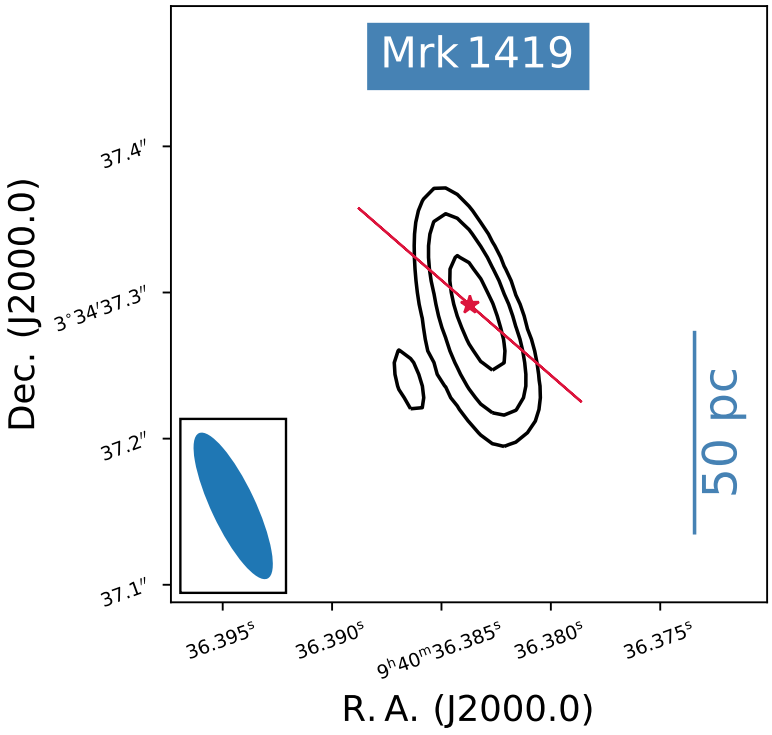

Figure 4.5: Radio continuum map of Mrk 1419, obtained using the eMERLIN array in C-band. The contour levels are ±4, 8, 16 and 32 times the rms noise level of an emission-free region in the CLEANed image (~ 19 μJy/beam). The maser position is shown with a red star, and the maser disk's orientation with a red solid line. The synthesized beam and the physical linear scales are shown in the bottom left and right corner respectively.

– NGC 1194

This source was not detected in our VLBA observations. However, with the intermediate resolution of the eMERLIN, we observe a point source. The maser position for this source coincides with the position of the radio continuum (see Fig. 4.8). This galaxy is resolved in our VLA observations, but unresolved in the eMERLIN observations. The resolved arcsec-scale morphology alongside the inverted spectral index of $\alpha_5^{33} = -0.35 \pm 0.05$ could be a signature of free-free emission. However, that little gas is present on a ~ 50 pc scale in the galaxy (Greene et al. 2014) indicating a small degree of SF, does not fully support the free-free emission scenario. Therefore, we label the origin of radio emission in this galaxy as unknown.

– NGC 2273

As presented in Fig. 4.9, we observe a component that coincides with the maser disk's position and that is also extended in an east-west direction with a PA of 85°. We also observe a blob in the west of the central component at 4 σ. The structure of NGC2273 is resolved in both VLA and eMERLIN observations. A steep spectral index of $\alpha_5^{33} = 0.62 \pm 0.07$ and resolved diffuse structure are indicators of SF activity. We suspect that since extended emission observed

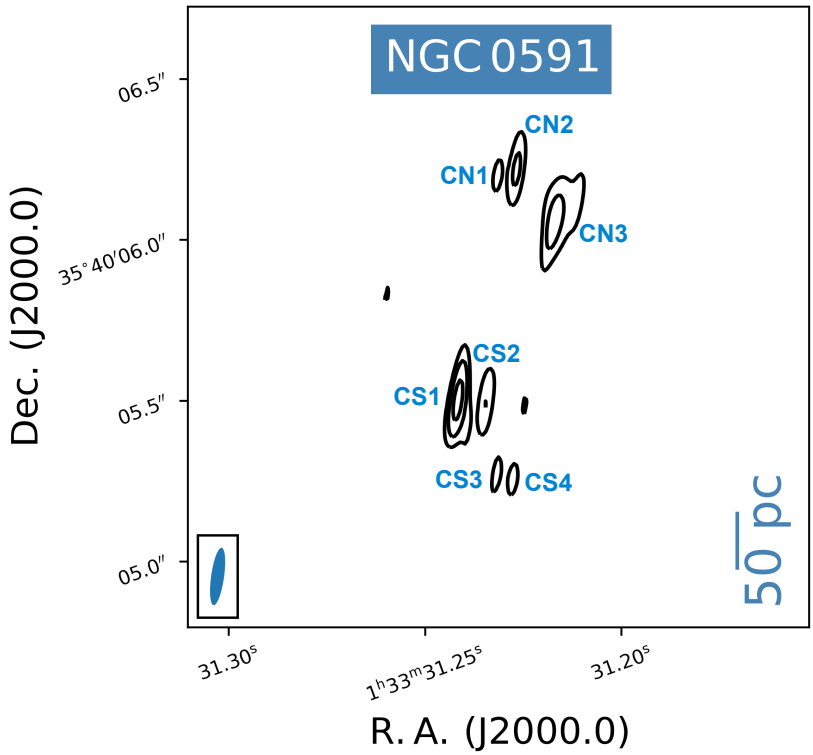

Figure 4.6: Radio continuum map of NGC 0591, obtained using the eMERLIN array in C-band. The contour levels are ±4, 8, 16 and 32 times the rms noise level of an emission-free region in the CLEANed image (~ 61 μJy/beam). The synthesized beam and the physical linear scale are shown in the bottom left and right corner respectively.

with the VLA beam is resolved out with the eMERLIN beam, that the spectral index is slightly underestimated. The morphology in the eMERLIN map (Fig. 4.9) could also support the outflow scenario. Therefore we label the dominant origin of radio emission in this galaxy as a mixture of SF and outflow.

– NGC 4388

NGC 4388 is a member of the Virgo cluster, and was not detected in our VLBA observations. This galaxy is resolved in both VLA and eMERLIN data, showing extended emission in the VLA data, and two components in the eMERLIN data, following a northeast-southwest direction (see Fig. 4.10). The spectral index obtained using the total flux density at 5 GHz and 33 GHz results in $\alpha_5^{33} = -0.25 \pm 0.04$. However, since in the 33 GHz image a large contribution to the total flux density comes from the extended emission in the southwest and this extended emission is resolved out in the eMERLIN data, we conclude that the total α_5^{33} is not reliable. We measured α_5^{33} by integrating the flux densities in the VLA map over the area observed with eMERLIN. The spectral index for the C1 component is $\alpha_5^{33} = 0.05 \pm 0.03$ and for the C2 component $\alpha_5^{33} = 0.86 \pm 0.13$. This is consistent with previous studies that suggest a flat spectrum source at the center of the galaxy, and steep spectrum sources outside of it (Giroletti & Panessa 2009, and references there in). For instance, Falcke et al. (1998) have shown that the northeastern radio source is coincident with the optical nucleus, while the southwestern radio

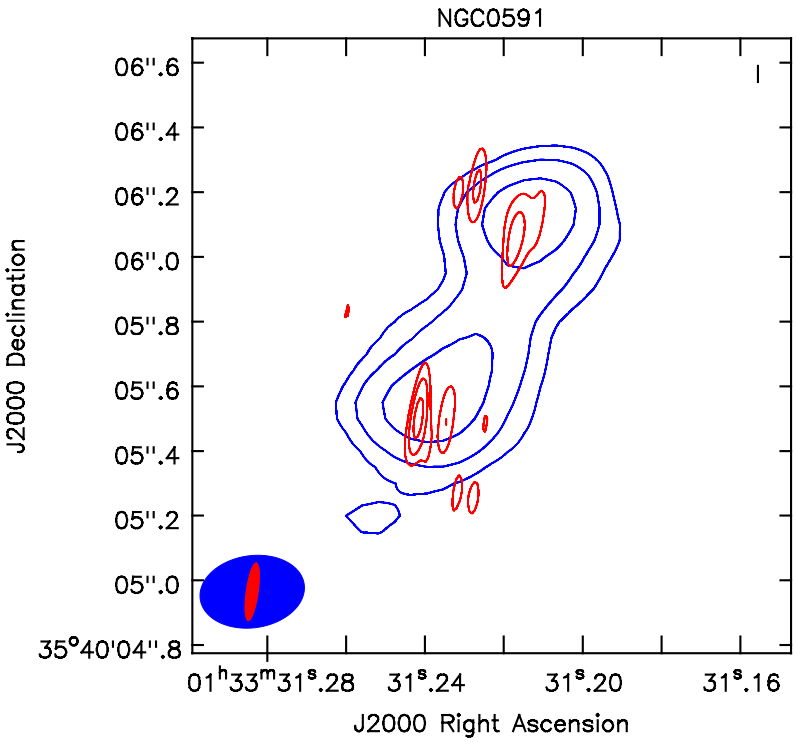

Figure 4.7: Radio continuum map of NGC 0591, obtained using eMERLIN in C-band (red contours) and the VLA in Ka-band (blue contours). The contour levels are ±4, 8, 16 and 32 times the rms noise level of an emission-free region in the CLEANed image (~ 61 μJy/beam for eMERLIN and ~ 13.6 μJy/beam for VLA). The synthesized beam of VLA and eMERLIN observations are shown in blue and red respectively.

component is coincident with a bright region of ionized gas seen in [O III]. Given the history of NGC 4388, a contribution from thermal processes is not ruled out. This galaxy is falling into the central part of the Virgo cluster (Yasuda et al. 1997) and gas is being stripped from the galaxy (Greene et al. 2014) resulting in the photo-ionization of gas. In conclusion, we classify the dominant source of radio emission in NGC 4388 as outflow.

– UGC 3193

Our eMERLIN observations show a compact source (see Fig. 4.11), which is resolved into two components in our VLBA observations, located in a north-south direction (Kamali et al. 2019, see Chapter 3). The spectral index $\alpha_5^{33} = 0.33 \pm 0.05$ is most probably underestimated due to the presence of extended diffuse radio emission observed in the 33 GHz VLA map, which is resolved out in the 5 GHz eMERLIN data. $\alpha_{33}^{36} = 0.96 \pm 1.9$ and the diffuse, clumpy radio emission could suggest that SF is the dominant source of radio emission at least on the kpc-scale. The total IR luminosity of $\sim 10^{10.58}$ L$_\odot$, similar to the total IR luminosity of local star forming galaxies, agrees with SF as the origin of radio emission (Wagner 2014). This galaxy lacks an optical spectroscopic classification. However, signatures of an AGN are present. The upper luminosity limit in hard X-rays is $\sim 10^{42.27}$ (Litzinger et al. in. prep.) and the high

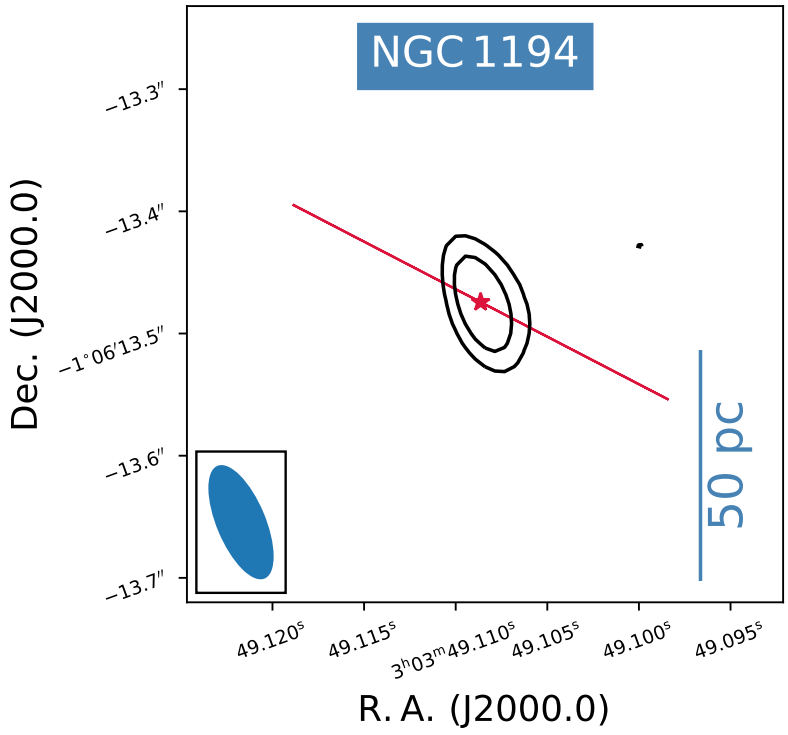

Figure 4.8: Radio continuum map of NGC 1194, obtained using the eMERLIN array in C-band. The contour levels are ±4, 8, 16 and 32 times the rms noise level of an emission-free region in the CLEANed image (~ 37 μJy/beam). The maser position is shown with a red star, and the maser disk's orientation with a red solid line. The synthesized beam and the physical linear scales are shown in the bottom left and right corner respectively.

brightness temperature of ~ 10^7 (Kamali et al. 2019) in addition to the pc-scale core-jet like morphology observed in our high resolution VLBA map, support the AGN scenario. Therefore, a contribution from outflows to the observed radio emission is also possible. In Sect. 4.5.3 we discuss further details related to the spatial relationship of the putative outflow and the maser disk.

– UGC 9639

This source was not observed in our pilot project, and was not detected with the VLBA. In our e-MERLIN data, we see multiple blobs elongated in the north-south direction (see Fig 4.12). Due to the low S/N, the obtained spectral indices have high uncertainty. Information on the maser disk is not available yet. Therefore, we cannot draw conclusions on the nature of the radio emission in this source and we label it as unknown.

We summarize here (also listed in Table 4.3), that out of ten detected sources, radio emission in two sources (NGC 0591 and NGC 4388) is dominated by outflows. In four sources (Mrk 0001, Mrk 1210, NGC 2273 and UGC 3193) both SF and outflows play the dominant role, in one source (Mrk 1419) the bulk of the emission may arise from the jet base or a putative corona, and in three galaxies (Mrk 0078, NGC 1194 and UGC9639) the nature of the radio emission

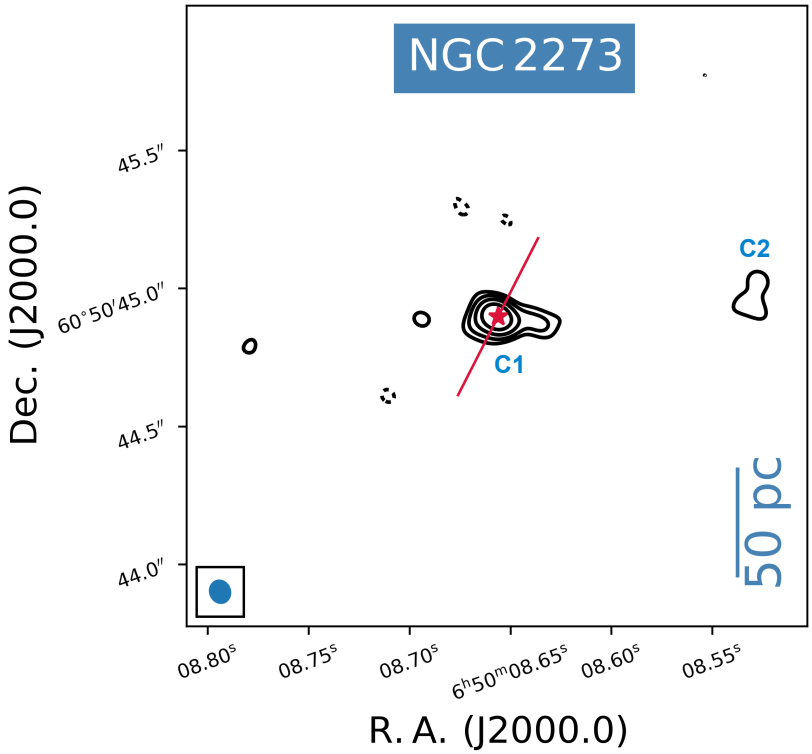

Figure 4.9: Radio continuum map of NGC 2273, obtained using the eMERLIN array in C-band. The contour levels are ±4, 8, 16 and 32 times the rms noise level of an emission-free region in the CLEANed image (~ 72 μJy/beam). The maser position is shown with a red star, and the maser disk's orientation with a red solid line. The synthesized beam and the physical linear scale are shown in the bottom left and right corner respectively.

remains inconclusive.

In order to verify or falsify the above mentioned dominant sources of radio emission in our galaxies, we search for possible correlations between the FIR-radio and X-ray-radio luminosities. We expect a correlation between the X-ray and radio luminosities if the radio emission is dominated by outflows. The top panel of Fig. 4.13 presents the X-ray luminosity versus 5 GHz luminosity for all sources. We do not see any clear correlation. In the lower panel of Fig. 4.13 we present the same analysis, excluding sources with unknown origin for the radio emission. We still do not see any correlation. It should be noted that presenting the same plot for sources which have only outflow as the dominant source of radiation is not reasonable since there are only two such sources. The lack of X-ray-radio luminosity correlation could imply that we still have a large contamination, for instance from the SF, to the radio emission observed on ~ 100 pc-scales.

We also performed the same analysis for FIR-radio luminosities. We expect to see a correlation between the FIR and radio luminosities for SF galaxies (see the introduction to this section). We adopted the FIR fluxes at 100 μm (with the exception of NGC 1194, here we took the 60 μm flux, since a 100 μm flux was not available for this source) from NED, which represent data taken with the Infrared Astronomical Satellite (IRAS). The top panel of Fig. 4.14 presents the FIR luminosities versus the radio luminosities for all ten detected sources. No correlation is evident here. We notice that the one outlier source in the bottom right corner

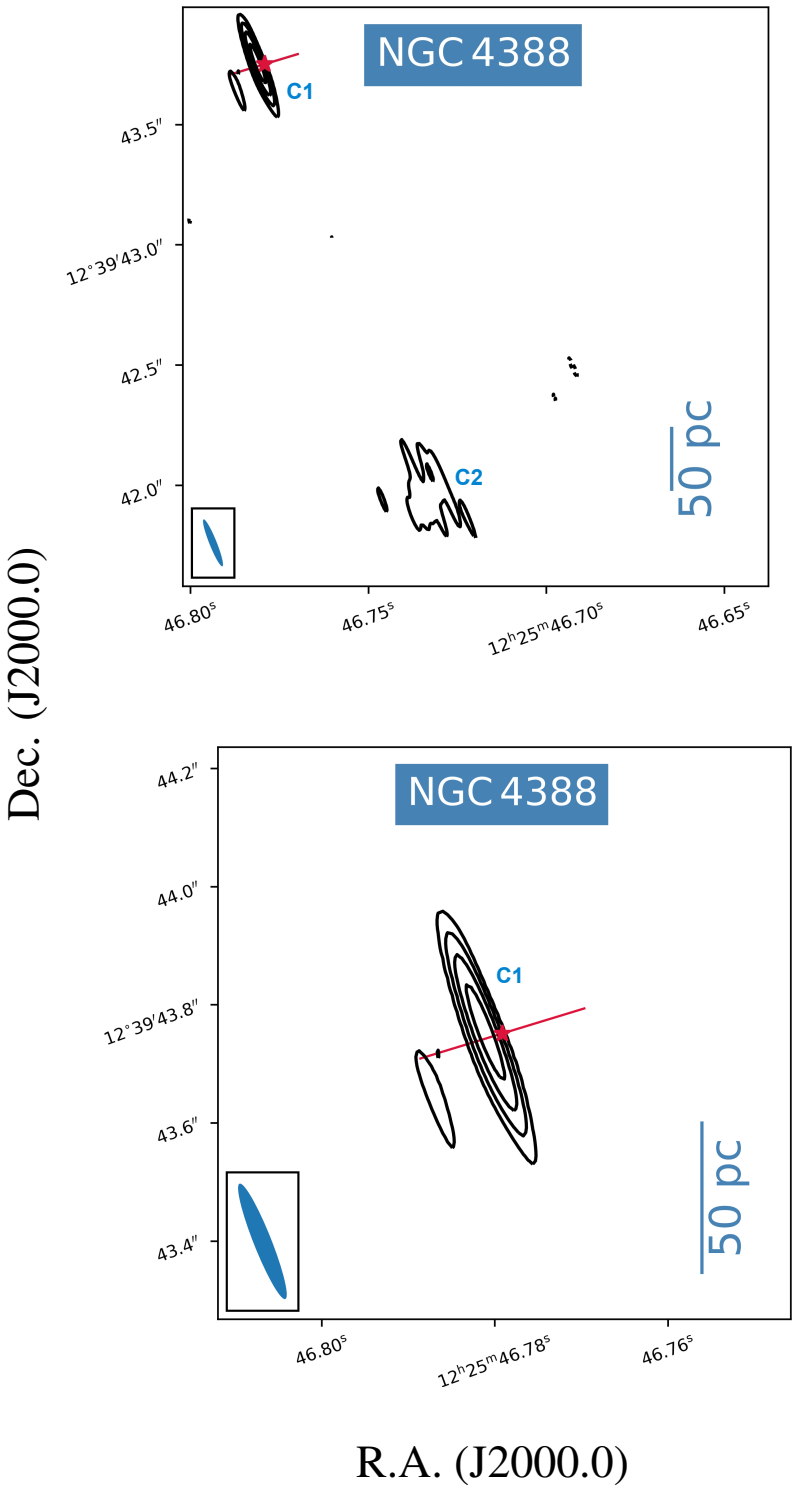

Figure 4.10: Radio continuum map of NGC 4388 (**upper panel**), and a zoom-in frame of the northern component (**lower panel**), obtained using the eMERLIN array in C-band. The contour levels are ±4, 8, 16 and 32 times the rms noise level of an emission-free region in the CLEANed image (~ 27 μJy/beam). The maser position is shown with a red star, and the maser disk's orientation with a red solid line. The synthesized beam and the physical linear scale are shown in the bottom left and right corner respectively.

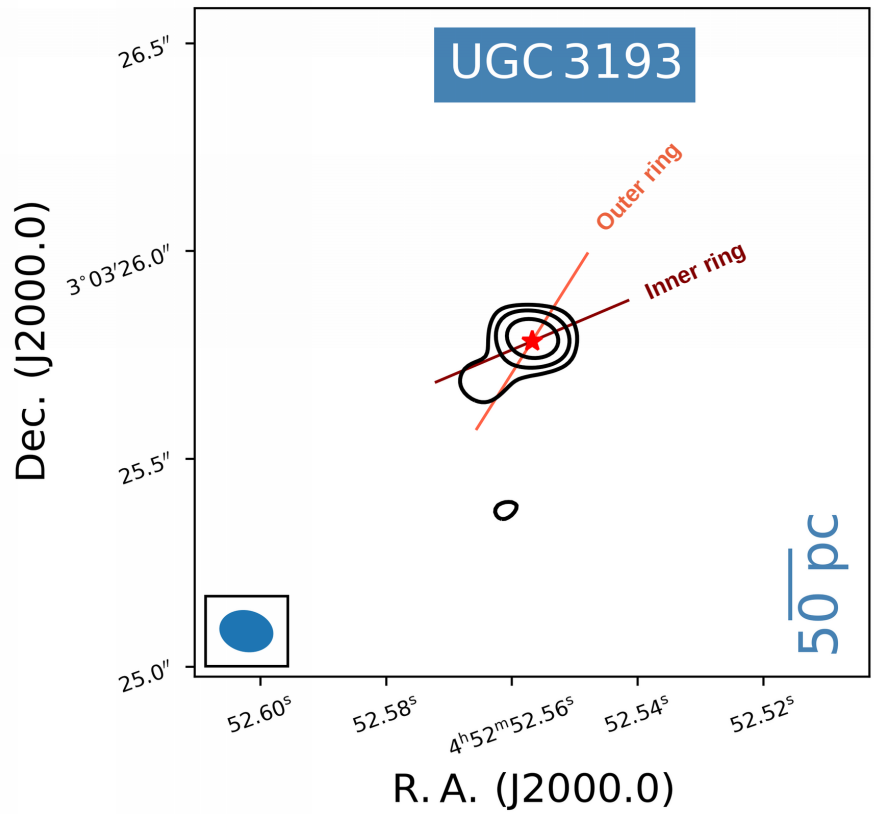

Figure 4.11: Radio continuum map of UGC 3193, obtained using the eMERLIN array in C-band. The contour levels are ±4, 8, 16 and 32 times the rms noise level of an emission-free region in the CLEANed image (~ 51 μJy/beam). The maser position is shown with a red star. The maser disk in UGC 3193 exhibits a complex structure consisting of an inner ring and an outer ring with different position angles (see Sect. 4.5.3). The synthesized beam and the physical linear scale are shown in the bottom left and right corner respectively.

of the plot, Mrk 1210, is highly variable in our observations. Therefore, we present the same plot as the top one, excluding Mrk 1210, in the middle panel of Fig. 4.14. As it is shown in the top left corner of the plot, a correlation with a coefficient of 0.83 and a P-value of 0.01 is observed. We also attempted to plot the FIR-radio luminosities including only the sources with SF/outflow as the dominant source of radio emission. The result is presented in the lower panel of Fig. 4.14. No correlation is observed in this case. The low number of sources are indeed a disadvantage for any statistical analyses. However, the correlation observed in the middle panel of Fig. 4.14 leads to the implication that the radio emission in H_2O -megamaser galaxies is heavily contaminated by SF as well as outflows or jets.

4.5.3 The alignment of the jet with respect to the rotation axis of the maser disk

We measure the orientation of the elongation of the detected radio emission following the method presented in Chapter 3. In sources where we detect one component, the position angle of the deconvolved source represents the orientation of the radio continuum. If there is more

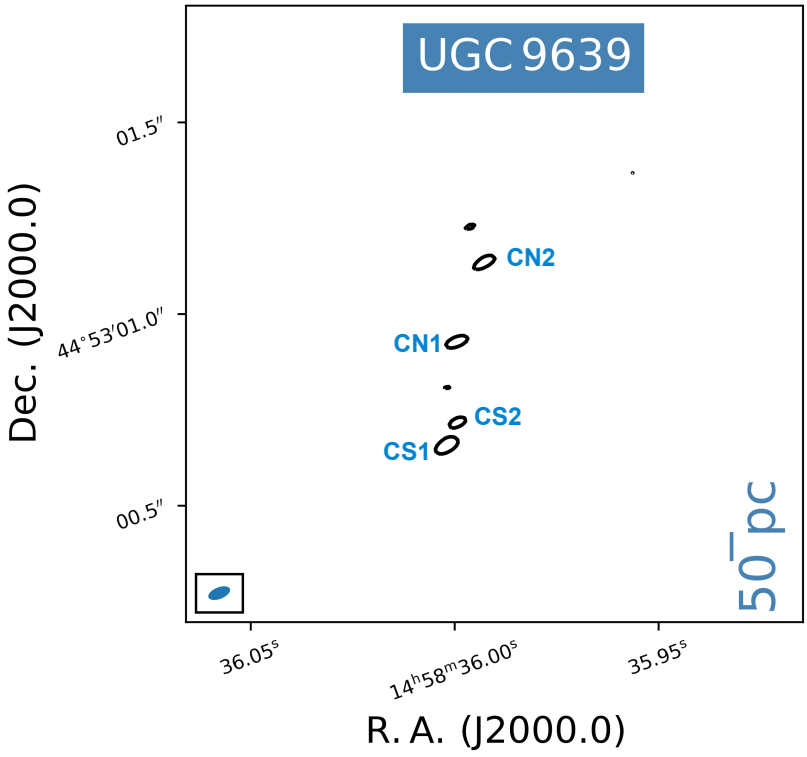

Figure 4.12: Radio continuum map of UGC 9639, obtained using the eMERLIN array in C-band. The contour levels are ±4, 8, 16 and 32 times the rms noise level of an emission-free region in the CLEANed image (~ 37 μJy/beam). The synthesized beam and the physical linear scales are shown in the bottom left and right corner respectively.

than one component, we fit a line to the central positions of the continuum sources. The error budget for the reported PAs resulting from these linear fits takes into account the uncertainties in the central positions of the continuum components. The resulting PAs and their uncertainties are presented in Table 4.3. The orientation of the maser disk is known for seven sources among the detected ones (Mrk 0001, Mrk 1210, Mrk 1419, NGC 1194, NGC 2273, NGC 4388, and UGC 3193). Of these seven sources, three are unresolved within our synthesized beam (Mrk 1419, NGC 1194, UGC 3193). For the remaining four sources (Mrk 0001, Mrk 1210, NGC 2273, and NGC 4388) both the maser disk PA and the radio continuum elongation obtained from eMERLIN observations are known. As presented in Table 4.3 and Fig. 4.15, the radio continuum is misaligned by not more than 37° relative to the rotation axis of the maser disk. If the pc-scale jet direction from the VLBA image is known, it is presented with smaller orange arrows in Fig. 4.15. The pc-scale jet direction and the jet orientation on ~ 100 pc scales are in agreement for all three sources (Mrk 0001, Mrk 1210, NGC 2273) with both available data sets.

Among the sources that are unresolved with the eMERLIN beam, two (Mrk 1419 and UGC 3193) exhibit known VLBA radio continuum elongation (see Chapter 3). For Mrk 1419 we discussed the jet-disk orientation in Chapter 3. However, the spatial relationship of the pc-scale jet direction with the maser disk's PA for UGC 3193 was not discussed in Chapter 3 since the maser disk orientation was not available before. UGC 3193 has a complex maser disk structure. The systemic masers are not detected for this galaxy (Wagner 2014). Furthermore, the presence of two different groups of high velocity masers suggests that the disk is consisting

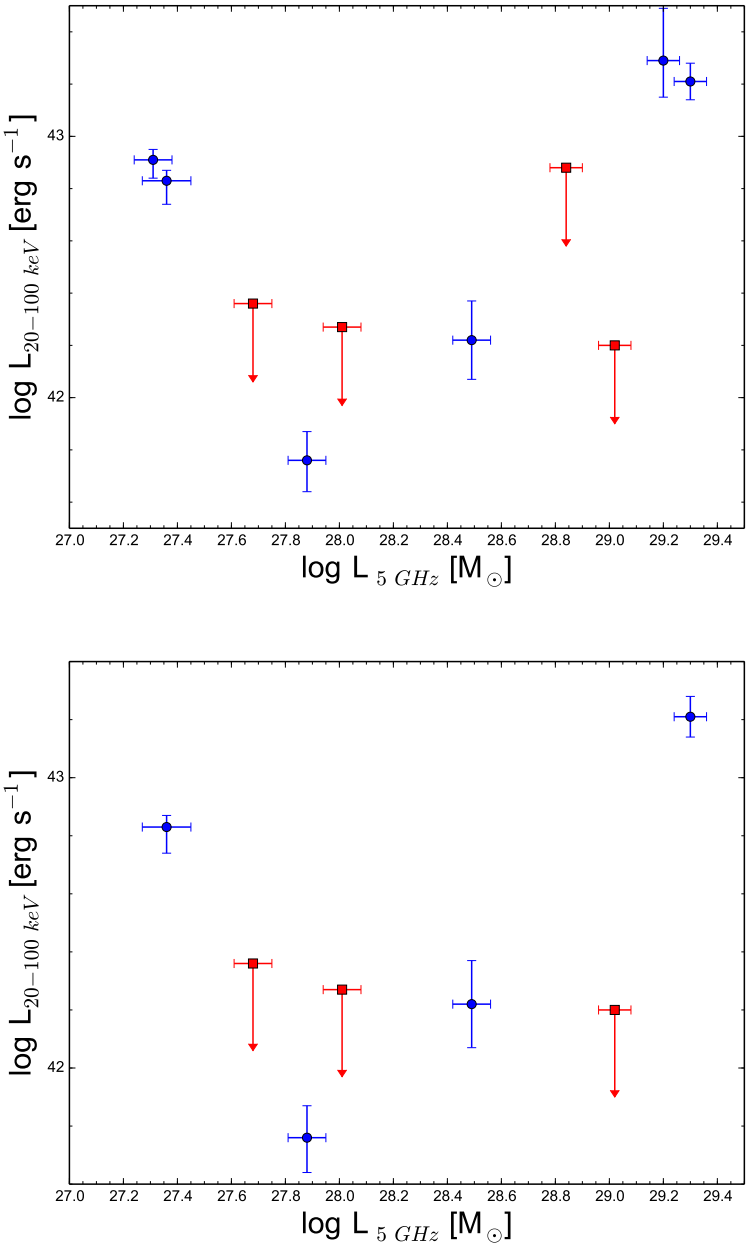

Figure 4.13: X-ray versus 5 GHz radio luminosities for all sourced (**top panel**), and excluding sources with unknown origin for the radio emission (**lower panel**). The red squares with an arrow represent upper limits. The X-ray data are taken from Litzinger et al. (in. prep.), also reported in Kamali et al. (2019).

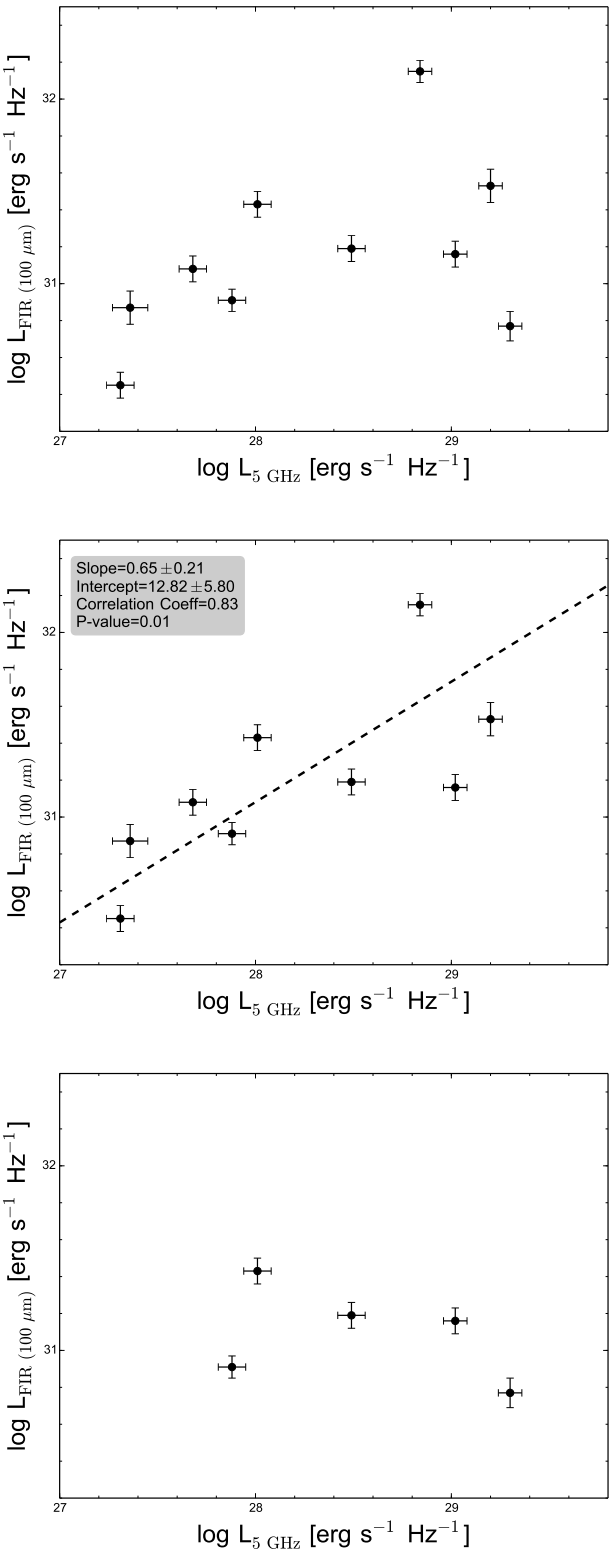

Figure 4.14: Far infrared luminosities versus 5 GHz radio luminosities. The **top panel** presents all ten sources. No correlation is observed. The **middle panel** shows the same as above, excluding Mrk 1210, a highly variable source in our observations. The correlation coefficient, P-value, slope and intercept of the linear fit are shown in the top-left corner of the plot. The **lower panel** shows the FIR versus radio luminosities for the sources with SF as the dominant source of observed radio emission (see Table 4.3). No correlation is observed.

Table 4.3: Position angles and dominant source of radio emission in our sample.

Galaxy	PA (eMERLIN)	PA (Maser disk)	Jet offset	Dominant source	rms
	degree	degree	degree	of radio emission	μJy
Mrk 0001	115±2	6.4±10	19±10	SF/outflow	37
Mrk 0078	78±40	—	—	unknown	71
Mrk 1210	116±15	62.58±0.45	37±15	SF/outflow	64
Mrk 1419	—	49±0.7	—	Jet core/corona	19
NGC 0591	164±6	—	—	outflow	61
NGC 1194	—	157±10	—	unknown	37
NGC 2273	94±7	153±4.6	31±8	SF/outflow	72
NGC 4388	21±6	107±10	4±12	outflow	27
UGC 3193	—	113.2±1.68 inner ring 147.99± 0.03 outer ring	—	SF/outflow	51
UGC 9639	172±4	—	—	unknown	37

Notes. Column 1: name of galaxy. The sources in bold hold clean maser disks (see Sect. 3.2). Column 2: Position angle of the radio continuum/outflow obtained from the 5 GHz eMERLIN data. Column 3: Position angle of the maser disk. Column 4: Jet offset from the rotation axis of the maser disk. Column 5: The dominant source of radio emission in our galaxies (see Sect. 4.5.2) SF stands for star formation. Column 6: The root-mean-square noise (rms) of an emission-free field in the CLEANed image.

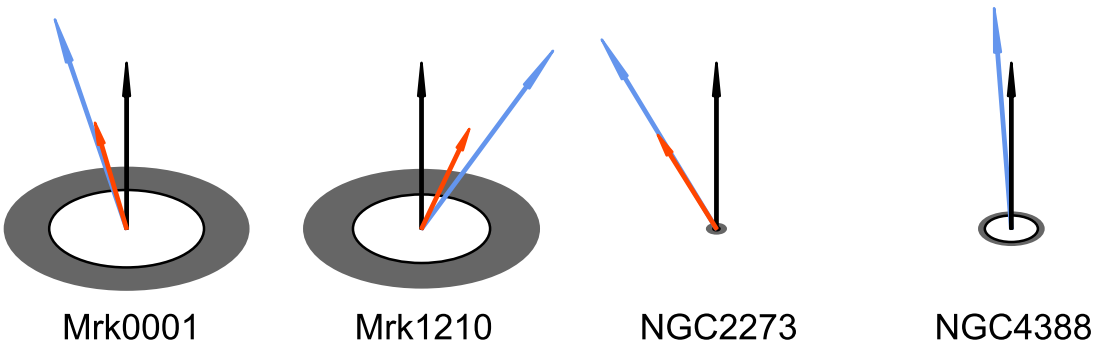

Figure 4.15: The jet direction w.r.t. the maser disk's rotation axis (black arrow). The orange arrows represent the jet direction on pc-scale (taken from Kamali et al. 2019) and the blue arrows represent the jet direction obtained from the eMERLIN observations presented in this chapter. The disk sizes are to scale with respect to each other.

of two concentric rings. The outer ring exhibits relatively slow high velocity masers, offset by $\pm 70\,\mathrm{km\,s^{-1}}$ from the systemic velocity with a PA of $\sim 148^\circ \pm 0.03^\circ$, while the inner ring contains maser groups offset by $\pm 150\,\mathrm{km\,s^{-1}}$ from the systemic velocity of the galaxy, with a PA of $113^\circ \pm 1.7^\circ$ (Wagner 2014). The top panel of Fig. 4.16 shows the 5 GHz VLBA observation of UGC 3193 where the maser position and its uncertainty are presented with a red star. Within the uncertainties, the maser disk's position is consistent with the position of the southern component. The lower panel of Fig. 4.16 presents the direction of the radio continuum elongation with respect to the the maser disk's rotation axis. The pc-scale VLBA and the kpc-scale VLA radio continuum elongations are misaligned with respect to the rotation axis of both the outer and inner rings. However, the misalignment is smaller between the inner ring's rotation axis and the radio continuum elongation ($27^\circ \pm 0.2^\circ$ and $19^\circ \pm 5^\circ$ for the VLA and VLBA data respectively). The outer ring's rotation axis is misaligned with respect to the VLA and VLBA radio continuum direction by $62^\circ \pm 2^\circ$ and $54^\circ \pm 5.3^\circ$, hinting at the possibility that the masers in the outer ring originate from outflows (the outer ring's PA is by $\sim 28^\circ$ misaligned with respect to the VLBA jet direction).

4.6 Conclusion and summary

We observed a sample of 18 LLAGNs that host H_2O -megamaser-disks, using eMERLIN at 5 GHz. Ten sources, Mrk 0001, Mrk 0078, Mrk 1210, Mrk 1419, NGC 0591, NGC 1194, NGC 2273, NGC 4388, UGC 3193, and UGC 9639 are detected at 4σ or higher levels. We further analyze the possible dominant origin of radio emission in our observations, using spectral indices, brightness temperatures and the radio morphologies. We conclude that in two sources, NGC 0591 and NGC 4388, the main contribution to the observed radio emission is from outflows. Four other sources, Mrk 0001, Mrk 1210, NGC 2273, and UGC 3193, show signatures of outflows, but their radio emission is possibly heavily contaminated by star formation as well. The radio emission in one source, Mrk 1419, is dominated by emission from a putative corona or jet base. In three other sources, Mrk 0078, NGC 1194, and UGC 9639, the origin of radio emission remain inconclusive based on our data. The radio emission in two sources, NGC 1194 and NGC 4388, might also be contaminated by free-free emission. More information such as star formation rate and star formation history of these galaxies, as well as large bandwidth polarization studies are required to further investigate the origin of radio emission in H_2O -megamaser galaxies. We also analyzed the direction of the observed radio emission with respect to the rotation axis of the maser disk. We conclude that in our sample, the jet is always oriented within 37° of the disk's rotation axis. Further investigations are needed to probe jet precession in our sample.

Acknowledgments

F. K. would like to thank Javier Moldon for his constructive comments on the data reduction process. This chapter is based on the data from the eMERLIN facility, a national facility operated by the University of Manchester at Jodrell Bank Observatory on behalf of STFC.

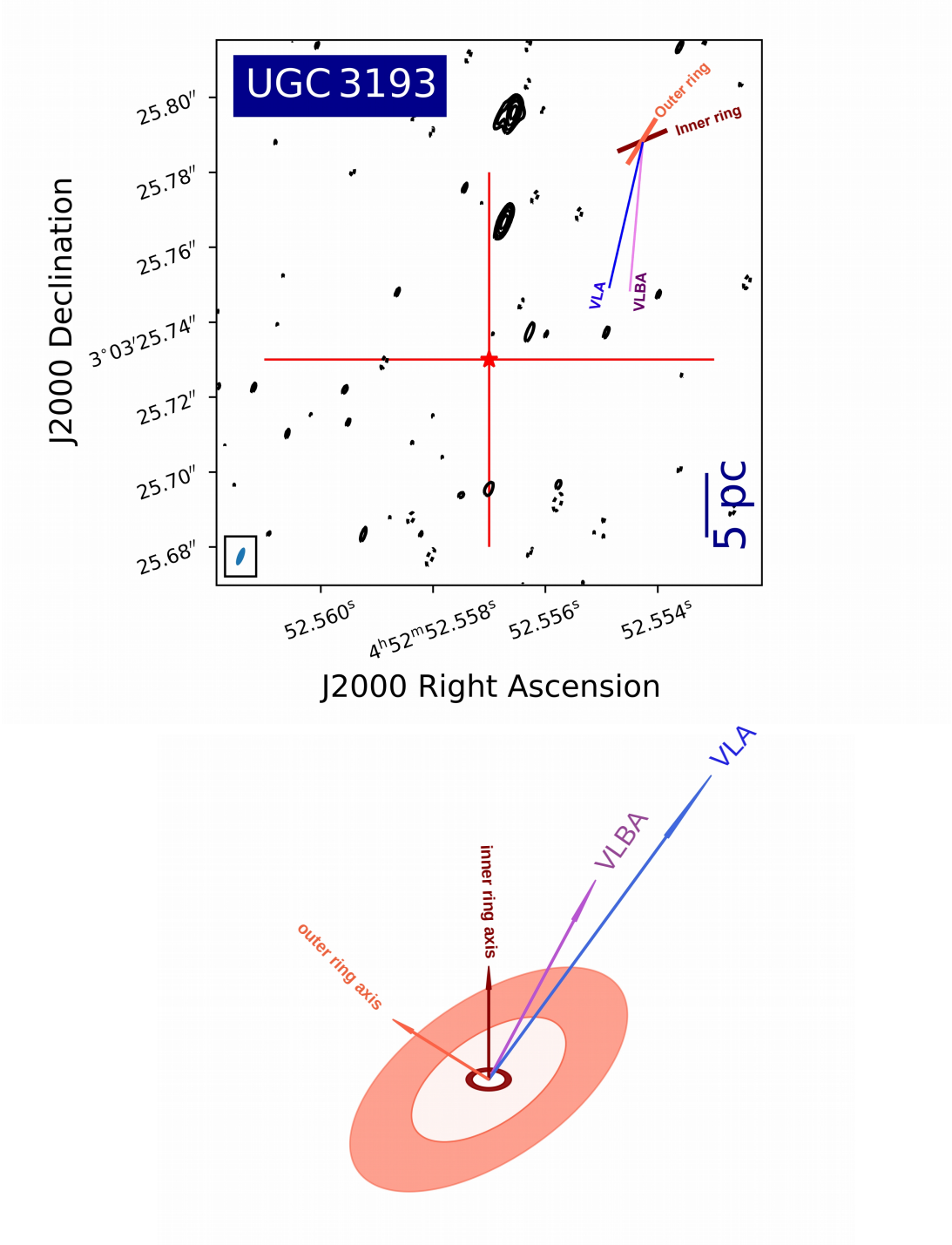

Figure 4.16: **Top panel:** radio continuum map of UGC 3193, obtained using the VLBA at 5 GHz (Kamali et al. 2019). The maser position is shown with a star, and its uncertainty with a red cross. The inner ring of the maser disk is shown in dark red and the outer ring in light red, in the top right corner of the plot. The directions of the radio jets obtained from different data are also presented. **Lower panel:** the inner ring (dark red) and the outer ring (light red) of the maser disk and their associated rotation axes. The radio continuum elongations obtained from the VLA and the VLBA data are also presented (see Sect. 4.5.3 for more details).

CHAPTER 5

Summary of the thesis and outlook

In this thesis, we studied the radio continuum of a sample of low luminosity active galaxies (LLAGNs) hosting H_2O -megamaser-disks, using three different radio interferometer arrays. Emission from the 22 GHz H_2O -maser transition observed in the accretion disks of LLAGNs allows us to directly observe the accretion disk at pc to sub-pc scales, revealing the central mass and disk morphology (e.g., the degree of warping). It is clear that this one spectral line cannot provide the entire picture because the maser emission is confined to specific physical and chemical conditions, namely kinetic temperatures of ~300–1000 K and densities $> 10^7$ cm^{-3}. Therefore observations at other frequencies are needed to gain a broader and more accurate picture of the environment surrounding the SMBHs. X-ray, optical, and infrared observations are severely hampered by a lack of angular resolution and/or high extinction and cannot resolve the targets observed at radio frequencies. Hence, the best complement to H_2O -maser observations is the radio continuum, which is not affected by obscuration and allows high resolution studies. The radio continuum also traces jets or outflows launched by the AGN. Therefore observing the radio continuum provides the unique opportunity to directly observe the central part of active galaxies with the same linear resolution as the maser disk. Complementing H_2O -maser accretion disk observations with maps of putative jets in the radio continuum, the spatial relationship of the radio jets and megamaser disks could finally be studied in detail.

We initially observed a sample of 24 H_2O -megamaser galaxies with the Karl G. Jansky Very Large Array (VLA) at 33 GHz, to first assure that radio emission is detected. The sample was later observed with higher resolution and at lower frequencies at which jets are presumably brighter. The VLA observations resulted in the detection of 21 sources; four of them showing biconical structure associated with jets, and the rest showing only one component often accompanied by extended diffuse emission. These observations provided central positions of the galaxies accurate up to 20-280 mas. Using correlation analyses, we demonstrated that the inner radii of the disks show stronger correlations with 1.4 GHz, 33 GHz, and hard X-ray luminosities than their outer radii, possibly because the outer radii are affected by star formation or disk warping.

We later observed 14 sources from our pilot survey, and four other H_2O -megamaser galaxies, using the Very Long Baseline Array (VLBA) at 5 GHz. These observations resulted in a $\sim$ 26% detection rate (5 out of 18). While all five sources are known to have maser disks, only for four of them the orientation of the maser disk is known. For all four sources, the radio continuum is misaligned relative to the rotation axis of the maser disk, but at a 99.1% confidence level, the orientations are not random and are confined to a cone within 32° of the maser disk's normal. Among these four sources the misalignment of the radio continuum with respect to the normal vector to the maser disk is smaller when the inner radius of the maser disk is larger.

To further investigate the low detection rate of our VLBA observations, we observed the same sample using the enhanced Multi-Element Radio Linked Interferometer Network (eMERLIN) at 5 GHz. These observations had an intermediate resolution, between that of the VLA and the VLBA. We detect ten out of 18 sources, including five sources already detected with the VLBA. Information on the orientation of the maser disks is available for four sources with measured radio continuum elongations form the eMERLIN observations. We find that the radio continuum is misaligned to the rotation axis of the maser disks, but confined to a cone within 37° of the normal vector to the maser disk. We further investigated the origin of radio emission in our data, using the radio morphologies on different scales, spectral indices, brightness temperatures and correlation analyses. We conclude that in the majority of our sources, both outflow and star formation are contributing to the observed radio continuum emission.

During the course of this study, we encountered sources that exhibit strong H_2O -megamaser emission but which are not detected in the radio continuum. For example, J0437+2456 is an H_2O -megamaser host that remains undetected in all radio continuum surveys (also in our VLA pilot project) and also in the hard X-ray survey of Litzinger et. al. (in.prep). Future wide-band polarization studies of disk-megamaser galaxies could help us to investigate the role of the magnetic field and to better constrain the origin of the radio emission. Another complement to radio continuum studies of H_2O -megamaser galaxies should be mm/submm molecular line observations of shock-tracing molecules such as SiO. The NOrthern Extended Millimeter Array (NOEMA) at Plateau de Bure, or the Atacama Large Millimeter/submillimeter Array (ALMA), are great facilities to perform such observations. With the current status of NOEMA, an angular resolution of 0.1 arcseconds could be achieved which corresponds to 41 pc at 85 Mpc. We could observe SiO more or less at the same resolution as our eMERLIN observations, and investigate how the molecular outflows are related to the observed radio continuum. Furthermore, we could constrain the contribution of outflows to the observed radio emission.

Acknowledgements

This thesis would have been impossible without guidance, support, love and existence of many people and phenomena.

Before I begin, I would like to thank Prof. Karl Menten, who gave me the opportunity to work in his research group. He could always find time to listen to my progress reports, and understood the unexpected difficulties and challenges I faced during my PhD project. Thank you Karl!

I would also like to thank Prof. Pavel Kroupa, Prof. Simon Stellmer and Prof. Volkmar Gieselmann for agreeing to be part of my thesis examination committee.

I am grateful to Andreas Brunthaler, Shoko Koyama, Sergio Abraham Dzib Quijano, and Gisela Noemi Ortiz-Leon for helping me to understand the radio interferometry data. I would like to thank Emmanouil Angelakis for his advice on how to proceed with my PhD at the time I faced unexpected problems with the project. I am also thankful to Ioannis Myserlis for proof-reading parts of this thesis.

And most importantly, I would like to express my deepest gratitude to Christian Henkel, for his lessons on scientific writing. He always read (patiently) my drafts and taught me how to nurture them and create a smooth, reader-friendly version, and to be critical of every sentence that I write. Thank you Christian for your advice, and for always being there to read my drafts, especially when I had deadlines!

I have been inspired by many people, a few I would like to mention here. I am grateful that I had wonderful teachers and mentors, through out my life time. Behrooz Zerafat, my highschool physics teacher and Khadije Bozorginejad my high-school principle who encouraged me to follow my dream and study astronomy. Mehdi Jahanmiri, Ahmad Poostforoush, and Nematollah Riazi who taught me the principles of astronomy during my bachelor studies. Jaccco van Loon, for his guidance and help on continuing my higher education in astronomy.

I would like to thank my dearest *office-mates*, Hansito, Nina, Richa, JB and KKs, for making our office (the place that we lived in, most of our wakeful time) an enjoyable place. Every day that I came to work I felt I am going to my second home :-) Thank you guys for bearing with me (and my plants), and never complaining that I open the windows.

Many special thanks to all my friends that made my stay in Bonn more exciting! Thank you Maitraiyee for your everyday supportive hugs, Negar for your shopping company and amazing discussions about evolution, Ana and Joey for making me a more social person, Farzaneh, Annalena, Arshia, Amit, Natasha, Marilyn, Eleni, Michael, Vivien, Geomarr, Wonju, KaTat, Carsten, Andishe, Zeinab, and other members of IMPRS and mm/submm astronomy group. My lovely Shalgham friends, Fatima, Davood, Diana, Alireza, Shiva, Amir, Eli, Hojjat, Homa, Tanaz, Mehdi and Mitra, my girls Yulia and Sarah, for all the leisure time activities and total nonsense conversations which was occasionally what I needed after a long day at work.

I would like to thank the Bi-Bu food stand in Bonn's Marktplatz for making the best falafel and soya-gyros sandwiches in the world, which motivated me to work on Saturdays in the last few months of writing-up.

I am very grateful for the existence of the river Rhein, which made running and cycling a

more enjoyable part of my PhD.

And of course, I am truly grateful to my family, who have always supported me, although I chose a path different from what they would have liked. Their contribution is not only love and support; they also contributed towards what inspired my career path. I would like to thank my mother, who gave me my first astronomy book when I was 11, my father who helped me buy a telescope when I was 15 and occasionally gave me company while I was camping and observing the night sky, my brother and sister for their unconditional love, and most of all to my lovely nieces, Paeezan and Arnika, who make me laugh and feel loved more than anything else.

I am indeed very lucky to have met my best friend, Behnam Javanmardi, and had him by my side in this PhD journey. He always tried to be there for me, either virtually or in reality, and helped me get through the difficult times I have had in this journey. Thanks for the philosophical, astronomical, anthropological, and nonsense discussions. Thanks for all the time you spent on the airplanes and trains to be by my side in the last few years.

In the end, I would like to thank all those people (and putative aliens) who consciously (or even unconsciously) contributed to understanding the Universe(s).

List of publications

First author publications:

- **Accretion disk versus jet orientation in H_2O megamaser galaxies**
  Kamali, F.; Henkel, C.; Koyama, S.; Kuo, C. Y.; Condon, J. J.; Brunthaler, A.; Reid, M. J.; Greene, J. E.; Menten, K. M.; Impellizzeri, C. M. V.; Braatz, J. A.; Litzinger, E.; Kadler, M. (2019) A&A, 624, A42
  DOI:10.1051/0004-6361/201834600
  This paper corresponds to Chapter 3

- **Radio continuum of galaxies with H_2O megamaser disks**
  Kamali, F.; Henkel, C.; Brunthaler, A.; Impellizzeri, C. M. V.; Menten, K. M.; Braatz, J. A.; Greene, J. E.; Reid, M. J.; Condon, J. J.; Lo, K. Y.; Kuo, C. Y.; Litzinger, E.; Kadler, M., 2018IAUS..336..139K
  DOI: 10.1017/S174392131701095X

- **Radio continuum of galaxies with H_2O megamaser disks: 33 GHz VLA data**
  Kamali, F.; Henkel, C.; Brunthaler, A.; Impellizzeri, C. M. V.; Menten, K. M.; Braatz, J. A.; Greene, J. E.; Reid, M. J.; Condon, J. J.; Lo, K. Y.; Kuo, C. Y.; Litzinger, E.; Kadler, M. (2017) A&A, 605, A84
  DOI:10.1051/0004-6361/201730899
  This paper corresponds to Chapter 2

n^{th} author publications:

- **Extragalactic maser surveys**
  Henkel, C.; Greene, J.-E.; **Kamali, F.**, 2018IAUS..336...69H
  DOI: 10.1017/S1743921318000753

- **Molecular line emission in NGC 4945, imaged with ALMA**

  Henkel, C.; Mühle, S.; Bendo, G.; Józsa, G. I. G.; Gong, Y.; Viti, S.; Aalto, S.; Combes, F.; García-Burillo, S.; Hunt, L. K.; Mangum, J.; Martín, S.; Muller, S.; Ott, J.; van der Werf, P.; Malawi, A. A.; Ismail, H.; Alkhuja, E.; Asiri, H. M.; Aladro, R.; Alves, F.; Ao, Y.; Baan, W. A.; Costagliola, F.; Fuller, G.; Greene, J.; Impellizzeri, C. M. V.; **Kamali, F.**; Klessen, R. S.; Mauersberger, R.; Tang, X. D.; Tristram, K.; Wang, M.; Zhang, J. S. (2018) A&A, 615, A155
  DOI: 10.1051/0004-6361/201732174

Bibliography

Adams, T. F. 1973, ApJ, 179, 417

Almeida, C. R. & Ricci, C. 2017, Nature Astronomy, 1, 679

Anderson, J. M. & Ulvestad, J. S. 2005, ApJ, 627, 674

Antonucci, R. R. J. & Miller, J. S. 1985, ApJ, 297, 621

Baldi, R. D., Williams, D. R. A., McHardy, I. M., et al. 2018, MNRAS, 476, 3478

Barthel, P. D. 1989, ApJ, 336, 606

Bassani, L., Dadina, M., Maiolino, R., et al. 1999, ApJS, 121, 473

Baum, S. A. & Heckman, T. 1989, ApJ, 336, 702

Becker, R. H., White, R. L., & Helfand, D. J. 1995, ApJ, 450, 559

Bennett, C. L., Larson, D., Weiland, J. L., et al. 2013, ApJS, 208, 20

Blandford, R., Meier, D., & Readhead, A. 2018, arXiv e-prints

Blandford, R. D. & Königl, A. 1979, ApJ, 232, 34

Blundell, K. M. & Beasley, A. J. 1998, MNRAS, 299, 165

Blundell, K. M. & Kuncic, Z. 2007, ApJ, 668, L103

Bonchi, A., La Franca, F., Melini, G., Bongiorno, A., & Fiore, F. 2013, MNRAS, 429, 1970

Braatz, J., Condon, J., Constantin, A., et al. 2015a, IAU General Assembly, 22, 2255730

Braatz, J., Condon, J., Constantin, A., et al. 2015b, IAU General Assembly, 22, 2255730

Braatz, J., Condon, J., Henkel, C., et al. 2018, in IAU Symposium, Vol. 336, Astrophysical Masers: Unlocking the Mysteries of the Universe, ed. A. Tarchi, M. J. Reid, & P. Castangia, 86–91

Braatz, J. A. & Gugliucci, N. E. 2008, ApJ, 678, 96

Braatz, J. A., Henkel, C., Greenhill, L. J., Moran, J. M., & Wilson, A. S. 2004, ApJ, 617, L29

Braatz, J. A., Reid, M. J., Humphreys, E. M. L., et al. 2010, ApJ, 718, 657

Buttiglione, S., Capetti, A., Celotti, A., et al. 2010, A&A, 509, A6

Capetti, A., Massaro, F., & Baldi, R. D. 2017, A&A, 601, A81

Carroll, B. W. & Ostlie, D. A. 2006, An Introduction to Modern Astrophysics (ISBN 978-0805304022: Addison-Wesley. p. 333.)

Castangia, P., Panessa, F., Henkel, C., Kadler, M., & Tarchi, A. 2013, MNRAS, 436, 3388

Cecil, G., Wilson, A. S., & Tully, R. B. 1992, ApJ, 390, 365

Chemin, L., Renaud, F., & Soubiran, C. 2015, A&A, 578, A14

Cheung, A. C., Rank, D. M., Townes, C. H., Thornton, D. D., & Welch, W. J. 1969, Nature, 221, 626

Churchwell, E., Witzel, A., Huchtmeier, W., et al. 1977, A&A, 54, 969

Condon, J. & Ransom, S. 2016, Essential Radio Astronomy, Princeton series in modern observational astronomy (Princeton University Press)

Condon, J. J. 1992, ARA&A, 30, 575

Condon, J. J., Cotton, W. D., Greisen, E. W., et al. 1998, AJ, 115, 1693

Corbel, S., Aussel, H., Broderick, J. W., et al. 2013, MNRAS, 431, L107

Corbin, M. R., Baldwin, J. A., & Wilson, A. S. 1988, ApJ, 334, 584

Curtis, H. D. 1918, Publications of Lick Observatory, 13, 9

Damas-Segovia, A., Beck, R., Vollmer, B., et al. 2016, ApJ, 824, 30

Diamond-Stanic, A. M., Rieke, G. H., & Rigby, J. R. 2009, ApJ, 698, 623

Dunkley, J., Spergel, D. N., Komatsu, E., et al. 2009, ApJ, 701, 1804

Elvis, M., Wilkes, B. J., McDowell, J. C., et al. 1994, ApJS, 95, 1

Erwin, P. & Sparke, L. S. 2003, ApJS, 146, 299

Event Horizon Telescope Collaboration, Akiyama, K., Alberdi, A., et al. 2019, ApJ, 875, L1

Fabbiano, G., Wang, J., Elvis, M., & Risaliti, G. 2011, Nature, 477, 431

Falcke, H. & Biermann, P. L. 1995, A&A, 293, 665

Falcke, H., Wilson, A. S., & Simpson, C. 1998, ApJ, 502, 199

Fanaroff, B. L. & Riley, J. M. 1974, MNRAS, 167, 31P

Fender, R. P., Belloni, T. M., & Gallo, E. 2004, MNRAS, 355, 1105

Fiore, F., Grazian, A., Santini, P., et al. 2008, ApJ, 672, 94

Freedman, W. L., Madore, B. F., Gibson, B. K., et al. 2001, ApJ, 553, 47

Freedman, W. L., Madore, B. F., Scowcroft, V., et al. 2012, ApJ, 758, 24

Gallimore, J. F., Henkel, C., Baum, S. A., et al. 2001, ApJ, 556, 694

Gao, F., Braatz, J. A., Reid, M. J., et al. 2017, ApJ, 834, 52

Gao, F., Braatz, J. A., Reid, M. J., et al. 2016, ApJ, 817, 128

Georgantopoulos, I., Georgakakis, A., Rowan-Robinson, M., & Rovilos, E. 2008, A&A, 484, 671

Giroletti, M. & Panessa, F. 2009, ApJ, 706, L260

Gordon, J. P., Zeiger, H. J., & Townes, C. H. 1954, Phys. Rev., 95, 282

Greene, J. E., Peng, C. Y., Kim, M., et al. 2010, ApJ, 721, 26

Greene, J. E., Seth, A., den Brok, M., et al. 2013, ApJ, 771, 121

Greene, J. E., Seth, A., Kim, M., et al. 2016, ApJ, 826, L32

Greene, J. E., Seth, A., Lyubenova, M., et al. 2014, ApJ, 788, 145

Greenhill, L. J., Jiang, D. R., Moran, J. M., et al. 1995, ApJ, 440, 619

Gültekin, K., Cackett, E. M., Miller, J. M., et al. 2009, ApJ, 706, 404

Heckman, T. M. 1980, A&A, 87, 152

Heckman, T. M. & Best, P. N. 2014, ARA&A, 52, 589

Heckman, T. M., Ptak, A., Hornschemeier, A., & Kauffmann, G. 2005, ApJ, 634, 161

Henkel, C., Peck, A. B., Tarchi, A., et al. 2005, A&A, 436, 75

Herrnstein, J. R., Greenhill, L. J., Moran, J. M., et al. 1998, ApJ, 497, L69

Herrnstein, J. R., Moran, J. M., Greenhill, L. J., et al. 1999, Nature, 400, 539

Herrnstein, J. R., Moran, J. M., Greenhill, L. J., et al. 1997, ApJ, 475, L17

Hine, R. G. & Longair, M. S. 1979, MNRAS, 188, 111

Hlavacek-Larrondo, J., Carignan, C., Daigle, O., et al. 2011, MNRAS, 411, 71

Hopkins, P. F. & Quataert, E. 2010, MNRAS, 407, 1529

Humphreys, E. M. L., Reid, M. J., Moran, J. M., Greenhill, L. J., & Argon, A. L. 2013, ApJ, 775, 13

Impellizzeri, C. M. V., McKean, J. P., Castangia, P., et al. 2008, Nature, 456, 927

Ishihara, Y., Nakai, N., Iyomoto, N., et al. 2001, PASJ, 53, 215

Kamali, F. 2014, Master's thesis

Kamali, F., Henkel, C., Brunthaler, A., et al. 2017, A&A, 605, A84

Kamali, F., Henkel, C., Koyama, S., et al. 2019, A&A, 624, A42

Kaspi, S., Maoz, D., Netzer, H., et al. 2005, ApJ, 629, 61

Kellermann, K. I., Sramek, R., Schmidt, M., Shaffer, D. B., & Green, R. 1989, AJ, 98, 1195

Kinney, A. L., Schmitt, H. R., Clarke, C. J., et al. 2000, ApJ, 537, 152

Klein, U. 2014, Lecture notes. Radio astronomy, tools, applications and impacts

Komatsu, E., Smith, K. M., Dunkley, J., et al. 2011, ApJS, 192, 18

Kondratko, P. T., Greenhill, L. J., & Moran, J. M. 2006a, ApJ, 652, 136

Kondratko, P. T., Greenhill, L. J., & Moran, J. M. 2008, ApJ, 678, 87

Kondratko, P. T., Greenhill, L. J., Moran, J. M., et al. 2006b, ApJ, 638, 100

Körding, E., Falcke, H., & Corbel, S. 2006, A&A, 456, 439

Kormendy, J. & Ho, L. C. 2013, ARA&A, 51, 511

Kormendy, J. & Richstone, D. 1995, ARA&A, 33, 581

Koss, M. J., Romero-Cañizales, C., Baronchelli, L., et al. 2015, ApJ, 807, 149

Krumholz, M. R. & Kruijssen, J. M. D. 2015, MNRAS, 453, 739

Kuo, C. Y., Braatz, J. A., Condon, J. J., et al. 2011, ApJ, 727, 20

Kuo, C. Y., Braatz, J. A., Lo, K. Y., et al. 2015, ApJ, 800, 26

Kuo, C. Y., Braatz, J. A., Reid, M. J., et al. 2013, ApJ, 767, 155

Kuo, C. Y., Constantin, A., Braatz, J. A., et al. 2018, ApJ, 860, 169

Lal, D. V., Shastri, P., & Gabuzda, D. C. 2004, A&A, 425, 99

Laor, A. & Brandt, W. N. 2002, ApJ, 569, 641

Läsker, R., Greene, J. E., Seth, A., et al. 2016, ApJ, 825, 3

Liddle, A. 2015, An Introduction to Modern Cosmology, 3rd Edition (Wiley)

Lo, K. Y. 2005, ARA&A, 43, 625

Makarov, D., Prugniel, P., Terekhova, N., Courtois, H., & Vauglin, I. 2014, A&A, 570, A13

Masini, A., Comastri, A., Baloković, M., et al. 2016, A&A, 589, A59

Masini, A., Comastri, A., Puccetti, S., et al. 2017, A&A, 597, A100

Mateos, S., Carrera, F. J., Alonso-Herrero, A., et al. 2016, ApJ, 819, 166

Mazzalay, X. & Rodríguez-Ardila, A. 2007, A&A, 463, 445

McMullin, J. P., Waters, B., Schiebel, D., Young, W., & Golap, K. 2007, in Astronomical Society of the Pacific Conference Series, Vol. 376, Astronomical Data Analysis Software and Systems XVI, ed. R. A. Shaw, F. Hill, & D. J. Bell, 127

Merloni, A., Heinz, S., & di Matteo, T. 2003, MNRAS, 345, 1057

Middelberg, E., Roy, A. L., Nagar, N. M., et al. 2004, A&A, 417, 925

Miyoshi, M., Moran, J., Herrnstein, J., et al. 1995, Nature, 373, 127

Mundell, C. G., Ferruit, P., Nagar, N., & Wilson, A. S. 2009, ApJ, 703, 802

Nagar, N. M. & Wilson, A. S. 1999, ApJ, 516, 97

Nakai, N., Inoue, M., & Miyoshi, M. 1993, Nature, 361, 45

Netzer, H. 2015, ARA&A, 53, 365

Neufeld, D. A. & Maloney, P. R. 1995, ApJ, 447, L17

Neufeld, D. A., Maloney, P. R., & Conger, S. 1994, ApJ, 436, L.127

Nisbet, D. M. & Best, P. N. 2016, MNRAS, 455, 2551

Omar, A., Dwarakanath, K. S., Rupen, M., & Anantharamaiah, K. R. 2002, A&A, 394, 405

Osterbrock, D. & Ferland, G. 2006, Astrophysics of Gaseous Nebulae and Active Galactic Nuclei (University Science Books)

Osterbrock, D. E. & Pogge, R. W. 1985, ApJ, 297, 166

Padovani, P. 2016, A&A Rev., 24, 13

Padovani, P., Alexander, D. M., Assef, R. J., et al. 2017, A&A Rev., 25, 2

Panessa, F., Baldi, R. D., Laor, A., et al. 2019, Nature Astronomy

Parsons, A. 2013, Lecture notes. Radio Astronomy: Tools and Techniques

Pesce, D. W., Braatz, J. A., Condon, J. J., et al. 2015, ApJ, 810, 65

Petitpas, G. R. & Wilson, C. D. 2002, ApJ, 575, 814

Piner, B. G., Stone, J. M., & Teuben, P. J. 1995, ApJ, 449, 508

Pjanka, P., Greene, J. E., Seth, A. C., et al. 2017, ApJ, 844, 165

Planck Collaboration, Ade, P. A. R., Aghanim, N., et al. 2014, A&A, 571, A16

Planck Collaboration, Ade, P. A. R., Aghanim, N., et al. 2016, A&A, 594, A13

Planck Collaboration, Aghanim, N., Akrami, Y., et al. 2018, arXiv e-prints

Pogge, R. W. 1988, ApJ, 332, 702

Pringle, J. E., Antonucci, R. R. J., Clarke, C. J., et al. 1999, ApJ, 526, L9

Quirk, W. J. 1972, ApJ, 176, L9

Rawlings, S. & Saunders, R. 1991, Nature, 349, 138

Reid, M. J., Braatz, J. A., Condon, J. J., et al. 2009, ApJ, 695, 287

Reid, M. J., Braatz, J. A., Condon, J. J., et al. 2013, ApJ, 767, 154

Riess, A. G., Macri, L., Casertano, S., et al. 2011, ApJ, 730, 119

Riess, A. G., Macri, L., Casertano, S., et al. 2009, ApJ, 699, 539

Riess, A. G., Macri, L. M., Hoffmann, S. L., et al. 2016, ApJ, 826, 56

Riffel, R. A. & Storchi-Bergmann, T. 2011, MNRAS, 417, 2752

Safronov, V. S. 1960, Annales d'Astrophysique, 23, 979

Sagan, C. 1977, The Dragons of Eden: Speculations on the Evolution of Human Intelligence (ISBN 0-394-41045-9: Random House)

Saikia, P., Körding, E., & Falcke, H. 2015, MNRAS, 450, 2317

Salpeter, E. E. 1964, ApJ, 140, 796

Sargent, M. T., Schinnerer, E., Murphy, E., et al. 2010, ApJS, 186, 341

Sargent, W. L. W. 1972, ApJ, 173, 7

Schmitt, H. R., Pringle, J. E., Clarke, C. J., & Kinney, A. L. 2002, ApJ, 575, 150

Schmitt, H. R., Ulvestad, J. S., Antonucci, R. R. J., & Kinney, A. L. 2001, The Astrophysical Journal Supplement Series, 132, 199

Seyfert, C. K. 1943, ApJ, 97, 28

Sopp, H. M. & Alexander, P. 1991, MNRAS, 251, 14P

Spergel, D. N., Bean, R., Doré, O., et al. 2007, ApJS, 170, 377

Spergel, D. N., Verde, L., Peiris, H. V., et al. 2003, ApJS, 148, 175

Stern, D., Assef, R. J., Benford, D. J., et al. 2012, ApJ, 753, 30

Sun, A.-L., Greene, J. E., Impellizzeri, C. M. V., et al. 2013, ApJ, 778, 47

Tadhunter, C. 2008, New A Rev., 52, 227

Terlouw, J. P. & Vogelaar, M. G. R. 2015, Kapteyn Package, version 2.3, Kapteyn Astronomical Institute, Groningen, available from http://www.astro.rug.nl/software/kapteyn/

Toomre, A. 1964, ApJ, 139, 1217

Ulvestad, J. S. & Wilson, A. S. 1984, ApJ, 285, 439

Urry, C. M. & Padovani, P. 1995, PASP, 107, 803

Van den Bosch, R. C. E., Greene, J. E., Braatz, J. A., Constantin, A., & Kuo, C.-Y. 2016, ApJ, 819, 11

Wagner, J. 2014, PhD thesis

Wardle, M. & Yusef-Zadeh, F. 2012, ApJ, 750, L38

Weaver, H., Williams, D. R. W., Dieter, N. H., & Lum, W. T. 1965, Nature, 208, 29

White, R. L., Becker, R. H., Helfand, D. J., & Gregg, M. D. 1997, ApJ, 475, 479

Whittle, M. & Wilson, A. S. 2004, AJ, 127, 606

Wilson, A. S. & Colbert, E. J. M. 1995, ApJ, 438, 62

Wilson, T. L., Rohlfs, K., & Hüttemeister, S. 2009, Tools of Radio Astronomy (Springer-Verlag)

Wright, E. L., Eisenhardt, P. R. M., Mainzer, A. K., et al. 2010, AJ, 140, 1868

Xanthopoulos, E., Thean, A. H. C., Pedlar, A., & Richards, A. M. S. 2010, MNRAS, 404, 1966

Yamauchi, A., Nakai, N., Ishihara, Y., Diamond, P., & Sato, N. 2012, PASJ, 64

Yasuda, N., Fukugita, M., & Okamura, S. 1997, ApJS, 108, 417

Zakamska, N. L. & Greene, J. E. 2014, MNRAS, 442, 784

Zel'dovich, Y. B. 1964, Soviet Physics Doklady, 9, 195

Zhang, J. S., Henkel, C., Guo, Q., & Wang, J. 2012, A&A, 538, A152

Zhao, W., Braatz, J. A., Condon, J. J., et al. 2018, ApJ, 854, 124